

ABSTRACT

NEELAM SHEORAN. Influence of Ionic Conductivity on Unconfined Melt Electrospinning of Thermoplastics. (Under the Direction of Dr. Laura Clarke and Dr. Jason Bochinski).

This Ph.D. dissertation explores an approach to creating electrospun nanofibers using thermoplastic melts. Thermoplastic melts and various commercial additives were used to understand the effect of ionic conductivity in setting jet radius (which sets the upper limit on the fiber size). An "unconfined" free surface geometry for melt electrospinning was utilized to avoid parasitic effects associated with melt electrospinning such as needle clogging and low throughput. Free surface geometry also enabled a direct observation of important characteristic length scales related to the interaction of the fluid and the applied electric field. The study includes the discussion of various parameters such as flow rate, viscosity, conductivity impacting the fiber morphology and how, by understanding the role of these critical parameters, we can move towards creating nanofibers.

In Chapter 1, a brief history of the electrospinning process, traditional electrospinning setup, and significance of charges/ions in polymer solution/melt in creating Taylor cones and electrospun jets were discussed. The limitations of solution electrospinning setup, leading to unconfined (free surface) melt electrospinning innovation was also reviewed. Finally, different parameters (particularly focusing on the polymer solution/ melt) affecting the electrospinning process were briefly reviewed.

In Chapter 2, an effect of ionic conductivity on determining the size of melt electrospun fiber was examined by comparing the experimental results with theoretical understanding of fluid mechanics. Two polymer systems with varying viscosity and initial ionic conductivity were utilized to study the effect of change in conductivity of the polymer through an addition of a

commercial additive (of varying concentrations). Physics of fluid interactions under an applied field was studied by overserving and understanding the changes in various characteristics length scales when commercial additives were used to manipulate the conductivity of the thermoplastic melt. Different parameters including the flow rate and viscosity impacting the fiber morphology were discussed. Finally, the significance of conductivity in determining the upper limit of the fiber size was explored and discussed.

In Chapter 3, a set of different polymer systems with various commercial additives spanning an extensive range of viscosity and conductivity values were studied to understand the overall impact of conductivity on fiber size. A significant reduction in fiber size was observed, and these results scaled in a similar manner as solutions with four orders of magnitude lower viscosity and eight orders of magnitude higher conductivity, indicating that ionic conductivity may be a limiting factor influencing fiber size.

In Chapter 4, from our understanding of conductivity and various other parameters affecting the fiber size, an approach of creating nanofibers was explored. The most stable case with a relatively higher conductivity from the previous analysis was used and optimized by tuning various extrinsic and intrinsic electrospinning parameters. Finally, the effect of the ambient temperature on nanofiber formation was discussed.

In Chapter 5, a summary of different parameters impacting the fiber size throughout this dissertation was discussed. A pathway of creating nanofibers from thermoplastic melts via unconfined melt electrospinning was discussed.

© Copyright 2022 by Neelam Sheoran

All Rights Reserved

Influence of Ionic Conductivity on Unconfined Melt Electrospinning of Thermoplastics

by
Neelam Sheoran

A dissertation submitted to the Graduate Faculty of
North Carolina State University
in partial fulfillment of the
requirements for the degree of
Doctor of Philosophy

Physics

Raleigh, North Carolina
2022

APPROVED BY:

Dr. Laura Clarke
Co-Chair

Dr. Jason Bochinski
Co-Chair

Dr. Keith Weninger

Dr. Russell Gorga

Dr. Alexander Kemper

DEDICATION

To my family and friends

BIOGRAPHY

Neelam Sheoran was born in the city of Kanpur in India. She moved to New Delhi where she completed her high school. High school piqued her interest in science. She was fascinated by the laws of physics and looked up to childhood science heroes such as Prof. Stephen Hawking and Dr. Feynman. She pursued a bachelor's in physics from the prestigious University of Delhi, India in 2013. She followed up with a Master's in Physics from Jamia Millia Islamia University, New Delhi in 2015.

She continued her journey in science and decided to go to grad school at North Carolina State University in 2016. After completing her course work and qualifiers, she joined the Clarke lab in 2017. She was interested in the polymer science research being conducted in the lab and could envision numerous applications of the research. This inspired her to perform her duties with utmost sincerity and dedication.

She presented her research at numerous conferences in form of poster and oral presentations such as American Physical Society (APS) March meeting conference 2018 at Boston, APS March meeting 2019 and APS march meeting 2020. Her research was affected by the Covid 19 pandemic shut down across the world, but she continued to be self-motivated and progressed forward in research as per the graduate plan in tandem with her supervisor and committee members. She also enjoyed her time as TA for teaching introductory labs and in developing minilabs for innovative program to teach experimental physics to undergraduates and invoke curiosity among them.

She also completed the A2i industrial training certificate at the NCSU in 2018 and Technology Entrepreneurship and Commercialization (TEC) certificate program from Jenkins, MBA school of NC State to elevate her communication and network building skills. This also heled her in preparing for interviews and making career decisions beyond her Ph.D.

Other than being cool at science, she loves spending time with her friends and family and go for long walks in the evening. Lake Raleigh and Lake Johnson are some of her favorite hiking spots.

She wishes to continue her journey by contributing to science and technology and excelling in her journey ahead.

ACKNOWLEDGMENTS

Throughout my Ph.D., I received tremendous support from a lot of people, and I would like to take this opportunity to acknowledge them.

I wish to express my sincere appreciation to my advisor Dr. Laura Clarke for her constant mentoring and guidance over the last 5 years. She was always there to extend her professional and emotional support whenever needed. I thank you for providing me this opportunity to work with you and believing in me. I would like to thank my co-advisor, Dr.Bochinski, for providing his knowledge and experience to help me succeed in my experimental adventures. I would like to thank my committee member Dr. Russell Gorga, Dr. Keith Wenninger, Dr. Alexander Kemper, for their time, expertise, and guidance.

I would like to thank my colleague Brenton Boland for being one of the best labmate I could have asked for. I really appreciate all his scientific insights and discussions and so many other things he did to support me and my research over the past 5 years. I would also like to thank Dr. Honglu Huang and Dr. Gabriel Firestone for their initial support in setting up my research project and for making me feel welcomed in the lab. Finally, I also appreciate Sam Thornton for helping me with my experiments, especially for carrying my project forward when I got stuck in India due to COVID.

I would like to acknowledge the many facilities within NC State that assisted in this research, including the Analytical Instrumentation Facility (AIF), the Education and Research Laboratory (EaRL), and the TECS. As well as Dr. Weninger, Ms.Judy Elson and Dr. Karen Daniels for the use of their equipment.

I want to thank my mom and dad, they always believed in bigger things for me. My mom didn't get the opportunity for any education, but she lived her dream through me by enabling me to go out in the world and get the highest educational degree. My dad set an exemplary example of discipline and hard work in life. Thank you both for all the values you gave me to help me succeed in my life. A big thank you to my siblings Robin Sheoran and Sunita Chahar and my niece Mudra Chahar for loving me and always making me feel special.

A special thanks to my partner and my love Dinesh Kaushik for always believing in me and supporting me. Four years of long-distance was not easy, but you always made me feel loved and special.

Finally, my chosen family, all my friends back at home and here who have constantly been asking me since the day I started, about when I will be done with the Ph.D.

Special mention to Dr. Abhimanyu Sharma, Dr. Ashish Kapoor, Anshu Sharma, Neeraj Mehta, Vaibhav Kumar, Abha Thapliyal, Shreya Tangri, thank you so much for all the laughs and support.

TABLE OF CONTENTS

LIST OF TABLES	ix
LIST OF FIGURES	x
CHAPTER 1	1
1.1. Introduction	1
1.2 Traditional needle-based Electrospinning	1
1.3. Melt electrospinning	6
1.4. Parameters affecting electrospinning.....	10
1.5. References	15
CHAPTER 2	27
2.1. Introduction	29
2.2. Results and Discussion	31
2.2.1. Selection of materials and material properties	31
2.2.2. Spontaneous fingering to form cone-jets	34
2.2.3. Additional characteristic length scales	39
2.2.3.1. Capillary length - understanding the fluid position on the plate and the cone width .	40
2.2.3.2. Jet radius, jet length, and flow rate.....	42
2.2.3.3. The uniquely useful role of conductivity in setting the jet radius	47
2.2.3.4. Fiber diameter.....	49
2.2.4. The path from jet to fiber	53
2.2.5. The role of the additive in increasing melt conductivity.....	55
2.2.6. Advantages of the open plate configuration.....	56
2.3. Conclusion.....	58
2.4. Experimental Methods.....	60
2.4.1. Materials and characterization	60
2.4.2. Apparatus	60
2.4.3. Characterizing the electrospinning process and fiber morphology	62
2.4.4. Calculation of electric fields	64
2.4.5. Conductivity measurements	66
2.4.6. Rheology measurements	68
2.5. References	69
CHAPTER 3	75
3.1. Introduction	76
3.2. Experimental methods.....	77

3.2.1. Material used.....	77
3.2.2. Electrospinning Process	77
3.2.3. Imaging of electrospinning process.....	78
3.2.4. Rheology and Conductivity measurements.....	79
3.3. Results and Discussion.....	81
3.4. References	91
CHAPTER 4	93
4.1. Introduction	94
4.2. Results and Discussion.....	94
CHAPTER 5	98
5. 1. Conclusion.....	98
APPENDICES	104
Appendix A-1	105
A-1.1. Conductivity measurement	105
A-1.1.1. Impedance spectroscopy	105
A-1.1.2. Measurement Techniques	107
A-1.1.2.1. Prober System	107
A-1.1.2.2. In-situ conductivity measurement: equipment modification.....	108
A-1.1.2.3. Interdigitated electrodes	112
A-1.1.3. Effect of ambience on measurement.....	115
A-1.1.4. Broadband dielectric analysis to study the effect of different temperatures and additive wt%.....	117
A-1.1.4.1. Dielectric loss tangent curves.....	117
A-1.1.4.2. Nyquist plots	119
A-1.1.4.3. Dielectric permittivity curves.....	122
A-1.1.4.4. AC Conductivity curves.....	123
A-1.2.1. Program for automated analysis of LCR data.....	129
A-1.2.2. Program for automated analysis of capacitance bridge (CB) data.....	132
A-1.3. References	137
Appendix A-2.....	140

LIST OF TABLES

Table 3.1 The linear low-density polyethylene (LLDPE) formulations utilized in this work with measured values for conductivity and viscosity at the stated electrospinning working temperature.....	80
---	----

LIST OF FIGURES

Figure 1.1 Traditional needle-based solution electrospinning setup showing the spinneret, linear and whipping jet region along with the fiber deposition on the grounded collector.....	2
Figure 1.2 Schematic diagram showing different forces acting on the Taylor cone and Jet formation as the jet travels towards the collector. Jet is assumed to be collection of charged beads. ¹³	3
Figure 1.3 Schematic showing the evolution of the jet including the whipping instabilities creating a helical cone structure	4
Figure 1.4 Schematic (top view) of unconfined melt electrospinning.....	8
Figure 2.1 a) Viscosity as a function of temperature for ASPUN (blue data) and DNDA (red data) with 0.0, 0.1, and 5.0 wt% FA38 additive (solid, dashed, and dotted lines), respectively. Inset: a magnified view of region 0 – 400 Pa-s and 175 – 200 °C. b) Ionic conductivity as a function of polymer melt temperature for ASPUN (blue data; square, diamond, right-facing triangle symbols) and DNDA (red data; circle, triangle, left-facing triangle symbols) with 0.0, 0.1, and 5.0 wt% FA38 additive, respectively. The green vertical lines indicate the approximate polymer temperature used during the electrospinning process (~195 °C).....	33
Figure 2.2 Top-down view of a sequence of photographic images of the spinning plate edge during the formation of protrusions and jets. The time sequence starting from $t = 0$ s, with images taken every 60 seconds (15 seconds) respectively, from left to right for ASPUN (DNDA). The scale bar represents 1 cm in each image.....	35
Figure 2.3 Inverse average time to spontaneous perturbation formation at the plate edge $1/\tau$ as a function of additive FA38 wt% for two different formulations of LLDPE. Solid lines with filled symbols (dashed lines with open symbols) are experimental (theoretical, Equation 1) $1/\tau$ values for ASPUN (blue square symbols) and DNDA (red circle symbols), respectively.....	36
Figure 2.4 Plot of observed jet number versus time. Measurements were performed by counting the number of jet sites every minute using video images for (a) ASPUN (blue data; square, diamond, right-facing triangle symbols) and (b) DNDA (red data; triangle, circle, left-facing triangle symbols) with 0.0, 0.1, and 5.0 wt% FA38 additive, respectively. The polymer melt temperature was held at 195 °C and -45 kV was applied to the collector. (c) Steady state values for each case with experimental data (filled symbols) compared to theoretical values (open symbols) from Equation 2.....	38

- Figure 2.5 Schematic depiction of the characteristic length scales in the melt electrospinning process from a top-down and side view perspective, respectively.....39
- Figure 2.6 a) Position of the fluid edge relative to the plate edge (i.e., x -extension and y -extension) as a function of additive loading wt%. Experimental values (filled symbols) are measured for x - (diamond (ASPUN) and triangle (DNDA) symbols) and y -extensions (right-facing triangle (ASPUN) and left-facing triangle (DNDA) symbols), while theoretical values (open symbols) (square (ASPUN) or circle (DNDA) symbols) are calculated from Equation 3 using the electric field simulation value at the observed x - and y -extension location. b) Cone width as a function of FA38 loading wt%. The different PE formulations are ASPUN (blue data) and DNDA (red data), with experimental values (filled symbols) and theoretical values (from Equation 3, open symbols) respectively.....41
- Figure 2.7 a) Measured experimental values (filled symbols) for the characteristic jet radius r_{cross} and length x_{cross} compared with theoretical predictions (open symbols) from Equation 4 and 5 for ASPUN (blue data) and DNDA (red data), respectively. As discussed in the text, $x_{cross} \sim a$. For this data group, we find $x_{cross} = 1.5a$ on average. Images of the jets at different additive loading levels 0.0, 0.1, and 5.0 wt% from top to bottom for b) ASPUN and c) DNDA.....44
- Figure 2.8 Comparison of experimental data (filled symbols) and theoretically calculated (open symbols) flow rate from Equation 6 as a function of FA38 loading wt% for ASPUN (blue squares) and DNDA (red circles), respectively. Letting $a = 0.75r_{cone}$ ($a = 0.40r_{cone}$) gives the open (starred open) symbol theoretical fit. For ASPUN, the order of magnitude theory, $Q \propto \pi a^2 \frac{\gamma}{\eta}$ is also plotted (open blue diamonds).....46
- Figure 2.9 a) A characteristic experimental jet radius (blue squares, blue line) compared with theoretical predictions (blue dashed line) from Equation 8 for ASPUN. Near the plate edge, the cone-jet is dominated by the cone formula as expected. The $\frac{1}{x}$ form for the jet is consistent with the data out to and beyond the cross-over point, here marked by the average x_{cross} (2.75 mm) and r_{jet} ($r_{cross} = 50 \mu\text{m}$). After ca. 4 mm, motion of the forming fiber and loss of focus make the experimental data unreliable. The theoretical curves is about 75% of that predicted by Equation 8 (with a co-factor of 3) for this condition, within the expected error, and reaches the predicted fiber size (i.e., 13 μm) at 11 mm. b) Measured average velocities for each experimental case (filled symbols, solid lines) for ASPUN (blue data) and DNDA (red data) were compared with the theoretical equivalent case (open symbols, dashed lines).....51

- Figure 2.10 Histogram graphs of melt electrospun fiber diameters for ASPUN (blue data, left column) and DNDA (red data, right column) as a consequence of increased additive loading wt% (top to lower row). In each graph, the inset is an SEM image of the fibers; scale bars in each graph represent 200 μm52
- Figure 2.11 Photographic images of the spinning plate edge (top down view) captured every 15 seconds for 8 consecutive images (left to right) showing the evolution of protrusions and jets formation for samples composed of (a) as-received DNDA and those with the addition of (b) 0.1 wt%, and (c) 5.0 wt% loading FA38. The scale bar represents 1 cm in each image.....58
- Figure 2.12 Schematic diagram (top-down view): after application of high voltage the polymer melt on the horizontal metal spinning plate spontaneously forms protrusions, leading to jet creation and subsequent fibrous mat deposition on the metal collector located 10 cm from the plate edge. Note: The spinning plate rests on top of a hot plate which is not shown in the image for enhanced clarity.....62
- Figure 2.13 Electric field simulation results viewed from a) side, and b) top-down perspectives, respectively, with the field amplitude color scale given above. The purple triangle in a) indicates the blade edge where the polymer is placed. c) The magnitude of the electric field at the center of the plate and a location of $y = 380 \mu\text{m}$ (i.e., at the average location of the polymer surface where jets form) as a function of x , where the origin $x = 0 \mu\text{m}$ is located at the plate edge. The distance from plate edge to the collector is 10 cm.....65
- Figure 2.14 Experimental Nyquist plots (imaginary part versus real part of the complex impedance) for as-received DNDA (circles) and DNDA + 5.0 wt% FA38 (squares) at 200 °C. (b) A single RC circuit model was used to fit data from as-received and 0.1 wt% FA38 loading additive cases, and (c) a two parallel RC model circuit was used for data from 5.0 wt% additive melts, resulting in the fits shown as black lines (solid and dashed, respectively). Fitted R values from these curves were used to calculate the bulk resistance of the polymer melt sample.....67
- Figure 3.1 (a) Experimental schematic (from above) consisting of two metal plates attached by a high voltage power supply. The grounded source plate resides on the surface of a hot plate (not shown). The polymer melt is shown in blue. After voltage is applied, first protrusions and then cone-jets are formed in the direction of the collector (held at high voltage). Jets thin until the polymer solidifies as a fiber, which is deposited onto the collector.....81

- Figure 3.2 (a) Images of the source plate edge at 1, 2, 3, 4 minutes after voltage applied for DNDA 1088 at 165 °C. (c) Same as b but for DNDA 1088 with 5% FA38 (165 °C) for 1, 1.25, 1.5, 1.75 minutes. For the higher conductivity case, the jet width is noticeably narrower.....82
- Figure 3.3 Theoretical prediction of the capillary length as a function of distance from the plate edge for a fixed y value utilizing electric field simulation results and reasonable estimates [ref surface tension as a function of temperature] of the surface tension for a linear low density polyethylene melt at 165 -195°C. Experimental tracking of the surface tension as a function of additive was consistent with these limits.....84
- Figure 3.4 For each of the 13 cases (with a minimum of three experiments per case) described in Table 1, the distance between neighboring cone-jets λ , (scaled by 3π) is plotted versus $Y1$ (thickness of the fluid at the plate edge). The fit line has a slope of 1. The values are clustered in the region of 300-500 microns as estimated from Figure 3.....85
- Figure 3.5 Average observed capillary length (from $Y1$ and $\lambda/3\pi$) for each of the 13 cases in Table 1 (filled symbols) plotted versus conductivity. The open symbols are a model: for $K < 1e-6$ S/m, $\kappa^{-1} \sim K^{-0.25}\eta^{0.40}$, for $K > 1e-6$ S/m, $\kappa^{-1} \sim K^{0.25}\eta^{0.40}$. The agreement between model and experiment is good.....87
- Figure 3.6 Flow rate (measured from mass loss divided by number of jet-seconds determined from videographs of each experiment). The average value over all data is 6.2 ± 1.1 m³/jet-sec indicated by the horizontal line, which overlaps with the error bar of most points, indicating no dependence on conductivity over 4 orders of magnitude nor viscosity (which varies by a factor of 5, see table 3.1).....88
- Figure 3.7 Fiber radius for the 13 cases in Table 1 as a function of measured melt ionic conductivity. The fit line has a slope of $K^{-0.29}$89
- Figure 3.8 Comparison of the fiber radius versus conductivity data in this work to literature precedent with a conductivities 8 orders of magnitude larger. The slope line for the solution phase data (after the original reference [Angamma and Jayaram, IEEE Trans. Indust. Appl. 47 1102 (2011)] is $K^{-0.16}$90
- Figure 4.1 Fiber diameter as a function of applied voltage for DNDA 1088 with 5wt% FA38 with a) 5 g of polymer melt at 185 deg. C and b) 10 g of polymer melt at 165 deg. C. No significant change is observed as voltage is altered over the working range.....95
- Figure 4.2 Fiber diameter versus applied voltage for different melt temperatures of DNDA 1088 with 5wt% FA38 (10 grams on plate). A general decrease with temperature is observed.....96

Figure 4.3 Fiber radius for various formulations where the region beyond the plate where elongation of the jet into a fiber occurs.....	97
Figure A-1.1 A graphical representation of the complex impedance plane.....	106
Figure A-1.2 (Top) Prober system setup with two probe arms and metal stage chamber (Bottom Left) Close up of metal stage chamber with IDE loaded with polymer sample (Bottom right) Close up of the probe.....	108
Figure A-1.3 In-situ measurement setup a) side view and b) front view, holding the IDE along with metal plate sitting on the hot plate.....	110
Figure A-1.4 Conductivity as a function of pure DNDA 1088 and DNDA 1088 + 5% FA38 is plotted for two measurement techniques (black squares – in-situ measurement and red square – station prober measurement).....	111
Figure A-1.5 a) Metroohm 10 μm bands/gaps Gold interdigitated on glass substrate b) Stereo microscope (top) and AFM 3D (bottom) images of G-IDEAU10, 10 μm bands/gaps IDE c) Schematic of planar interdigitated electrode.....	113
Figure A-1.6 a) Electric field pattern in parallel plate electrode configuration b) Electric field patter in IDE	114
Figure A-1.7 Nyquist plot of ASPUN 6850A for two different melt temperatures (150 $^{\circ}\text{C}$ and 190 $^{\circ}\text{C}$) showing an overlap over measured frequency range for both CB (solid lines) and LCR (dotted lines) measurements.....	115
Figure A-1.8 Ionic conductivity as a function of polymer melt temperature for ASPUN 6850A LLDPE with no additive (black lines) and with 5wt% Hostastat FA38 additive (red lines) measured inside prober system with vacuum (solid lines) and without vacuum (dotted lines).....	116
Figure A-1.9 Dielectric loss tangent as function of frequency was plotted for a) pure DNDA 1082 and b) DNDA 1082 with 5% FA38 additive as function of melt temperature (130 $^{\circ}\text{C}$ to 190 $^{\circ}\text{C}$) c) and d) DNDA 1082 with increasing wt% of FA38 at lower (140 $^{\circ}\text{C}$) and higher (190 $^{\circ}\text{C}$) melt temperatures respectively.....	118
Figure A-1.10 Nyquist plots for given range of frequency (1Hz to 20kHz) were plotted for a) DNDA 1082 and b) DNDA 1082 + 5% FA38 with varying melt temperatures (130 $^{\circ}\text{C}$ to 200 $^{\circ}\text{C}$).....	120
Figure A-1.11 Nyquist p Nyquist plots for given range of frequency (1Hz to 20kHz) were plotted for DNDA 1088 with varying (0,5,10) Hostastat FA38 additive wt% at higher melt temperature (190 $^{\circ}\text{C}$)	121

Figure A-1.12 Equivalent RC circuits for Nyquist plots a) for fitting one semicircle b) for fitting two semicircles. Constant phase element (CPE) instead of ideal capacitance is used to fit depressed semicircle of varying radii.....	120
Figure A-1.13 Real (ϵ') and complex (ϵ'') dielectric permittivity as a function of frequency were plotted for DNDA 1082 with varying Hostastat FA38 additive wt% (0, 5, 10) at two different polymer melt temperatures (140 °C and 190 °C)....	123
Figure A-1.14 Ac conductivity and real relative permittivity are plotted as function of frequency. Graph represents the lower and high frequency region dispersion region and intermediate frequency plateau region along with some limiting features.....	125
Figure A-1.15 AC conductivity as a function of frequency were plotted for DNDA 1082 with varying Hostastat FA38 additive wt% (0, 5, 10) at two different polymer melt temperatures (140 °C and 190 °C).....	126
Figure A-1.16 Nyquist plot for DNDA 1088 + 5% FA38 measured via in-situ conductivity measurement as a function of time which the polymer was heated on the metal stage (0 mins is when polymer is fully melted, and temperature reaches 180 °C) was plotted.....	127
Figure A-1.17 Nyquist plot for DNDA 1088 + 5% ATMER129 measured via in-situ conductivity measurement as a function of time for which the polymer was heated on the metal stage (0 mins is when polymer is fully melted, and temperature reaches 180 °C) was plotted.....	128
Figure A-2.1. a) Jet and ultimate fiber size show no dependence on melt viscosity for either LLDPE formulation. b) Jet size decreases as melt conductivity increases. The line is conductivity raised to the -0.25 power.....	140
Figure A-2.2. Expanded histogram graphs of fiber diameter distributions for different LLDPE formulations with 5.0 wt% FA38 additive loading for a) ASPUN (blue data) and b) DNDA (red data), respectively.....	141
Figure A-3.3. Drawings of the source plate and planer blade. Dimensions are given in inches.....	142

CHAPTER 1

1.1. Introduction

Polymer meso (micro to nano) scale fibers have applications in air and water filtration, drug delivery, energy storage, wound healing, and artificial tissue engineering.¹⁻⁶

Currently, there are different methods of producing the sub-micron polymer fibers in the textile industry, such as fiber drawing, melt blowing, electro blowing, and electrospinning. However, electrospinning is the most common technique used in producing meso (micro to nanoscale) fibers due to its simplicity, applicability over a wide range of materials, and low cost.⁵

The word electrospinning is derived from “electrostatic spinning”. This term was first proposed by William Gilbert in the 1600s when he utilized static electricity to deform the water droplets.^{7,8}

Later in the 1900s Cooley and Morton made the first effort to create fibers using this technique.⁹

In 1917, Zeleny first photographed the electrospinning process.¹⁰ Aton worked on the significantly on developing the experimental electrospinning process between 1934 and 1944. But it was Taylor in 1969, who provided a theoretical explanation on deforming the fluid droplets into conical structure now known as Taylor cone.^{11,12} Owing to scientific and technological advancements at the end of the 20th century researchers started producing ultra-fine fibers in 1980s. Due to the availability and ease of the process, electrospinning started gaining both industrial and academic attention. Since then, there have been multiple studies undertaken to understand the process of electrospinning and to improve the morphology of the fibers produced.

1.2 Traditional needle-based Electrospinning

As mentioned earlier, electrospinning is a widely popular fiber fabricating technique due to its simple setup. A typical traditional needle-based electrospinning setup (TNE) consists of a high

voltage power supply, a needle with a small diameter, and a ground collector (shown in Figure 1.1). The process of electrospinning is broadly divided into three parts. It starts with the polymer fluid forming a Taylor cone at the tip of the needle. The cone then transforms into a jet, followed by a jet thinning process. This leads to fiber deposition on the collector as shown in Figure 1.1.

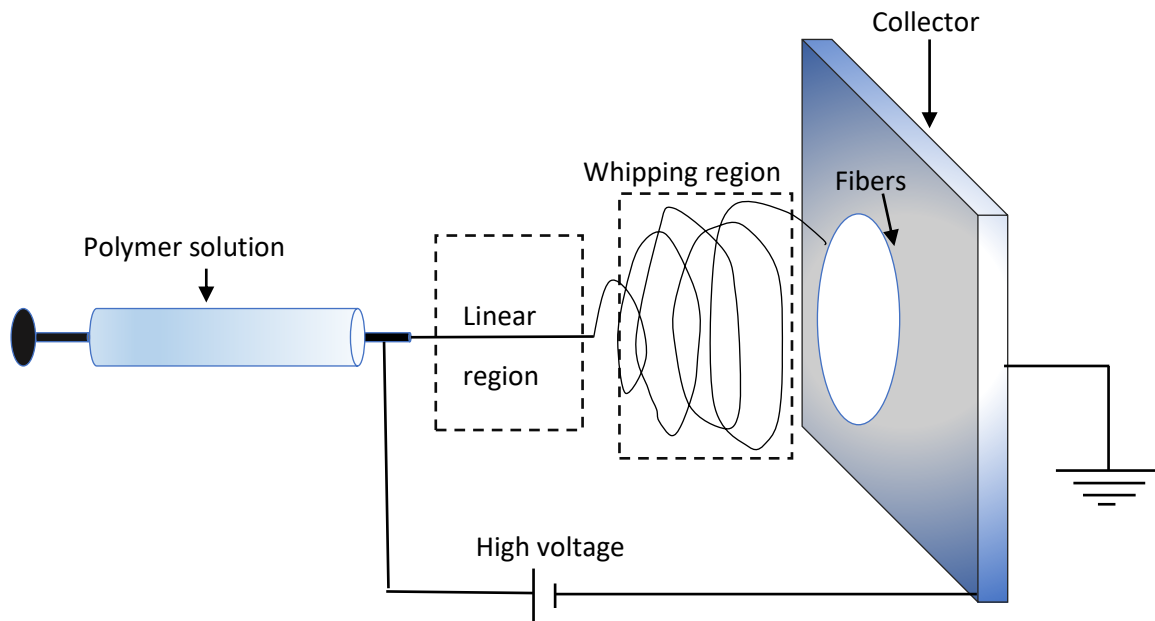


Figure 5.1. Traditional needle-based solution electrospinning setup showing the spinneret, linear and whipping jet region along with the fiber deposition on the grounded collector.

In a typical configuration, a high external potential is applied to the tip of the needle. A potential difference is created between the needle and a grounded collector. This potential difference creates an electric field around the fluid meniscus which is formed at the tip of the nozzle and moves the charges/ions to the surface of the polymer. Different types of electric forces such as surface charge coulomb force and external field electrostatic force, develop at the interface, balanced by the surface tension and viscous force induced by the fluid (as shown in Figure 1.2).

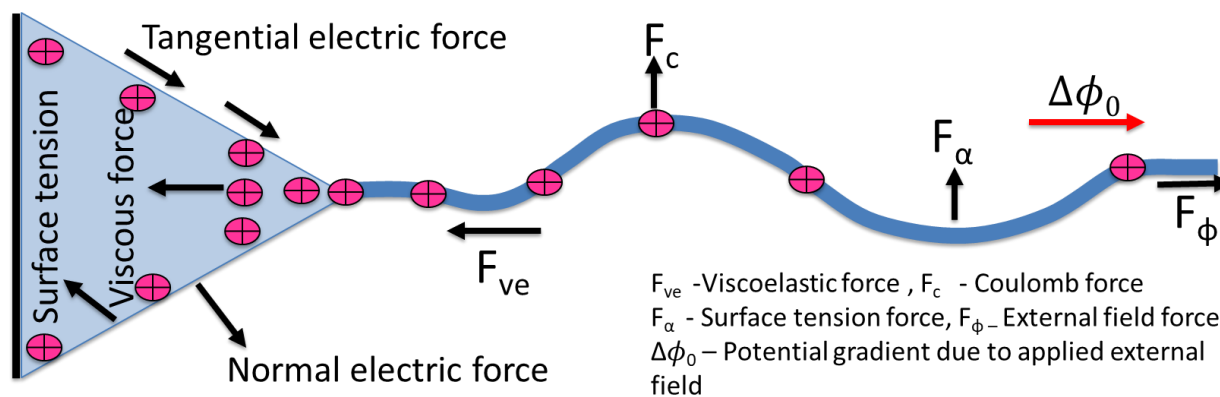


Figure 1.6. Schematic diagram showing different forces acting on the Taylor cone and Jet formation as the jet travels towards the collector. Jet is assumed to be collection of charged beads.¹³

The surface charges in the presence of external electric field creating electrostatic force governs the formation of the Taylor cone at the tip of the fluid meniscus. The tangential field component of the fluid, as shown in Figure 1.2, induces this electrostatic force to stretch the cone to form a jet. A Taylor cone (half-angle of the cone is 49.3°) at the tip of the needle is formed when the applied external field approaches a critical value.¹² Usually, in the experimental setup, this half-angle of the cone is smaller ($30^\circ - 37^\circ$) than the predicted theoretical value (49.3°). As the electric field is increased beyond the critical value, the electric forces overcome the surface tension and viscous forces to form a jet. Hence, this approach necessitates a conductive polymer solution instead of ideal dielectrics to start an electrospinning process. As in the case of ideal dielectric, there will not be enough ions/charges to move to the surface of the polymer in the presence of an external electric field, and hence there will be no occurrence of Taylor cone or jet formation.

Once the jet initiates, both repulsive Coulomb force between the charges and electrostatic forces governs the jet motion as it moves towards the collector in the direction of the electric field (as shown in Figure 1.1).

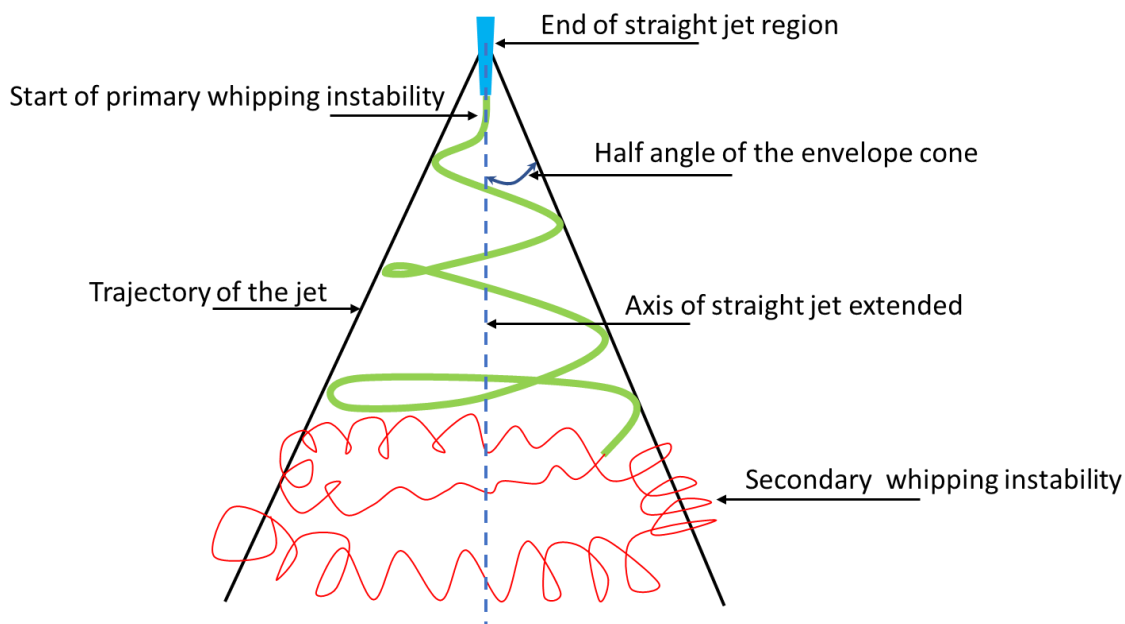


Figure 1.7. Schematic showing the evolution of the jet including the whipping instabilities creating a helical cone structure

In the initial transition region of forming straight jet out of Taylor cone, the tensile stress of the polymer fluid increases. Both the shape and the charge distribution of the jet was determined by the strain rate as it provides a high longitudinal viscoelastic stress.¹⁴ The charge distribution in this region affects the jet diameter. The initial stretching of the jet is directly proportional to the magnitude of the disturbing charge.¹⁵ The charge distribution not only decides the initial stretching but can also define the further development of the jet. Also, the bending instabilities mainly depend on the repulsive coulombic interactions. As shown in Figure 1.2, a polymer jet can be

treated as a combination of charged beads held together by a linear viscoelastic dumbbell. Different forces act on the jet, such as Coulomb and external electrical forces stretching the jet, and viscoelastic, and surface tension forces stabilizing the jet. All these forces affect the jet diameter significantly. Briefly, the viscoelastic force initial straight jet region increases and reaches its maximum with the proceeding of the jet dynamics. After reaching its peak value, it starts to decay due to viscoelastic relaxations and cannot sustain the expanding pressure of both Coulomb and external electric forces, which results in a quasistraight path (bending). In this region, the internal viscoelastic force plays a significant role as it provides the necessary stiffness to maintain the straight jet and is also a dominant force in stabilizing the jet. In addition to viscoelastic force, the surface tension also counters the bending instability. Surface tension must maintain the minimum surface area of the jet, and hence it resists bending as it leads to an increase in the jet surface. The surface tension forces can counteract small perturbations in the straight path of the jet; however, as the jet starts to move away from the Taylor cone, a more extensive instability known as whipping instability kicks in and creates a spiral conical shape of the jet (as shown in Figure 1.3). Surface tension and coulomb repulsive force due to surface charge are the two competing forces deciding the jet bending or jet stability. When dominating force is surface tension, the jet remains straight, and when surface charge repulsion dominates, the jet starts to bend, leading to more significant perturbations perpendicular to the jet centerline. All these charges follow charge conservation, where total current, which is a sum of conduction, and convection current remains constant. When the polymer is near the tip of the nozzle forming a Taylor cone, conduction current dominates, and the jet is stable. As the jet starts to thin (caused by the stretching done by the external field and solvent evaporation) and moves away from the nozzle, convection current increases as the surface charge density increases until the charge repulsion overcomes the surface

tension and jet starts whipping.¹⁶ Sometimes initial whipping can lead to secondary whipping instabilities (as shown in Figure 1.2). As the jet starts whipping, most of the stretching of the jet is happening in this region. Therefore, the size of the whipping region has a significant role in influencing the jet and ultimately the fiber diameter.¹⁶

Finally, this jet moves along the direction of the electric field and reaches a ground collector. The grounded collector is usually set at an optimized distance (usually between 5 to 25 cm) away from the nozzle. As the jet travels this distance, the solvent evaporates, which causes the solidification of jets and the formation of nonwoven electrospun fibers.

Considering recent advancements, a new electrospinning technique known as melt electrospinning is gaining researchers' and industry's attention. In contrast to solution electrospinning, where polymer solution is electrospun, a polymer is melted in melt electrospinning, and temperature change (cooling of jet) instead of solvent evaporation causes fiber solidification.¹⁷

1.3. Melt electrospinning

For the longest time, solution electrospinning has been a more popular method than melt electrospinning due to a wide variety of materials used in solution electrospinning to produce highly functional nanofibers. However, melt electrospinning has been gaining popularity in the recently due to its solvent-free environment-friendly approach to creating meso fibers. Melt electrospinning has also opened a gateway for creating fibers from commercially available materials such as thermoplastics. These materials are not readily soluble in solvents and hence were not previously utilized for electrospinning through solution electrospinning. Nevertheless, their abundance and easy availability makes them a promising candidate for creating melt electrospun fibers, especially for their application in air and water filtration. Such melt-spun meso

fibers should possess dramatically improved mechanical properties, including strength, toughness, long lifetime, and other have other attributes such as recyclability, and low cost.

Charles Norton first patented the melt electrospinning process in 1936.¹⁸ However, the scientific breakthrough in melt electrospinning happened in the 1980s when Larrondo and Manley published experimental and theoretical simulation results in various publications.¹⁹ The first article demonstrated that fibers could be drawn from the droplets of thermoplastics. The second paper proposed a theoretical model for the electrostatically drawn jet.²⁰ The third and final paper looked at the deformation effects of an electrostatic field on a molten polymeric droplet.²¹ These articles showed that a molten polymer could be electrostatically drawn and have a theoretical understanding based on Taylor's explanations.

20 years later in a peer-reviewed publication, Reneker and Rangkupan discussed creating electrospun fibers using thermoplastics in a vacuum which again focused researchers' attention to the novel technique of melt electrospinning.²² Since then, there has been continuous growth in research publications exploring the advances of melt electrospinning.

For melt electrospinning setups, researchers identified the simplicity of traditional needle-based electrospinning (TNE) and added a component, i.e., a heating device (usually with a temperature sensor), to create traditional needle-based melt electrospinning (TNME) setup.¹⁷ TNME setup offers a straightforward method for creating meso fibers. However, this benefit is usually outweighed by several processing setbacks such as needle clogging, the difficulty of pumping high viscous fluids at low feed rates, and obstacles in creating jets from highly insulating materials. Nevertheless, one considerable advantage of melt electrospinning is its ability to process without environmentally harmful organic solvents and the possible use of a wide range of materials. This

makes it a more promising technology in creating functional micro to nanoscale fibers for filtration and biomedical applications.^{23–26}

To address these processing problems and the challenge of small fiber throughput, researchers have been modifying the electrospinning setup, and one such modification led to an unconfined or open surface melt electrospinning setup. Unconfined or open surface melt electrospinning setups are systems where high voltage is applied, the fluid on a free surface, reorganizes from protrusions leading to the formation of multiple jets (example is shown Figure 1.4). Free surface melt electrospinning setups are widely used in solution electrospinning. Different configurations such as magnetic fluids, balls, discs, wires, cylinders, etc. were used in a polymer solution to form multiple jets.^{27–34} With melt electrospinning, a melt differential, disc needled, slit rod configurations, and unconfined plate edge have been utilized to increase the mass throughput of the fibers.^{35–38}

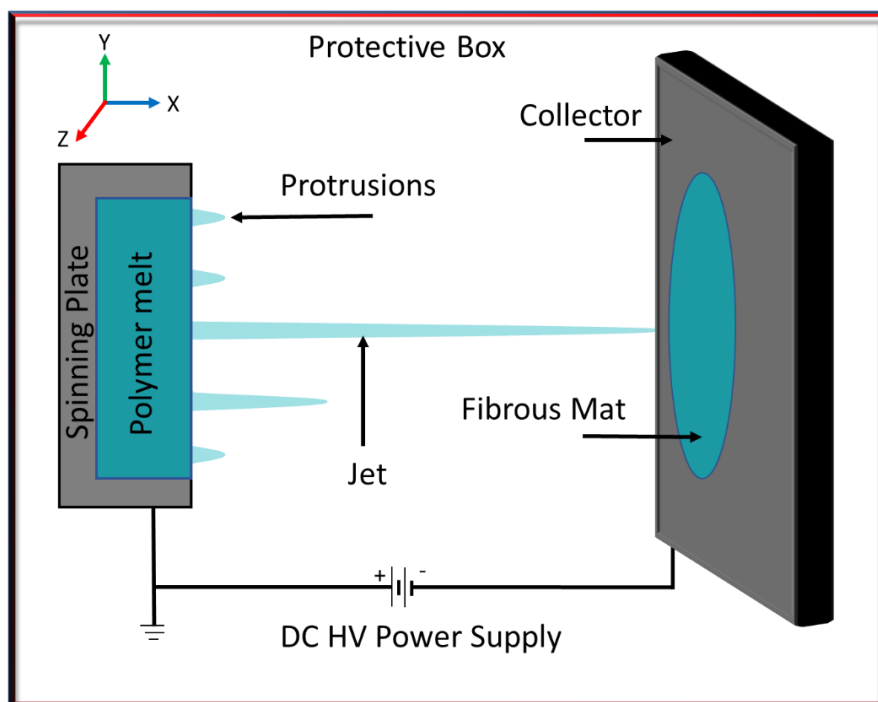


Figure 1.8. Schematic (top view) of unconfined melt electrospinning

The working mechanism of free-surface electrospinning is the same as TNE. The process involves electrostatic forces overcoming the surface tension of the melt to form spontaneous jets that occur on multiple sites of the free surface. Open-free surface setups operate at higher voltages as the electric field is less concentrated than the TNE. These multiple jets in open surface electrospinning configurations increase the fibers' throughput by many folds. Instead of the pointed needle, free surfaces have less concentrated electric fields requiring a higher voltage to overcome the surface tension of the fluid. There is also less control on the jet formation as the jets organize and self-assemble on the free surface.

A jet formation theory from free surfaces was introduced by Lukas.³⁹ The theory is based on the surface wave dynamics of "fastest-growing instability". On application of an external electric field, the charges are developed inside the fluid, and it appears to swell due to coulomb electrostatic force, however, the surface tension counteracts the unconfined growth and simultaneous protrusion are formed through the free surface. Same as solution electrospinning, as electric field above the critical electric field, jets are initiated with the fastest-growing amplitude separated by a length λ . λ is the distance between these adjacent jets, known as characteristic spacing. Generally, increasing the voltage will decrease the characteristic spacing λ and increase the number of jets. In addition, the process is affected by the interaction between jets where for higher jet densities, jets rearrange themselves to minimize the jet interaction, creating a non-linear patterns of fiber deposition.³³

These open surface geometries not only overcome the existing challenges but purely from a fundamental science perspective are useful as they enable the observation of changes in the fluid wetting properties and response to the applied electric field as a function of various extrinsic and intrinsic parameters affecting the electrospinning process. However, open surface geometries have

some challenges as the open surface area can provide access to undesired processes such as water vapor adsorption, polymer degradation, and corona discharges, affecting the final fiber morphology. Apart from these challenges, fiber morphology in the melt electrospinning process depends significantly on different extrinsic and intrinsic parameters. Therefore, it is vital that we understand how changing these different parameters can affect our fiber morphologies.

1.4. Parameters affecting electrospinning

For all types of electrospinning, there are polymer material properties such as viscosity, conductivity, process, and environmental factors such as voltage, the distance between spinneret and collector, temperature and humidity that could affect the ultimate fiber morphology. Effects of these parameters are discussed in the following section.

Effect of applied voltage/electric field have been extensively studied for both solution and melt electrospinning.^{17,40-48} In melt electrospinning, the voltage applied to form the jets is much higher (20- 100 kV) than the typical solution electrospinning (5- 20 kV). Generally, increasing the applied electric field have resulted in thinner fiber due to smaller Taylor cones and increase in electrostatic force stretching the jet.^{17,40,42,44,45,47,48} However, sometimes it may not have a significant effect or beyond a certain voltage this could negatively affect the fiber diameter and have resulted in making bead or bigger fibers.^{30,46,49-53} Specially in melt unconfined electrospinning since flow rate is governed by the applied electrostatic force, it plays a significant role in deciding fiber morphology. Along with applied voltage, effect of the collection distance between spinneret and collector provides the jet time to evaporate the solvent (in solution electrospinning) or to cool the melt before it hits the collector, have been studied for determining the optimum combination of voltage and distance that yield to a smaller fiber diameter.^{8,46,54-56}

Effect of temperature is focused for melt electrospinning as both polymers melt temperature and spin line temperature could affect the fiber diameter. With increase in melt temperatures a significant decrease in the fiber diameter was overserved attributed to the decrease in viscoelasticity and viscosity of the polymer fluid.^{44,47,48,53} Since higher temperatures are used for melt electrospinning, there could be polymer degradation causing the increase in average fiber diameter after a certain point. Also, the spin line temperature plays an important role as the electric force can stretch the jet only when it is in its melted form. Different methods are used for heating this region.^{8,54,57-59} With increase in the spin line temperature a decrease in fiber diameter was observed till an optimum temperature.

Finally, there are some internal parameters such as surface tension, viscosity and conductivity that affects the fiber morphology.^{49,55,60-66} Lower viscosities of the polymer solution/melt can result in formation of beads or microspheres and a high viscosity can cause thick fibers or cause the failure of the spinning. Viscosity of the polymer depends on a lot of factors such as molecular weight, entanglement of molecular chains, temperature and additives used. In solution electrospinning the viscosity range is 5-20 Pa S, which is considered as a good range for smooth spinning. In melt electrospinning, we have much higher viscosity range 20 – 200 Pa S which can challenging at times.⁶⁷ In melt electrospinning, viscosity plays a significant role in determining the fiber diameter as it directly effects the melt flow rate of the fluid. In a certain range, decreasing viscosity contributes to better spinnability and smaller fiber diameter. Researchers have manipulated the viscosity majorly by changing the temperature and by using different additives. Since viscosity is inversely proportional to the temperature of the melt. Most of the studies, by increasing the melt temperature (thereby decreasing the melt viscosity) fiber diameter has been decreased.^{24,64-66,68-70}

Effect of rheology modifiers to decrease the fiber diameter in melt electrospinning is an area that has been explored by the researchers. However, the conductivity of the polymer fluid is an overlooked fundamental characteristic which strongly affects electrospinning outcomes. As known from the studies on electrospinning process, charges/ions play a significant role in defining the jet diameter as the surface charges creates a stretching force that causes jet thinning. An ideal dielectric polymer solution will not have enough charges/ions to move to the surface. It will not be favorable to make Taylor cone with ideal dielectric when an external field is applied. However, conductive polymers have enough charges/ions. The polymer moves to the surface to create a Taylor cone and electrospun fibers when an external field is applied. In solution electrospinning, it is relatively easy to manipulate the conductivity of the solution, and researchers have achieved this by introducing organic and salt additives to the polymer spinning solution. These salt additives increase the number of ions in the polymer solution, increasing the surface charge density of the polymer fluid. This effect creates thinner fibers as it increases the electrostatic force generated by the external electric field and decreases the tangential electric field along the surface of the fluid. However, a decrease in this tangential field with increased conductivity could also negatively impact the formation of the Taylor as the electrostatic force along the surface of the fluid diminishes. Both the straight and whipping jet regions play a significant role in determining the ultimate fiber diameter. It's been shown that increase in the surface charge density leading to stretching of the jet in the whipping region leads to nanofibers.⁷¹ To understand the effect of surface charges on fiber morphology, researchers have utilized solvents, organic and non-organic salts and conductive polymer to manipulate the conductivity of the polymer fluid. In addition to the different types and concentrations of the additives or solvents, the ion size present in the polymer solution/melt can also influence the fiber morphology.⁷¹⁻⁸⁰

While in solution electrospinning, it is relatively easier to manipulate the conductivity of the solution in contrast, however, manipulating the conductivity of the polymer melt is difficult as it is challenging to find a compatible additive. Hence in melt electrospinning, very few researchers have tried manipulating the conductivity of the melt to decrease the fiber diameter. Research groups have presented that using SO and NaCl as additives in polypropylene reduced the fiber diameter from 6 microns to 0.3 microns.⁶⁴ Other additives such as sodium, magnesium, and zinc stearates, Irgastab 16, and some biobased dyes such as biobased dyes alizarin, hematoxylin, and quercetin were utilized to increase the conductivity and reduce fiber diameter.^{81,82} It is important to note that these additives were purposely added to increase the conductivity but can also affect the viscosity of the polymer. Hence, it is important to monitor the changes in viscosity to understand the full impact of the additive affecting the fiber diameter.

Through this thesis, a comprehensive study on understanding the effect of altering the ionic conductivity on the melt electrospinning process and, ultimately, the fiber diameter was explored. Thermoplastic melts have very low ionic conductivity ($\sim 10^{-10}$ S/m) and as mentioned above, the electrospinning process requires some minimum level of mobile charges to move to the surface of the polymer to form Taylor cones in order to spin the polymer fluid. We have utilized an unconfined melt electrospinning setup which uses a metal source plate with a sharp edge (as shown in figure 1.4 to melt the polymer as opposed to the needle syringe in the case of the TNE setup. This setup eliminated the challenges of using a TNE setup, such as needle clogging and less throughput, and enabled us to visualize the changes in fluid properties when the external electric field was applied. In the usual melt electrospinning of thermoplastics, the electrospun fiber diameter is in the tens of micron range due to the polymer's high viscosity and low ionic conductivity; however, it would be desirable to make nanoscale fibers. Nanoscale

fibers of thermoplastic melts should have much improved mechanical properties and other attributes such as recyclable and low cost, making them an ideal candidate for application in highly efficient air and water filters. Furthermore, decreasing the fiber size to the nanoscale creates a dense porous structure, significantly increasing filter efficiency. Researchers have tried modifying the viscosity (as discussed in this section above) of the polymer melt through various means. However, this research focuses on analyzing the underexplored effect of ionic conductivity on various characteristics length scales of the electrospinning process and, ultimately, its effect on decreasing the fiber diameter. The effect of an increase in ionic conductivity leading to a decrease in fiber diameter has been identified in solution electrospinning. Through this research work, a connection between such solution results will be used as a model to establish a connection between the solution electrospinning and melt electrospinning processes.

In the coming chapters of this thesis, we have optimized our unconfined melt electrospinning setup for the external parameters such as voltage, collection distance, and polymer melt temperature for the given polymer sample to get the smallest fiber diameter. Different additives were added to the thermoplastics to understand the influence of the conductivity on the melt electrospinning process. Variations in conductivity and viscosity were measured, and the changes in fluid properties under an applied electric field were observed to understand the pathway of creating submicron fibers using melt electrospinning.

1.5. References

- 1) dos Santos, D. M.; Correa, D. S.; Medeiros, E. S.; Oliveira, J. E.; Mattoso, L. H. C. Advances in Functional Polymer Nanofibers: From Spinning Fabrication Techniques to Recent Biomedical Applications. *ACS Appl. Mater. Interfaces* 2020, 12 (41), 45673–45701. <https://doi.org/10.1021/acsami.0c12410>.
- 2) McCullen, S. D.; Ramaswamy, S.; Clarke, L. I.; Gorga, R. E. Nanofibrous Composites for Tissue Engineering Applications. *WIREs Nanomed Nanobiotechnol* 2009, 1 (4), 369–390. <https://doi.org/10.1002/wnan.39>.
- 3) Rosenberger, A. G.; Pellá, M. C. G.; Medeiros, A. R.; da Silva Lima, F.; Fraga, G. N.; Caetano, J.; Dragunski, D. C. Electrospun Nanofibers for Biological Application. In *Nanoengineering of Biomaterials*; John Wiley & Sons, Ltd, 2022; pp 91–121. <https://doi.org/10.1002/9783527832095.ch21>.
- 4) Asmatulu, R.; Khan, W. S. Electrospun Nanofibers for Filtration Applications. In *Synthesis and Applications of Electrospun Nanofibers*; Elsevier, 2019; pp 135–152. <https://doi.org/10.1016/B978-0-12-813914-1.00007-9>.
- 5) Xue, J.; Wu, T.; Dai, Y.; Xia, Y. Electrospinning and Electrospun Nanofibers: Methods, Materials, and Applications. *Chem Rev* 2019, 119 (8), 5298–5415. <https://doi.org/10.1021/acs.chemrev.8b00593>.
- 6) Barhate, R.; Ramakrishna, S. Nanofibrous Filtering Media: Filtration Problems and Solutions from Tiny Materials. *Journal of Membrane Science* 2007, 296 (1–2), 1–8. <https://doi.org/10.1016/j.memsci.2007.03.038>.

- 7) Amna, R.; Ali, K.; Malik, M. I.; Shamsah, S. I. A Brief Review of Electrospinning of Polymer Nanofibers: History and Main Applications. *JNMES* 2020, 23 (3), 151–163.
<https://doi.org/10.14447/jnmes.v23i3.a01>.
- 8) Bhardwaj, N.; Kundu, S. C. Electrospinning: A Fascinating Fiber Fabrication Technique. *Biotechnol. Adv.* 2010, 28 (3), 325–347.
<https://doi.org/10.1016/j.biotechadv.2010.01.004>.
- 9) Teo, W. E.; Ramakrishna, S. A Review on Electrospinning Design and Nanofibre Assemblies. *Nanotechnology* 2006, 17 (14), R89–R106. <https://doi.org/10.1088/0957-4484/17/14/R01>.
- 10) Zeleny, J. Instability of Electrified Liquid Surfaces. *Phys. Rev.* 1917, 10 (1), 1–6.
<https://doi.org/10.1103/PhysRev.10.1>.
- 11) Taylor, G. I.; McEwan, A. D. The Stability of a Horizontal Fluid Interface in a Vertical Electric Field. *Journal of Fluid Mechanics* 1965, 22 (1), 1–15.
<https://doi.org/10.1017/S0022112065000538>.
- 12) Taylor, G. I.; McEwan, A. D.; de Jong, L. N. J. Studies in Electrohydrodynamics. I. The Circulation Produced in a Drop by an Electric Field. *Proceedings of the Royal Society of London. Series A. Mathematical and Physical Sciences* 1966, 291 (1425), 159–166.
<https://doi.org/10.1098/rspa.1966.0086>.
- 13) Reneker, D. H.; Yarin, A. L.; Fong, H.; Koombhongse, S. Bending Instability of Electrically Charged Liquid Jets of Polymer Solutions in Electrospinning. *Journal of Applied Physics* 2000, 87 (9), 4531–4547. <https://doi.org/10.1063/1.373532>.
- 14) Reneker, D. H.; Yarin, A. L. Electrospinning Jets and Polymer Nanofibers. *Polymer* 2008, 49 (10), 2387–2425. <https://doi.org/10.1016/j.polymer.2008.02.002>.

- 15) Lauricella, M.; Pontrelli, G.; Coluzza, I.; Pisignano, D.; Succi, S. JETSPIN: A Specific-Purpose Open-Source Software for Simulations of Nanofiber Electrospinning. *Computer Physics Communications* 2015, 197, 227–238. <https://doi.org/10.1016/j.cpc.2015.08.013>.
- 16) Fridrikh, S. V.; Yu, J. H.; Brenner, M. P.; Rutledge, G. C. Controlling the Fiber Diameter during Electrospinning. *Phys. Rev. Lett.* 2003, 90 (14), 144502.
<https://doi.org/10.1103/PhysRevLett.90.144502>.
- 17) Lyons, J.; Li, C.; Ko, F. Melt-Electrospinning Part I: Processing Parameters and Geometric Properties. *Polymer* 2004, 45 (22), 7597–7603.
<https://doi.org/10.1016/j.polymer.2004.08.071>.
- 18) Norton, C. L. Method of and Apparatus for Producing Fibrous or Filamentary Material. US2048651A, July 21, 1936.
- 19) Larrondo, L.; Manley, R. Electrostatic Fiber Spinning from Polymer Melts. I. Experimental Observations on Fiber Formation and Properties. 1981.
<https://doi.org/10.1002/POL.1981.180190601>.
- 20) Larrondo, L.; St. John Manley, R. Electrostatic Fiber Spinning from Polymer Melts. II. Examination of the Flow Field in an Electrically Driven Jet. *Journal of Polymer Science: Polymer Physics Edition* 1981, 19 (6), 921–932.
<https://doi.org/10.1002/pol.1981.180190602>.
- 21) Larrondo, L.; St. John Manley, R. Electrostatic fiber spinning from polymer melts. III. Electrostatic deformation of a pendant drop of polymer melt. *Journal of Polymer Science: Polymer Physics Edition* 1981, 19 (6), 933–940.
<https://doi.org/10.1002/pol.1981.180190603>.

- 22) Rangkupan, R.; RENEKER, D. Electrospinning Process of Molten Polypropylene in Vacuum. *J. Met. Mater. Miner.* 2003, 12.
- 23) Li, X.; Yang, W.; Li, H.; Wang, Y.; Bubakir, M.; Ding, Y.; Zhang, Y. Water Filtration Properties of Novel Composite Membranes Combining Solution Electrospinning and Needleless Melt Electrospinning Methods. *Journal of Applied Polymer Science* 2014, 132. <https://doi.org/10.1002/app.41601>.
- 24) Li, H.; Wu, W.; Bubakir, M.; Chen, H.; Zhong, X.; Liu, Z.; Ding, Y.; Yang, W. Polypropylene Fibers Fabricated via a Needleless Melt-Electrospinning Device for Marine Oil-Spill Cleanup. *Journal of Applied Polymer Science* 2014, 131. <https://doi.org/10.1002/app.40080>.
- 25) Hochleitner, G.; Jüngst, T.; Brown, T. D.; Hahn, K.; Moseke, C.; Jakob, F.; Dalton, P. D.; Groll, J. Additive Manufacturing of Scaffolds with Sub-Micron Filaments via Melt Electrospinning Writing. *Biofabrication* 2015, 7 (3), 035002. <https://doi.org/10.1088/1758-5090/7/3/035002>.
- 26) Chung, S.; Ingle, N. P.; Montero, G. A.; Kim, S. H.; King, M. W. Bioresorbable Elastomeric Vascular Tissue Engineering Scaffolds via Melt Spinning and Electrospinning. *Acta Biomaterialia* 2010, 6 (6), 1958–1967. <https://doi.org/10.1016/j.actbio.2009.12.007>.
- 27) Theron, S. A.; Zussman, E.; Yarin, A. L. Experimental Investigation of the Governing Parameters in the Electrospinning of Polymer Solutions. *Polymer* 2004, 45 (6), 2017–2030. <https://doi.org/10.1016/j.polymer.2004.01.024>.
- 28) Niu, J.; Lin, H.; Xu, J.; Wu, H.; Li, Y. Electrochemical Mineralization of Perfluorocarboxylic Acids (PFCAs) by Ce-Doped Modified Porous Nanocrystalline

- PbO₂ Film Electrode. *Environ. Sci. Technol.* 2012, 46 (18), 10191–10198.
<https://doi.org/10.1021/es302148z>.
- 29) Liu, Y.; Li, X.; Ramakrishna, S. Melt Electrospinning in a Parallel Electric Field. *Journal of Polymer Science Part B: Polymer Physics* 2014, 52.
<https://doi.org/10.1002/polb.23511>.
- 30) Miloh, T.; Spivak, B.; Yarin, A. L. Needleless Electrospinning: Electrically Driven Instability and Multiple Jetting from the Free Surface of a Spherical Liquid Layer. *Journal of Applied Physics* 2009, 106 (11). <https://doi.org/10.1063/1.3264884>.
- 31) Thoppey, N. M.; Bochinski, J. R.; Clarke, L. I.; Gorga, R. E. Edge Electrospinning for High Throughput Production of Quality Nanofibers. *Nanotechnology* 2011, 22 (34), 345301.
- 32) Thoppey, N. M.; Gorga, R. E.; Bochinski, J. R.; Clarke, L. I. Effect of Solution Parameters on Spontaneous Jet Formation and Throughput in Edge Electrospinning from a Fluid-Filled Bowl. *Macromolecules* 2012, 45 (16), 6527–6537.
- 33) Roman, M. P.; Thoppey, N. M.; Gorga, R. E.; Bochinski, J. R.; Clarke, L. I. Maximizing Spontaneous Jet Density and Nanofiber Quality in Unconfined Electrospinning: The Role of Interjet Interactions. *Macromolecules* 2013, 46 (18), 7352–7362.
- 34) Thoppey, N. M.; Gorga, R. E.; Clarke, L. I.; Bochinski, J. R. Control of the Electric Field–Polymer Solution Interaction by Utilizing Ultra-Conductive Fluids. *Polymer* 2014, 55 (24), 6390–6398.
- 35) Weimin, Y.; Haoyi, L. Principle and Equipment of Polymer Melt Differential Electrospinning Preparing Ultrafine Fiber. *IOP Conf. Ser.: Mater. Sci. Eng.* 2014, 64, 012013. <https://doi.org/10.1088/1757-899X/64/1/012013>.

- 36) Komárek, M.; Martinová, L. DESIGN AND EVALUATION OF MELT-ELECTROSPINNING ELECTRODES. undefined 2010.
- 37) Thoppey, N. M.; Bochinski, J. R.; Clarke, L. I.; Gorga, R. E. Unconfined Fluid Electrospun into High Quality Nanofibers from a Plate Edge. *Polymer* 2010, 51 (21), 4928–4936. <https://doi.org/10.1016/j.polymer.2010.07.046>.
- 38) Wang, Q.; Curtis, C. K.; Thoppey, N. M.; Bochinski, J. R.; Gorga, R. E.; Clarke, L. I. Unconfined, Melt Edge Electrospinning from Multiple, Spontaneous, Self-Organized Polymer Jets. *Mater. Res. Express* 2014, 1 (4), 045304. <https://doi.org/10.1088/2053-1591/1/4/045304>.
- 39) Lukas, D.; Sarkar, A.; Pokorny, P. Self-Organization of Jets in Electrospinning from Free Liquid Surface: A Generalized Approach. *Journal of Applied Physics* 2008, 103 (8), 084309. <https://doi.org/10.1063/1.2907967>.
- 40) Bakar, S. S. S.; Fong, K. C.; Eleyas, A.; Nazeri, M. F. M. Effect of Voltage and Flow Rate Electrospinning Parameters on Polyacrylonitrile Electrospun Fibers. *IOP Conf. Ser.: Mater. Sci. Eng.* 2018, 318, 012076. <https://doi.org/10.1088/1757-899X/318/1/012076>.
- 41) Li, Z.; Wang, C. Introduction of Electrospinning; 2013; pp 1–13. https://doi.org/10.1007/978-3-642-36427-3_1.
- 42) Şener, A. G.; Altay, A. S.; Altay, F. Effect of Voltage on Morphology of Electrospun Nanofibers. In 2011 7th International Conference on Electrical and Electronics Engineering (ELECO); 2011; p I-324-I-328.
- 43) Kalluri, L.; Satpathy, M.; Duan, Y. Effect of Electrospinning Parameters on the Fiber Diameter and Morphology of PLGA Nanofibers. *Dental Oral Biology and Craniofacial Research* 2021, 2021 (2), 1–7. <https://doi.org/10.31487/j.DOBCCR.2021.02.04>.

- 44) Zhmayev, E.; Zhou, H.; Joo, Y. L. Modeling of Non-Isothermal Polymer Jets in Melt Electrospinning. *Journal of Non-Newtonian Fluid Mechanics* 2008, 153 (2), 95–108. <https://doi.org/10.1016/j.jnnfm.2007.11.011>.
- 45) Zhou, H.; Green, T. B.; Joo, Y. L. The Thermal Effects on Electrospinning of Polylactic Acid Melts. *Polymer* 2006, 47 (21), 7497–7505. <https://doi.org/10.1016/j.polymer.2006.08.042>.
- 46) Shen, Y.; Liu, Q.; Deng, B.; Yao, P.; Xia, S. Experimental Study and Prediction of the Diameter of Melt-Electrospinning Polypropylene Fiber. *Fibers and Polymers* 2016, 17, 1227–1237. <https://doi.org/10.1007/s12221-016-6303-4>.
- 47) Liu, Y.; Deng, R.; Hao, M.; Yan, H.; Yang, W. Orthogonal Design Study on Factors Effecting on Fibers Diameter of Melt Electrospinning. *Polymer Engineering & Science* 2010, 50 (10), 2074–2078. <https://doi.org/10.1002/pen.21753>.
- 48) Xie, G.; Chen, Z.; Ramakrishna, S.; Liu, Y. Orthogonal Design Preparation of Phenolic Fiber by Melt Electrospinning. *J. Appl. Polym. Sci.* 2015, 132 (38), n/a-n/a. <https://doi.org/10.1002/app.42574>.
- 49) Li, X.; Liu, H.; Wang, J.; Li, C. Preparation and Characterization of Poly(ε-caprolactone) Nonwoven Mats via Melt Electrospinning. *Polymer* 2012, 53, 248–253. <https://doi.org/10.1016/j.polymer.2011.11.008>.
- 50) Buchko, C. J.; Chen, L. C.; Shen, Y.; Martin, D. C. Processing and Microstructural Characterization of Porous Biocompatible Protein Polymer Thin Films. *Polymer* 1999, 40 (26), 7397–7407. [https://doi.org/10.1016/S0032-3861\(98\)00866-0](https://doi.org/10.1016/S0032-3861(98)00866-0).
- 51) Demir, M. M.; Yilgor, I.; Yilgor, E.; Erman, B. Electrospinning of Polyurethane Fibers. *Polymer* 2002, 43 (11), 3303–3309. [https://doi.org/10.1016/S0032-3861\(02\)00136-2](https://doi.org/10.1016/S0032-3861(02)00136-2).

- 52) Deitzel, J. M.; Kleinmeyer, J.; Harris, D.; Beck Tan, N. C. The Effect of Processing Variables on the Morphology of Electrospun Nanofibers and Textiles. *Polymer* 2001, 42 (1), 261–272. [https://doi.org/10.1016/S0032-3861\(00\)00250-0](https://doi.org/10.1016/S0032-3861(00)00250-0).
- 53) Hao, M. F.; Liu, Y.; He, X. T.; Ding, Y. M.; Yang, W. M. Factors Influencing Diameter of Polypropylene Fiber in Melt Electrospinning. *Advanced Materials Research* 2011, 221, 129–134. <https://doi.org/10.4028/www.scientific.net/AMR.221.129>.
- 54) Matabola, K. P.; Moutloali, R. M. The Influence of Electrospinning Parameters on the Morphology and Diameter of Poly(Vinylidene Fluoride) Nanofibers- Effect of Sodium Chloride. *Journal of Materials Science* 2013, 16 (48), 5475–5482. <https://doi.org/10.1007/s10853-013-7341-6>.
- 55) Ki, C. S.; Baek, D. H.; Gang, K. D.; Lee, K. H.; Um, I. C.; Park, Y. H. Characterization of Gelatin Nanofiber Prepared from Gelatin–Formic Acid Solution. *Polymer* 2005, 46 (14), 5094–5102. <https://doi.org/10.1016/j.polymer.2005.04.040>.
- 56) Reneker, D. H.; Chun, I. Nanometre Diameter Fibres of Polymer, Produced by Electrospinning. *Nanotechnology* 1996, 7 (3), 216–223. <https://doi.org/10.1088/0957-4484/7/3/009>.
- 57) Wang, X.; Lin, T.; Wang, X. Use of Airflow to Improve the Nanofibrous Structure and Quality of Nanofibers from Needleless Electrospinning. *Journal of Industrial Textiles* 2015, 45 (2), 310–320. <https://doi.org/10.1177/1528083714537100>.
- 58) Li, X.; Liu, Y.; Peng, H.; Ma, X.; Fong, H. Effects of Hot Airflow on Macromolecular Orientation and Crystallinity of Melt Electrospun Poly(L-Lactic Acid) Fibers. *Materials Letters* 2016, 176, 194–198. <https://doi.org/10.1016/j.matlet.2016.04.070>.

- 59) Zhmayev, E.; Cho, D.; Joo, Y. Nanofibers from Gas-Assisted Polymer Melt Electrospinning. *Polymer* 2010, 51, 4140–4144.
<https://doi.org/10.1016/j.polymer.2010.06.058>.
- 60) Yang, Q.; Li, Z.; Hong, Y.; Zhao, Y.; Qiu, S.; Wang, C.; Wei, Y. Influence of Solvents on the Formation of Ultrathin Uniform Poly(Vinyl Pyrrolidone) Nanofibers with Electrospinning. *Journal of Polymer Science Part B: Polymer Physics* 2004, 42 (20), 3721–3726. <https://doi.org/10.1002/polb.20222>.
- 61) Pham, Q. P.; Sharma, U.; Mikos, A. G. Electrospun Poly(ϵ -Caprolactone) Microfiber and Multilayer Nanofiber/Microfiber Scaffolds: Characterization of Scaffolds and Measurement of Cellular Infiltration. *Biomacromolecules* 2006, 7 (10), 2796–2805.
<https://doi.org/10.1021/bm060680j>.
- 62) Zhang, C.; Yuan, X.; Wu, L.; Han, Y.; Sheng, J. Study on Morphology of Electrospun Poly(Vinyl Alcohol) Mats. *European Polymer Journal* 2005, 41 (3), 423–432.
<https://doi.org/10.1016/j.eurpolymj.2004.10.027>.
- 63) Brown, T. D.; Dalton, P. D.; Hutmacher, D. W. Direct Writing By Way of Melt Electrospinning. *Advanced Materials* 2011, 23 (47), 5651–5657.
<https://doi.org/10.1002/adma.201103482>.
- 64) Nayak, R.; Ilias, bullet; Kyratzis, I.; Yen, bullet; Truong, Y.; Rajiv, bullet; bullet, P.; Arnold, L. Melt-Electrospinning of Polypropylene with Conductive Additives. *Journal of Materials Science* 2012, 47, 6387–6396. <https://doi.org/10.1007/s10853-012-6563-3>.
- 65) Wang, X.; Huang, Z. Melt-Electrospinning of PMMA. *Chin J Polym Sci* 2010, 28 (1), 45–53. <https://doi.org/10.1007/s10118-010-8208-9>.

- 66) Li, H.; Chen, H.; Zhong, X.; Wu, W.; Ding, Y.; Yang, W. Interjet Distance in Needleless Melt Differential Electrospinning with Umbellate Nozzles. *Journal of Applied Polymer Science* 2014, 131 (15). <https://doi.org/10.1002/app.40515>.
- 67) Hutmacher, D. W.; Dalton, P. D. Melt Electrospinning. *Chemistry – An Asian Journal* 2011, 6 (1), 44–56. <https://doi.org/10.1002/asia.201000436>.
- 68) Zhiyuan, C.; He, J.; Fengwen, Z.; Yuexing, L.; Yong, L.; Huilin, Y. Effect of Polar Additives on Melt Electrospinning of Nonpolar Polypropylene. *Journal of the Serbian Chemical Society* 2014, 79 (5), 587–596.
- 69) Malakhov, S. N.; Khomenko, A. Yu.; Belousov, S. I.; Prazdnichnyi, A. M.; Chvalun, S. N.; Shepelev, A. D.; Budyka, A. K. Method of Manufacturing Nonwovens by Electrospinning from Polymer Melts. *Fibre Chem* 2009, 41 (6), 355–359. <https://doi.org/10.1007/s10692-010-9204-0>.
- 70) Malakhov, S. N.; Dmitryakov, P. V.; Pichkur, E. B.; Chvalun, S. N. Nonwoven Materials Produced by Melt Electrospinning of Polypropylene Filled with Calcium Carbonate. *Polymers* 2020, 12 (12), 2981. <https://doi.org/10.3390/polym12122981>.
- 71) Angamma, C. J.; Jayaram, S. H. Analysis of the Effects of Solution Conductivity on Electrospinning Process and Fiber Morphology. *IEEE Transactions on Industry Applications* 2011, 47 (3), 1109–1117. <https://doi.org/10.1109/TIA.2011.2127431>.
- 72) Zong, X.; Kim, K.; Fang, D.; Ran, S.; Hsiao, B. S.; Chu, B. Structure and Process Relationship of Electrospun Bioabsorbable Nanofiber Membranes. *Polymer* 2002, 43 (16), 4403–4412. [https://doi.org/10.1016/S0032-3861\(02\)00275-6](https://doi.org/10.1016/S0032-3861(02)00275-6).
- 73) Choi, J. S.; Lee, S. W.; Jeong, L.; Bae, S.-H.; Min, B. C.; Youk, J. H.; Park, W. H. Effect of Organosoluble Salts on the Nanofibrous Structure of Electrospun Poly(3-

- Hydroxybutyrate-Co-3-Hydroxyvalerate). *Int J Biol Macromol* 2004, 34 (4), 249–256.
<https://doi.org/10.1016/j.ijbiomac.2004.06.001>.
- 74) Multifactorial Modeling and Optimization of Solution and Electrospinning Parameters to Generate Superfine Polystyrene Nanofibers. <https://doi.org/10.1002/adv.21947>.
- 75) Nitanan, T.; Akkaramongkolporn, P.; Ngawhirunpat, T.; Rojanarata, T.; Panomsuk, S.; Opanasopit, P. Fabrication and Evaluation of Cationic Exchange Nanofibers for Controlled Drug Delivery Systems. *International journal of pharmaceutics* 2013.
<https://doi.org/10.1016/j.ijpharm.2013.04.031>.
- 76) Varnaite-Zuravliova, S.; Savest, N.; Baltušnikaitė-Guzaitienė, J.; Abraitienė, A.; Krumme, A. Electrospinning of Chitosan Biopolymer and Polyethylene Oxide Blends. *Autex Research Journal* 2019, 20. <https://doi.org/10.2478/aut-2019-0031>.
- 77) Jin, H.-J.; Fridrikh, S. V.; Rutledge, G. C.; Kaplan, D. L. Electrospinning Bombyx Mori Silk with Poly(Ethylene Oxide). *Biomacromolecules* 2002, 3 (6), 1233–1239.
<https://doi.org/10.1021/bm025581u>.
- 78) Tan, S.-H.; Inai, R.; Kotaki, M.; Ramakrishna, S. Systematic Parameter Study for Ultra-Fine Fiber Fabrication via Electrospinning Process. *Polymer* 2005, 46 (16), 6128–6134.
<https://doi.org/10.1016/j.polymer.2005.05.068>.
- 79) Uyar, T.; Besenbacher, F. Electrospinning of Uniform Polystyrene Fibers: The Effect of Solvent Conductivity. *Polymer* 2008, 49, 5336–5343.
<https://doi.org/10.1016/j.polymer.2008.09.025>.
- 80) Heikkilä, P.; Harlin, A. Electrospinning of Polyacrylonitrile (PAN) Solution: Effect of Conductive Additive and Filler on the Process. *Express Polymer Letters* 2009, 3 (7), 437–445. <https://doi.org/10.3144/expresspolymlett.2009.53>.

- 81) Malakhov, S. N.; Belousov, S. I.; Bakirov, A. V.; Chvalun, S. N. Electrospinning of Non-Woven Materials from the Melt of Polyamide-6 with Added Magnesium, Calcium, and Zinc Stearates. *Fibre Chem* 2015, 47 (1), 14–19. <https://doi.org/10.1007/s10692-015-9631-z>.
- 82) König, K.; Balakrishnan, N.; Hermanns, S.; Langensiepen, F.; Seide, G. Biobased Dyes as Conductive Additives to Reduce the Diameter of Polylactic Acid Fibers during Melt Electrospinning. *Materials* 2020, 13, 1055. <https://doi.org/10.3390/ma13051055>.

CHAPTER 2

Increasing ionic conductivity within thermoplastics via commercial additives results in a dramatic decrease in fiber diameter from melt electrospinning

Neelam Sheoran, Brent Boland, Samuel Thornton, Jason R. Bochinski, and Laura I. Clarke**

N. Sheoran, B. Boland, S. Thornton, Prof. J. R. Bochinski, and Prof. L. I. Clarke
Department of Physics, North Carolina State University, Raleigh, NC 27695-8202,
United States
Email: jason_bochinski@ncsu.edu and laura_clarke@ncsu.edu

Abstract

Polyethylene melt conductivity was increased by adding a commercial anti-static agent, which resulted in a 20× decrease in electrospun fiber diameter and formation of a significant fraction of sub-micron diameter fibers. Two polyethylene formulations and varying additive concentrations were utilized to span the parameter space of conductivity and viscosity. The key role of conductivity in determining the jet radius (which sets the upper limit on the fiber size) is discussed in the context of fluid mechanics theory and previous simulations. Parameters which affect the conversion of the liquid jet to a solid fiber and the pertinent theory are outlined. An "unconfined" experimental configuration is utilized to avoid parasitic effects associated with melt electrospinning such as needle clogging and to enable direct observation of important characteristic length scales related to the interaction of the fluid and the applied electric field. In this approach, the fluid spontaneously forms an array of cone perturbations which act as stationary "nozzles" through which the mobile fluid flows to form the jet. The experimental data and theory considerations allow for a holistic discussion of the interaction between flow rate, viscosity, conductivity, and the resultant jet and fiber size. Information about the fluid viscosity and conductivity gained by observing the electrospinning process is highlighted. Schemes for theoretically predicting the cone-jet density, cone size, and flow rate are compared to experimental results.

Keywords: melt electrospinning, thermoplastics, ionic conductivity

2.1. Introduction

Polymeric fibers are utilized in a wide variety of high societal impact applications such as wound dressings, water and air filters, and tissue scaffolds.¹⁻⁵ Solvent-free nano- and meso-scale diameter fibers made from mechanically strong thermoplastic polymers would be particularly valuable for many of these products. Such small fibers result in material with a very high surface-to-volume ratio and ample open space, facilitating high efficiency and long lifetime without clogging for filtration applications,⁶⁻¹¹ as well as enabling cells to organize into tissues in an environment which is morphologically similar to that in nature for biomedical applications.¹²⁻¹⁵ Solvent-free nanofiber production eliminates concerns of trace solvent contamination in the final product and the negative human health and environmental consequences of using solvent in manufacturing. Use of high molecular weight, highly-entangled commercial polymers would ensure the resultant fibers have sufficient mechanical strength for higher pressure applications like filtration. Yet creating nanofibers directly from molten substances is problematic due in part to the high viscosity of polymer melts^{3, 16}; this is particularly true for highly-entangled mechanically-strong materials. Electrospinning^{12, 17-20} is a common technique to fabricate nanofibers, which in principle can use any entangled fluid. However, in practice, melt electrospinning has been strikingly unpopular: fewer than 6% of electrospinning scientific publications appearing in the last decade specifically address melt systems,²¹ with the vast majority utilizing polymer solutions. As previously reported,²² some of the challenges with melt electrospinning can be addressed by replacing the traditional single metal needle through which a highly-viscous melt must be pumped with an unconfined configuration²³⁻²⁷ (e.g., a thin film of molten polymer on a flat metal plate). Jets spontaneously form on the sharp-edged plate, which eliminates clogging, enables many

simultaneous jetting sites, and allows control of the jet size via tuning of the melt properties and electric field strength.

In this work, using a combination of theory and data, the fundamental relationships that underlie electrospinning of low conductivity, high viscosity polymer melts (i.e., the melts formed by thermoplastics) are discussed. A particular focus is the underexplored role of low innate ionic conductivity. Electrospinning relies on the fluid having a moderate level of mobile ions: when an electric field is applied, ions move under the influence of the field, causing surface charges. This charged fluid then experiences a force due the electric field and/or charge repulsion, which ultimately propels it towards the collector.^{28, 29} When utilizing solution-based electrospinning, there are multiple potential ion sources; however in an additive-free molten thermoplastic the only ions present are due to chain defects or unintentional thermal degradation. All commercial thermoplastics have proprietary additive packages which might include antioxidants or other thermal stabilizers to prevent degradation, as well as whitening agents.^{30, 31} Such small molecule additives, which are introduced to serve different purposes, are most likely the serendipitous origin of ions which make melt electrospinning of these systems possible. The conductivity created by these sources is usually not measured nor optimized.

In this work, the ionic conductivity of polyethylene (the most common commodity thermoplastic worldwide) is altered, demonstrating that increasing the melt conductivity to levels typically found in solution-based electrospinning results in a 20× decrease in fiber diameter. This outcome, verified for two polyethylene formulations with significantly different physical properties, highlights that ionic conductivity is an overlooked fundamental characteristic which strongly affects electrospinning outcomes. Measuring and altering ionic conductivity enables a clearer delineation of the challenges in melt electrospinning, determining the various roles that high

viscosity, lack of solvent loss, and low ion concentration and motion play in producing larger diameter fibers. By incorporating a readily-available, inexpensive commercial thermoplastic additive (e.g., an anti-static agent) at a low doping level, significant increase in molten ionic conductivity and concurrent decrease in fiber diameter was accomplished. We present measurements of ionic conductivity and viscosity as a function of temperature, describe changes in the electrospinning process, including cone size and cone-jet density, and apply theoretical analysis to explain alteration of each pertinent length scale including the resultant fiber size.

2.2. Results and Discussion

2.2.1. Selection of materials and material properties

Polyethylene was selected as a target material because despite its ubiquitous commercial presence, it is rarely used for melt electrospinning.³²⁻³⁵ However, linear low-density polyethylene (LLDPE) is often utilized in microfiber form and has good mechanical properties (e.g., ASPUN is designed for fiber applications). Two different LLDPE formulations were utilized: ASPUN 6850a (ASPUN) has a moderate viscosity and contains a standard additive package while DNDA 1082 (DNDA) is a specialty formulation with a minimal additive package and a lower viscosity. Figure 2.1 summarizes viscosity and conductivity measurements versus temperature for the two materials. At 195 °C - the temperature used for electrospinning in this work - the viscosity of DNDA is ~25% that of ASPUN (Figure 2.1a). The data was taken with decreasing temperature, thus the sudden increase at ~120 °C is due to polymer solidification. At the working temperature, the two unmodified polyethylene formulations (i.e., as received from the manufacturer) have similar conductivity values $\sim 7 \times 10^{-10}$ S/cm (Figure 1b). For comparison, the conductivity of solutions utilized for electrospinning typically falls in the range $10^{-6} - 10^{-4}$ S/cm; e.g., 4 - 6 % (w/w)

polyethylene oxide/water solution, which is a common nanofiber-forming, electrospinning fluid,^{26, 27} has a conductivity of $\sim 8 \times 10^{-5}$ S/cm.

To controllably increase the electrical conductivity of the LLDPE melts, the anti-static agent Hostastat FA38 (FA38) was utilized as a dilute ionic supplement. A commercially available additive designed to be homogeneously incorporated into thermoplastics avoided chemical incompatibility or ineffective mixing between the melt and additive. Conventional antistatic agents generally combine hydrophobic and hydrophilic (e.g., phosphate and fatty acid esters) structures, and work by migrating to the surface of the polymer material in order to absorb water and ions from the air and improve the surface conductivity. This process may be a portion of the conductivity effect pertinent in this work, with bulk conduction due to ions likely also contributing. Ionic conductivity measurements versus temperature at 0.0, 0.1 and 5.0 weight percent (wt%) FA38 loading for the two LLDPE formulations are presented in Figure 2.1b. Focusing on the data at 195 °C (Figure 1, vertical green line) which is most pertinent for electrospinning, the DNDA [ASPUN] melt conductivity increased by $\sim 20\times$ [$\sim 40\times$] from 6.8×10^{-10} [7.3×10^{-10}] S/cm as received to 1.6×10^{-8} [3.0×10^{-8}] S/cm at the 5.0 wt% FA38 loading level. The dashed black line represents the measurement lower limit (due to the electrode) as a function of temperature. Figure 2.1a shows the complex viscosity as a function of temperature for ASPUN and DNDA with 0.0, 0.1, and 5.0 wt% FA38 additive. The change in viscosity due to the additive is less than 20%.

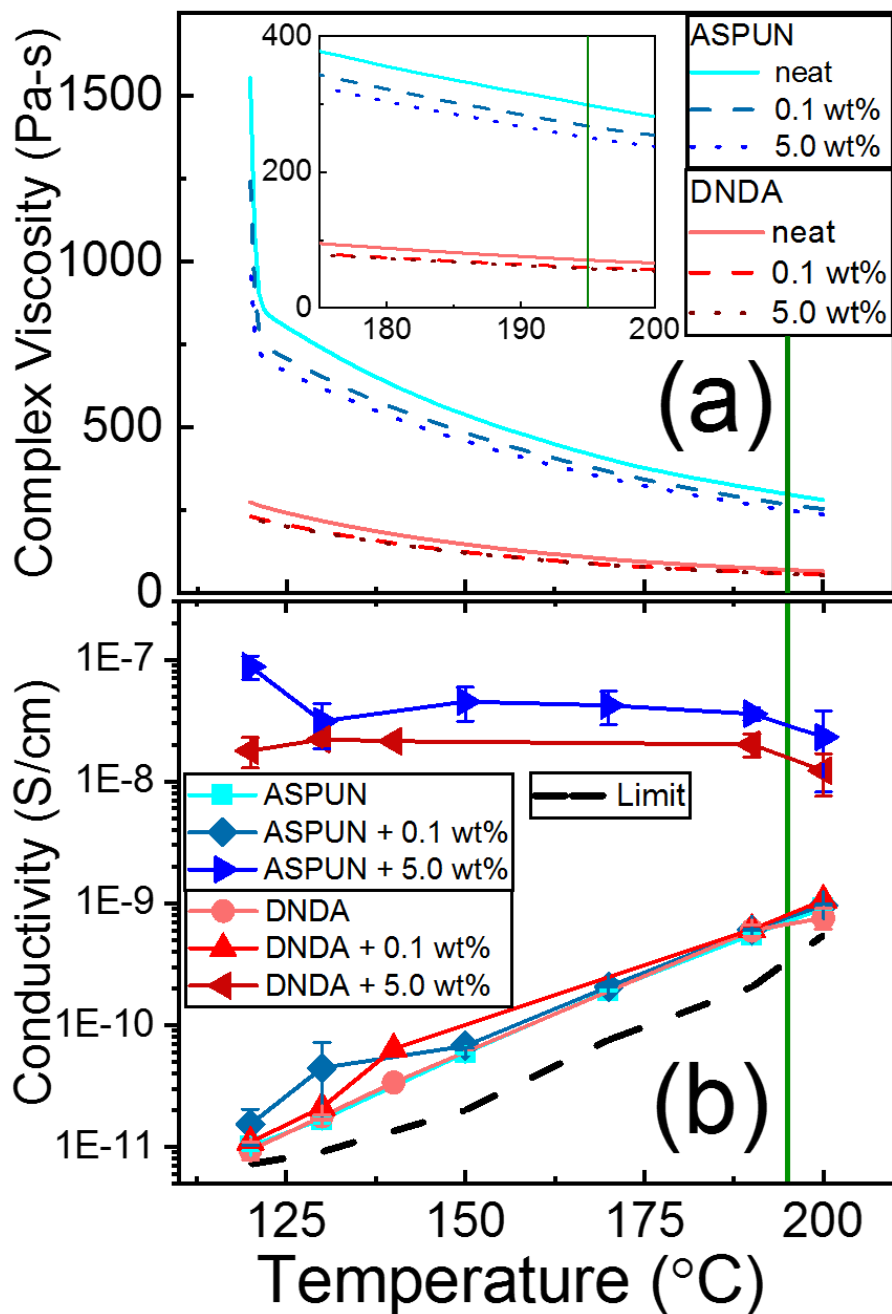


Figure 2.1. a) Viscosity as a function of temperature for ASPUN (blue data) and DNDA (red data) with 0.0, 0.1, and 5.0 wt% FA38 additive (solid, dashed, and dotted lines), respectively. Inset: a magnified view of region 0 – 400 Pa-s and 175 – 200 °C. b) Ionic conductivity as a function of polymer melt temperature for ASPUN (blue data; square, diamond, right-facing triangle symbols) and DNDA (red data; circle, triangle, left-facing triangle symbols) with 0.0, 0.1, and 5.0 wt% FA38 additive, respectively. The green vertical lines indicate the approximate polymer temperature used during the electrospinning process (~195 °C).

2.2.2. Spontaneous fingering to form cone-jets

The unconfined electrospinning apparatus, electric field pattern generated, and coordinate system utilized for this work are described in detail in Experimental Methods. Polymer melt resides on a grounded, heated horizontally-oriented plate with a sharp edge. A nearby vertically-oriented plate serves as a collector and is held at a large negative voltage. The electric field pattern generated has a maximum magnitude at the sharp plate edge. After voltage is applied, the edge of the polymer melt film extends slightly ($\sim 300 - 800 \mu\text{m}$) past the plate edge in the direction towards the collector; we refer to this length scale as the x -extension. The nominal thickness of the polymer melt on the source plate is 1.8 mm. When voltage is applied, the thickness of the fluid extending past the plate edge is in the range of $200 - 600 \mu\text{m}$ (referred to as the y -extension). The extension lengths are smaller for the lower viscosity case, as discussed in Section 2.2.3.1. As further discussed below, the x - and y - extensions are part of a series of characteristic length scales that describe how the fluid is affected by the electric field, which also includes the characteristic cone size and the jet size and length. These quantities depend on the melt ionic conductivity.

The cone-jet initiation process occurs as follows: Ions within the melt experience forces due to the applied electric field, which leads to an excess of positive charges accumulating near the leading edge of the fluid. The charged melt near the edge of the plate expands, moving in the direction of the applied field (i.e., toward the collector). Surface tension works against such an expansion and the resultant instability causes the polymer melt to spontaneously finger to form many small protrusions, which ultimately transition into fiber forming cone-jets.²²⁻²⁷

This process is illustrated in Figure 2.2 for the as-received polyethylene formulations.

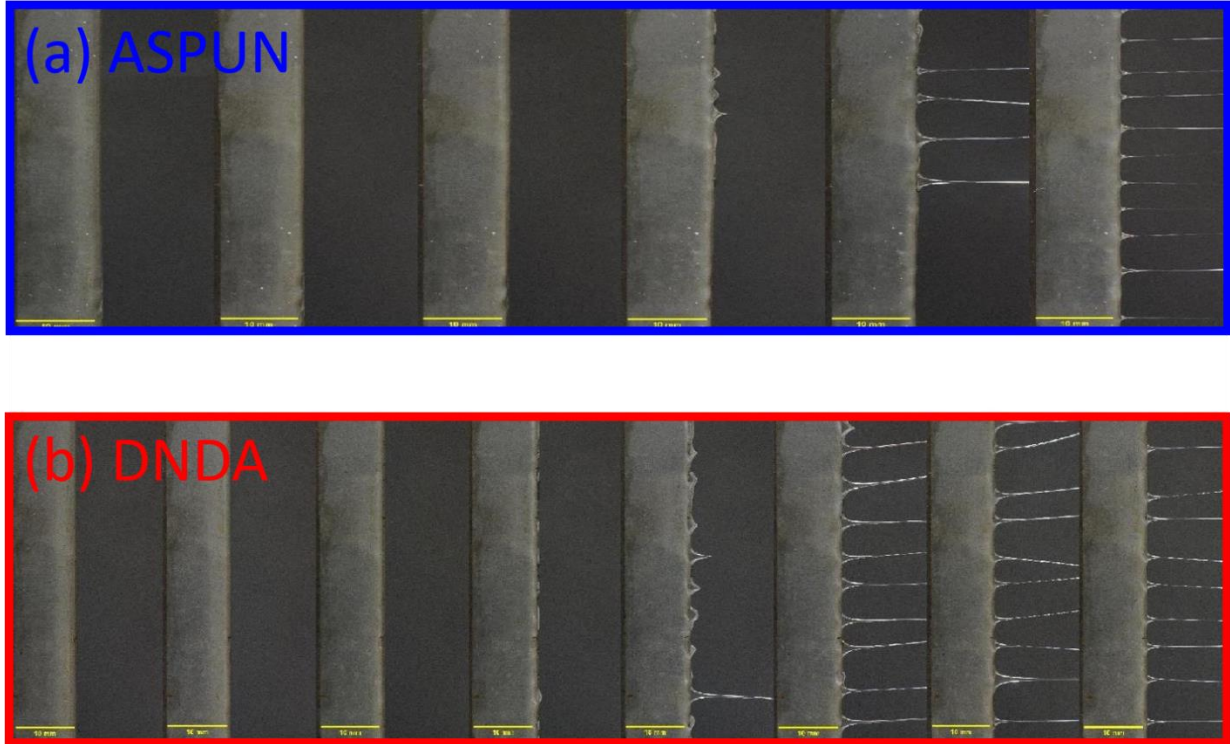


Figure 2.2. Top-down view of a sequence of photographic images of the spinning plate edge during the formation of protrusions and jets. The time sequence starting from $t = 0$ s, with images taken every 60 seconds (15 seconds) respectively, from left to right for ASPUN (DNDA). The scale bar represents 1 cm in each image.

The process of fingering and then cone-jet formation begins with a spontaneous fluctuation of the expanded fluid. As a result, both the time between application of the applied field and appearance of the first finger perturbation and the time required to reach the steady-state number of cone-jets are viscosity-dependent. The approximate time for the first finger perturbation to occur^{22, 36} is given as:

$$\text{Time for first perturbation} = \left(\frac{2\eta}{h^2}\right) \frac{27\gamma^2}{4\epsilon_0^3 E^6} \quad (1),$$

where h is the film thickness (i.e., y -extension), η is the viscosity, E is the electric field at the location where fingering begins, and γ is the surface tension. (Equation 1 (varying only by a co-factor of 12 versus 13.5) can also be derived by analogy with Rayleigh-Taylor instabilities,³⁷

substituting the electric force for gravity, and identifying h as a capillary length (see Section 2.2.3.1) which establishes relationships between h , γ , and E .)

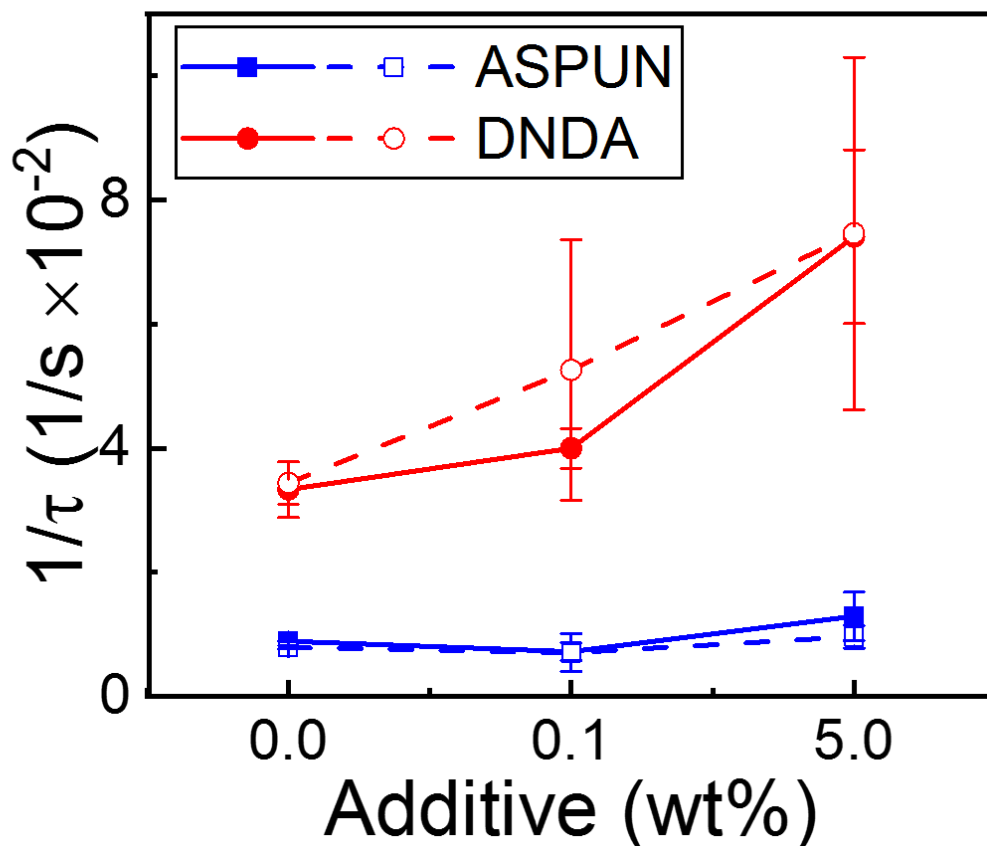


Figure 2.3. Inverse average time to spontaneous perturbation formation at the plate edge $1/\tau$ as a function of additive FA38 wt% for two different formulations of LLDPE. Solid lines with filled symbols (dashed lines with open symbols) are experimental (theoretical, Equation 1) $1/\tau$ values for ASPUN (blue square symbols) and DNDA (red circle symbols), respectively.

For instance, at the working electrospinning temperature of 195 °C, the viscosity of DNDA and ASPUN are 70 ± 2 and 300 ± 9 Pa-s, respectively. After field application, the first finger perturbation for neat DNDA formed within 30 ± 4 seconds while this process took 112 ± 5 seconds for neat ASPUN. A comparison of experimental and theoretical values for the time to first perturbation is presented in Figure 2.3. For theoretical calculations, the y-extension (h) was

determined by imaging (after jet formation as discussed below) and the simulated electric field value used was from this y -extension and $1.3\times$ the x -extension measured at steady state, which is consistent with visual observations prior to, and during, the spontaneous fingering process. Thus, the fluid edge pulls back slightly in the x direction after cone-jet formation.

After the protrusions form and organize, a steady-state is reached in which the cone-jets are approximately evenly spaced over the length of the plate and the x - and y -extensions are similar in size. A summary of the jet number as a function of time, including the steady state values is presented in Figure 2.4.

The characteristic spacing λ between two cone-jets can be predicted using the equation^{22, 36}

$$\lambda = \left(\frac{3\pi}{\epsilon_0}\right) \frac{\gamma}{E^2} \quad (2),$$

where E is the electric field at the location of the fluid edge in steady state. Equation 2 arises from determining the wavenumber where the growth rate (a generalization of Equation 1) for perturbations is maximized. (Again, this expression (with a co-factor of $2\pi\sqrt{2}$ versus 3π) can also be derived using an analogy with Rayleigh-Taylor instabilities³⁷ and substituting the gravity force with electric force.) Theoretical estimates, using simulated electric field values at the experimentally observed x - and y -extensions and a constant value of $\gamma = 33.1 - 0.0390*T(^{\circ}\text{C})$ mN/m with $T = 195^{\circ}\text{C}$ as the surface tension of polyethylene³⁸ for all cases, are compared with experimental values in Figure 4c; the agreement is good. For the neat polymer, the experimental (theoretical) λ values for DNDA and ASPUN are 4.19 ± 0.15 mm (4.15 ± 0.21 mm), and 5.32 ± 0.40 mm (5.47 ± 0.58 mm), respectively. The physics of this initial process was described in more detail in previous works.^{22, 23, 26} Overall, these experiments confirm that the surface tension is not significantly altered by addition of the additive.

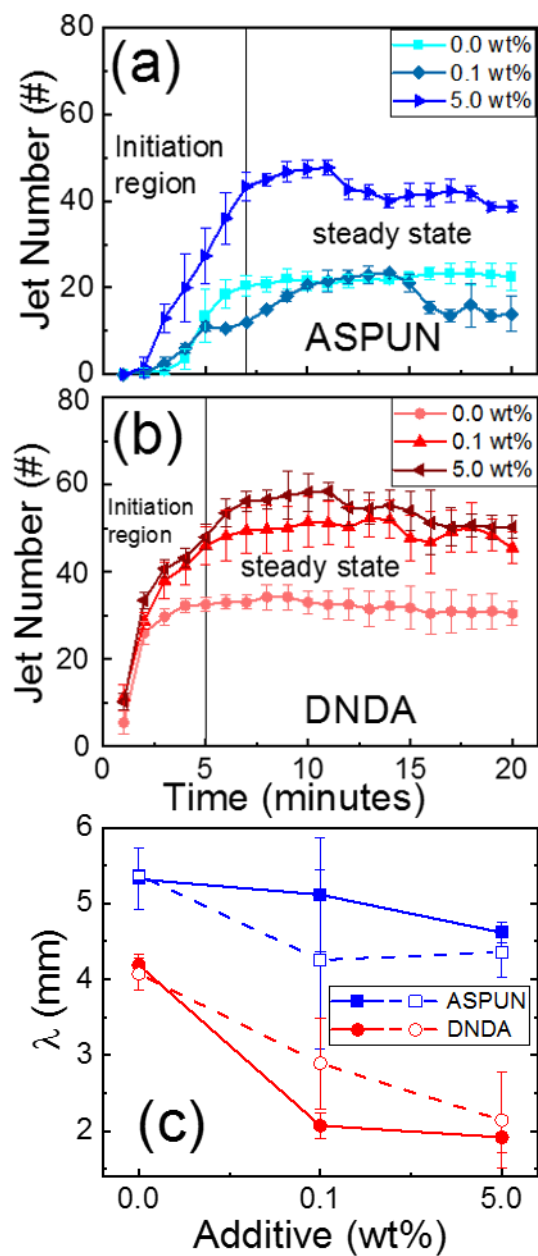


Figure 2.4. Plot of observed jet number versus time. Measurements were performed by counting the number of jet sites every minute using video images for (a) ASPUN (blue data; square, diamond, right-facing triangle symbols) and (b) DNDA (red data; triangle, circle, left-facing triangle symbols) with 0.0, 0.1, and 5.0 wt% FA38 additive, respectively. The polymer melt temperature was held at 195 °C and -45 kV was applied to the collector. (c) Steady state values for each case with experimental data (filled symbols) compared to theoretical values (open symbols) from Equation 2.

2.2.3. Additional characteristic length scales

Parameters such as electrical conductivity K , viscosity, flow rate Q , surface tension, and electric field strength combine to determine the characteristic size of each feature of the electrospinning process: jet-to-jet spacing, cone width, x - and y -extension length, jet width, jet length, and ultimately, the final fiber size, as summarized in Figure 2.5. In this section, mathematical expressions (utilizing previous treatments^{37, 39, 40}) for each additional pertinent length scale, along with the flow rate, beginning at the plate edge and moving outward, are presented, discussed, and connected to experimental data.

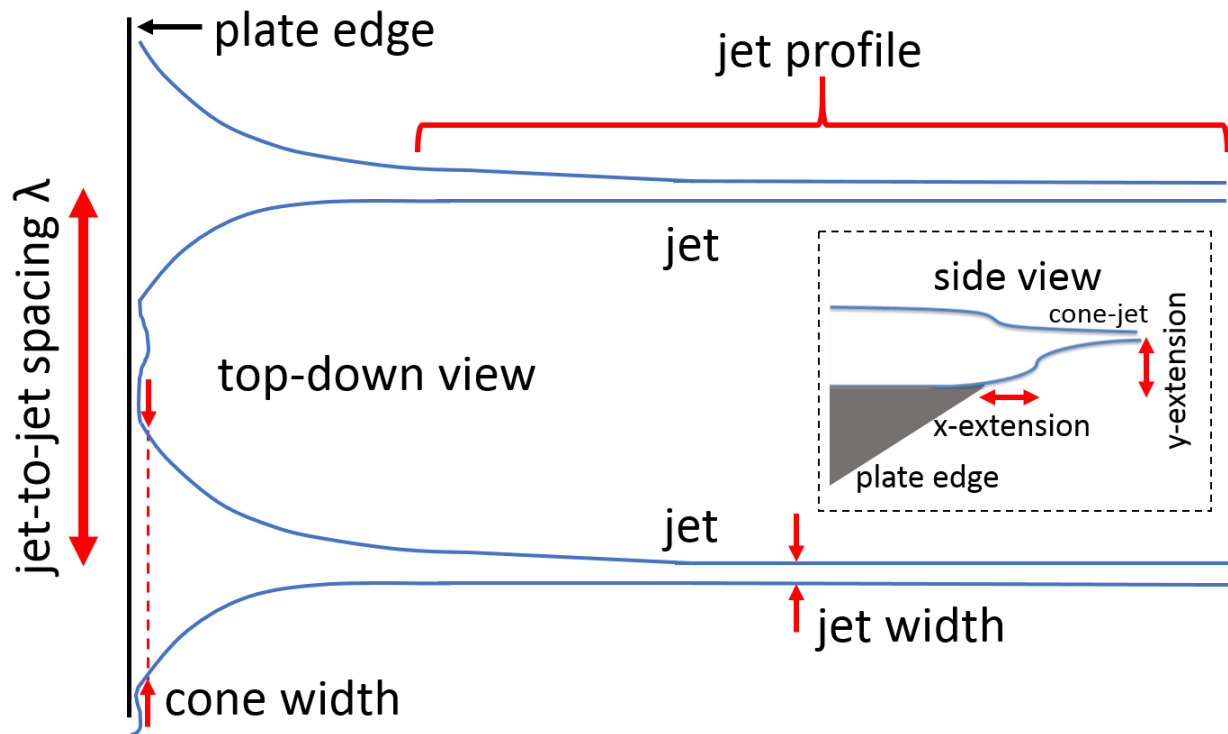


Figure 2.5. Schematic depiction of the characteristic length scales in the melt electrospinning process from a top-down and side view perspective, respectively.

2.2.3.1. Capillary length - understanding the fluid position on the plate and the cone width

The x - and y -extensions are similar to a meniscus formed by the fluid on the plate. In a classic meniscus,³⁷ the size is related to the capillary length $\kappa_{gravity}^{-1} = \sqrt{\gamma/\rho g}$ where ρ is the mass density and g is the acceleration due to the gravity. The capillary length is the distance over which the force of gravity (due to the small mass) is negligible and thus capillary forces (i.e., those associated with surface tension) dominate. It can also be interpreted as a screening length: that is, the distance needed for the fluid to relax to a flat sheet moving away from a disturbance (e.g., the plate). An analogous approach can be utilized for the present experiment where the balance is between electric and capillary forces. Balancing the capillary and electric pressures (in direct analogy with the gravity derivation)³⁷ is $\gamma/\kappa^{-1} = \sigma E = \epsilon_0 E^2$ (where σ is the surface charge density, the boundary condition $E_{out} - E_{in} = \sigma/\epsilon_0$ has been used, and complete screening of the electric field $E_{in} = 0$ is assumed), which results in

$$\kappa^{-1} = \frac{\gamma}{\epsilon_0 E^2} \quad (3).$$

Using the electric field at the observed x - and y -extensions and the known surface tension results in capillary length values which match the observed extensions (Figure 2.6a). Thus, the data is consistent with Equation 3. Thinking physically, when the electric field has just been applied, the thickness of the film on the plate is 1.8 mm, which results in a capillary pressure of around 10 N. (The gravity capillary length is ca. 1.7 mm; thus gravity effects should be minimal.) The electric pressure (i.e., pressing outward towards the collector) is > 80 N. Thus, as a consequence the fluid will move forward and thin. Thinning increases the capillary pressure (and, due to the experimental configuration utilized here, moving forward in the $+x$ direction decreases the electric field). At the stationary point, the two pressures balance, which sets the x - and y -extension values. Using order of magnitude calculations, the assumption (based on experimental observations) that

x - and y -extension values are similar at the final fluid edge location, and the known dependence of the electric field, this point occurs around 400 μm , which matches well with the experimental results (Figure 2.6a).

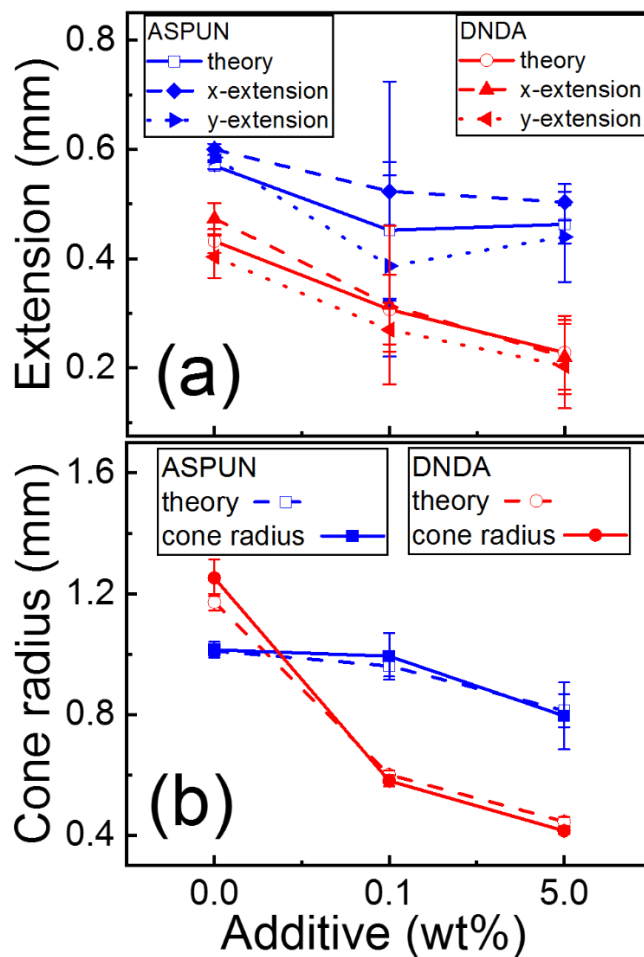


Figure 2.6. a) Position of the fluid edge relative to the plate edge (i.e., x -extension and y -extension) as a function of additive loading wt%. Experimental values (filled symbols) are measured for x - (diamond (ASPUN) and triangle (DNDA) symbols) and y -extensions (right-facing triangle (ASPUN) and left-facing triangle (DNDA) symbols), while theoretical values (open symbols) (square (ASPUN) or circle (DNDA) symbols) are calculated from Equation 3 using the electric field simulation value at the observed x - and y -extension location. b) Cone width as a function of FA38 loading wt%. The different PE formulations are ASPUN (blue data) and DNDA (red data), with experimental values (filled symbols) and theoretical values (from Equation 3, open symbols) respectively.

Melts with higher conductivity and lower viscosity have systematically lower x - and y -extensions. We find that the experimental x - and y - extension values depend on η to a power of ca. 0.3 to 0.7. The change in x - and y -extensions has a weaker dependence on conductivity, varying as K to the power of -0.1 to -0.3.

The stationary cone region around each jet can also be interpreted as a meniscus, where in this case the disturbance is the motion of the fluid in the jet region. Thus, the cone radius can also be estimated by the capillary length (see Equation 3) with E the electric field at the terminal end of the cone (which is approximately $1.5\times$ the cone radius). The comparison between the experimental data and theoretical estimates of the cone widths are presented in Figure 2.6b.

Finally, identifying the y -extension as a capillary length, enables a re-examination of Equation 1, the time to first perturbation. Using $h \approx \gamma/\epsilon_0 E^2$ enables the simplification to time $\approx 27\eta h/2\gamma$. γ/η is the characteristic fluid velocity^{39, 40} and the time is proportional to the capillary length, divided by this characteristic velocity. Because surface tension is relatively constant and the dependence of h on conductivity is weak, this simplification indicates that melt viscosity has the strongest effect on the perturbation time: for the example case discussed in Section 2.2.2, a 4.3-fold increase in viscosity decreases the time by a factor of 3.7. The influence of the conductivity will occur in decreasing the capillary length, which results in a faster time (see Section 2.2.7). The capillary length also appears in Equation 2, where its classic identification as related to the inverse characteristic wavenumber (κ^{-1})³⁷ leads to $\kappa \sim 2\pi/\lambda$ or $\lambda \sim 2\pi\kappa^{-1}$.

2.2.3.2. Jet radius, jet length, and flow rate

While capillary lengths and cone-jet spacing provide useful visual evidence of changes in conductivity, the jet width has a direct impact on the ultimate fiber diameter, serving as the upper limit. The jet size for a viscous fluid is given by:

$$r_{jet} = r_{cross} = \frac{\eta^{1/2} Q^{1/3} \epsilon_0^{1/6}}{K^{1/4} E^{1/6}} \quad (4),$$

with E is the electric field at the "cross-over" point as discussed below.^{39, 40} Equation 4 results from a particular model in which flow Q is pushed through a circular hole (having radius a) in a flat plate and the electric field is uniform; however, this expression can be more generally applied. In this model and associated detailed simulations, near the source plate current is initially generated by volumetric flow (i.e., ions moving with the fluid) however, as the jet develops, ions move to the surface and the primary current mode becomes surface convention. The "jet radius" is identified as the crossover point r_{cross} where these two types of current are the same order of magnitude. Although the process is continuous, to simplify the discussion, for x (i.e., the coordinate direction that connects the source and collector plates) values less than this crossover point, one can think of the cone as transforming into a jet. For x values greater than this point, the jet is transforming into a fiber. The x value where the crossover occurs (the "jet length") is estimated by:

$$\ell_{jet} = x_{cross} \sim \frac{\eta^{1/3} Q^{1/3}}{\epsilon_0^{1/3} E^{2/3}} \quad (5),$$

where E is the electric field at the crossover point, as in Equation 4. Thus, when considering $r(x)$, $r(x_{cross}) = r_{cross}$. For the viscous, low conductivity fluids where Equation 4 is applicable, x_{cross} is a reasonable distance from the plate edge: for the conditions explored in this work, 2 – 3 mm, where visually the cone has transitioned into a nearly parallel-sided jet. In practice, when applying Equation 4 and 5 to experimental data $r(x)$, an iterative approach was utilized to self-consistently determine r_{cross} and x_{cross} , which both depend on the value of E at the location $x = x_{cross}$.

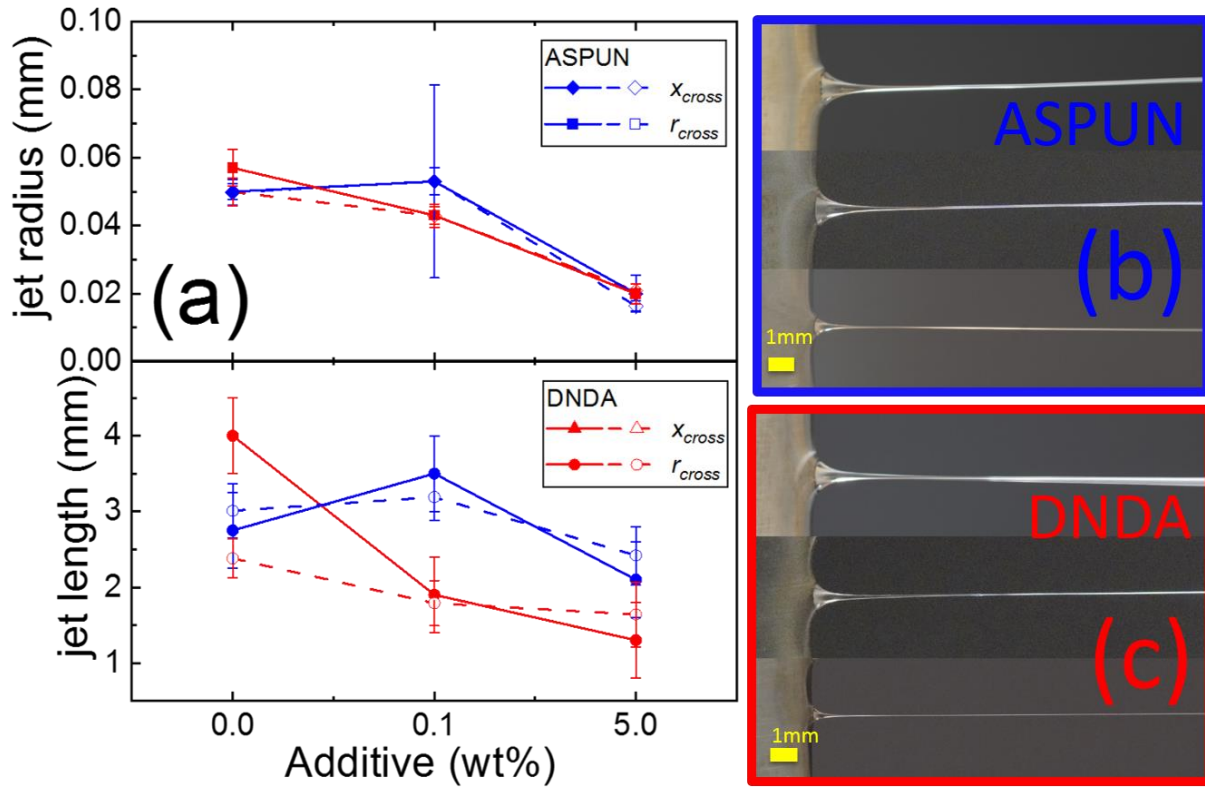


Figure 2.7. a) Measured experimental values (filled symbols) for the characteristic jet radius r_{cross} and length x_{cross} compared with theoretical predictions (open symbols) from Equation 4 and 5 for ASPUN (blue data) and DNDA (red data), respectively. As discussed in the text, $x_{cross} \sim a$. For this data group, we find $x_{cross} = 1.5a$ on average. Images of the jets at different additive loading levels 0.0, 0.1, and 5.0 wt% from top to bottom for b) ASPUN and c) DNDA.

From this analysis, we determined that the co-factor for Equation 5 is approximately 3 for the conditions utilized in this work. The process of charge transport to the surface is driven by the electric field; because the electric field decreases with distance in our apparatus, this process is elongated over the model prediction. Figure 2.7a summarizes the agreement between experimental data and theoretical estimates of the jet radius r_{cross} and length x_{cross} .

Because flow rate has a large role in determining jet size and, in an unconfined electrospinning configuration, is itself determined by the electric field, Q was modelled by applying classical fluid theory.³⁷ In the lubrication approximation, which is valid for viscous systems at small size scales (i.e., thin films), the average fluid velocity goes as the film thickness squared times the pressure

difference per length divided by the viscosity, with a co-factor of $1/3$.³⁷ This model invokes a thin film supported on a solid substrate with fluid motion parallel to the substrate due to different pressures (e.g., at the two ends of the substrate). The velocity is zero at the fluid-substrate interface and maximized at the free surface, resulting in a quadratic velocity profile perpendicular to the flow direction. For a cone-jet, pressure is associated with the electric field as $\epsilon_0 E^2$, and flow proceeds in the x -direction. A core of fluid moves through the interior of the cone with the exterior region remaining largely stationary (i.e., as though the fluid has formed a nozzle which is immobile except within the innermost region). Considering this interior jet and moving outward radially at a fixed x value, the velocity is maximum at the radial center and almost zero at the transition into the stationary cone. Thus, the radius of the interior jet is analogous to the film thickness. We denote this length scale as a because it is the equivalent of the orifice size in the theory³⁹ utilized to derive Equation 4 and 5. Thus, $v = \frac{a^2 \epsilon_0 E^2}{3\eta L}$ where v is the average velocity, and L is a characteristic distance over which the pressure varies (e.g., the cone-jet length). Using the electric pressure and the deviation in this pressure with x from the simulation results, and multiplying the velocity by the cross-sectional area results in:

$$Q = 2\pi\epsilon_0 E \frac{a^4 dE}{3\eta dx} \quad (6),$$

where the electric field and derivative are taken from the simulation at the x - and y -extensions.

The effective radius a is the only unknown and it must lie between the jet and cone radii.

The experimental Q data was well fit by utilizing $a = 0.4$ to $0.8 \times$ the experimentally determined cone radius. Figure 2.8 summarizes the results for experimental and predicted Q with a value of $a = 0.75r_{cone}$ for all cases except the neat DNDA data, which requires $a = 0.4r_{cone}$. Thus for most cases, roughly 75% of the cone width is moving fluid with the outer 25% serving as an orifice for the mobile fluid. For DNDA (and to a lesser extent DNDA + 0.1 wt% FA38) which has both

low viscosity and low conductivity, the mobile portion of the cone is smaller. Previous workers^{39, 40} have defined the ratio of the residence time of fluid in the cone-jet transition region to the charge relaxation time, $\varepsilon\varepsilon_0/K$ where ε is the dielectric constant (ca. 3 for a polymer melt). This ratio $\frac{\pi\eta^{1/2}}{K^{1/2}\varepsilon\varepsilon_0E}$ relates to the number of electric relaxation cycles (i.e., the time needed for charge to re-arrange) that occur while the fluid moves through the jet. Low ratio values (which occur for DNDA neat and DNDA + 0.1 wt% FA38) were associated with a quantities that were a smaller fraction of the cone radius. This is consistent with fast flow (low viscosity) and slower charge transfer due to low conductivity.

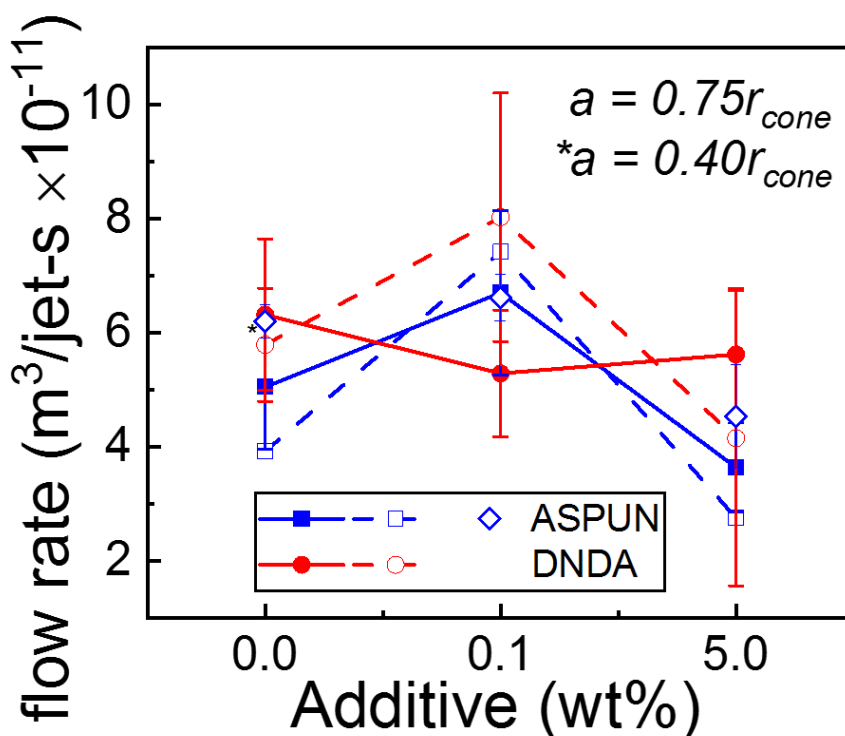


Figure 2.8. Comparison of experimental data (filled symbols) and theoretically calculated (open symbols) flow rate from Equation 6 as a function of FA38 loading wt% for ASPUN (blue squares) and DNDA (red circles), respectively. Letting $a = 0.75r_{cone}$ ($a = 0.40r_{cone}$) gives the open (starred open) symbol theoretical fit. For ASPUN, the order of magnitude theory, $Q \propto \pi a^2 \frac{\gamma}{\eta}$ is also plotted (open blue diamonds).

The observed flow rate is almost constant as the conductivity and viscosity are changed. Combining the most basic form for $Q = \frac{\pi a^4 \varepsilon_0 E^2}{3\eta L}$ with Equation 6 or examining the experimental data indicates that related quantities L and ℓ_{jet} are proportional to a , which is itself a fraction of r_{cone} . Thus both a and L are likely set by capillary lengths (see Section 2.2.3.1) with the only difference being the particular electric field value used in Equation 3. Considering a and L proportional and substituting the capillary length from Equation 2 results in $v \propto \gamma/\eta$ (which also appears in the discussion at the end of Section 2.2.3.1) and $Q \propto \pi a^2 \frac{\gamma}{\eta}$. This approach results in a reasonable fit, as shown in Figure 2.8 for ASPUN ($a = 0.75r_{cone}$, open blue diamonds) Note that this expression has no explicit dependence on E . Considering the dependence of a on viscosity, this simplified form helps explain why Q is relatively constant despite changes in conductivity and viscosity, as discussed further in Section 2.2.3.3.

It is useful to re-visit Equation 4 and 5, which contain both Q and E , and substitute Equation 6 which also relates these two quantities. This results in

$$r_{jet} = r_{cross} \sim \frac{\varepsilon_0^{1/2} a E^{1/2}}{K^{1/4} \eta^{1/4}} \quad \text{and} \quad \ell_{jet} = x_{cross} \sim a \quad (7),$$

where the dimensional approximation that $\frac{dE}{dx} \sim \frac{E}{a}$ and the assumption that E at the crossover point (the E in Equation 4 and 5) is some fraction of E at the plate edge (which is the E quantity in Equation 6) have been used. These results are discussed in detail in the following section.

2.2.3.3. The uniquely useful role of conductivity in setting the jet radius

Examining Equation 4, the parameter with the largest influence on the jet radius is the flow rate. Q is dependent on the cross-section area (a^2) and the velocity, which increases with the driving force (proportional to E) and decreases with the viscosity. However, as discussed above, the experimental values for the flow rate (with similar E field values, Figure 2.8) reveal that 5 of the

6 conditions explored in this work have the same flow rate to within error, even though the two formulations of polyethylene have viscosities that differ by a factor of 4. To better understand this observation, we can examine the interplay between a and viscosity. In particular, a has a hidden dependence on viscosity, as it is proportional to the cone radius which is set by the capillary length, which experimentally increases with viscosity ($a \sim \eta^{0.3-0.5}$). Considering the order of magnitude estimate $Q \sim a^2\gamma/\eta$ (i.e., the cross-sectional area times the characteristic velocity) or the more detailed form in Equation 6, where the electric field also has a hidden dependence on η (i.e., as viscosity decreases, the capillary length decreases, and thus E increases), and substituting for a , reveals that the flow rate is almost viscosity independent, as observed experimentally. Examining the jet radius form in Equation 7, shows the same effect: the quantity $a/\eta^{0.25}$ is almost constant with viscosity, and thus the jet radius is relatively independent of viscosity. Therefore, if one is seeking to decrease the jet radius by reducing the flow rate, then the viscosity is not a useful parameter in an unconfined system. Experimental results summarized in Supporting Information Figure A-2.1 confirm that viscosity has no predictive effect on jet size. DNDA melts with viscosity values in the range of 60 – 70 Pa-s and ASPUN melts with η ranging from 250 – 300 Pa-s display almost identical r_{jet} values of 20 – 60 μm and 20 – 50 μm , respectively. For the neat cases where the conductivity is almost identical, but the viscosity varies by 4 \times , the DNDA and ASPUN jet radii vary by < 15%.

Decreasing E may decrease the flow rate and thus also r_{jet} , which is desirable for nanofiber formation. However, sufficient decrease in E will lead to the pattern of cone-jets collapsing and extinguish the electrospinning process; thus this is not a productive approach.

Such analysis makes the unique utility of the conductivity clearer. Increasing K will decrease the jet radius directly. Examining Equation 7, it has no other significant counterbalancing effects:

increased K will also decrease a but this is only a weak dependence, which mitigates a potential increase in E as result of the fluid pulling closer to the plate edge. Experimental data bears out this analysis. Figure S1b shows r_{jet} as a function of measured conductivity: the downward trend with conductivity raised to the power -0.25 (as in Equation 7) is evident. Tuning K to alter r_{jet} is also fundamentally more experimentally achievable than the alternative of decreasing E or increasing η to decrease the flow rate, particularly with the facile repurposing of pre-existing additives. Characteristic images of the cone-jet regions near the plate edge are shown for each three experimental cases for ASPUN (Figure 2.7b) and DNDA (Figure 2.7c) with progressively higher additive wt%. It is clear that upon increasing conductivity all features are smaller including the jet radius.

2.2.3.4. Fiber diameter

The same simulation and theory approach^{39, 40} for viscous melts that results in Equation 4 and 5, provides a form for the radius as a function of x , sufficiently far from the plate edge. This should at a minimum be applicable for $x > x_{cross}$ (i.e., past the crossover point), which is the region in which the jet transforms into the final fiber.

$$r(x) \sim \left(1 + \sqrt{1 + \frac{24 IE\eta}{\pi \gamma^2}}\right) \frac{\gamma Q}{2IEx} \approx \left(1 + \sqrt{1 + \frac{24 \varepsilon_0^{\frac{1}{3}} \eta^{\frac{7}{6}} K^{\frac{1}{2}} Q^{\frac{2}{3}} E^{\frac{5}{3}}}{\pi \gamma^2}}\right) \frac{\gamma Q^{\frac{1}{3}}}{2\varepsilon_0^{\frac{1}{3}} \eta^{\frac{1}{6}} K^{\frac{1}{2}} E^{\frac{5}{3}} x} \sim \frac{\eta^{\frac{5}{12}} Q^{\frac{2}{3}}}{\varepsilon_0^{\frac{1}{6}} K^{\frac{1}{4}} E^{\frac{5}{6}} x} \sim \frac{\varepsilon_0^{1/2} E^{1/2} a^2}{\eta^{1/4} K^{1/4} x} \quad (8),$$

where the total current I was estimated from the surface current at the cross-over point, as in the original work. The surface charge density at the cross-over point (involved in the derivation of Equation 4 and 5) $\sigma \sim \varepsilon_0^{1/2} E^{1/2} \eta^{1/4} K^{1/4}$, results in $I \sim \varepsilon_0^{1/3} \eta^{1/6} K^{1/2} Q^{2/3} E^{2/3}$. This derivation assumes a constant electric field and thus the presence of a co-factor is expected, which again is approximately 3 for the experimental conditions in this work with E in Equation 8 set to the value at the cross-over point. Note that the co-factor for $r(x)$ and that for x_{cross} cancel resulting in an

unchanged expression for r_{cross} (i.e., Equation 4). Substituting the expression for Q (i.e., Equation 6), results in the final term.

Equation 8 indicates that the fiber radius should decrease roughly as $\frac{1}{x}$, where x is the distance from the source plate. This prediction can be compared to experimental results in several ways. Figure 2.9a shows a characteristic jet profile of r versus x taken from analysis of optical images. Such data is quantitatively reliable relatively close to the plate edge; further out, loss of focus or movement of the fiber during the shutter time results in feature broadening. Experimental data from all six cases was generally consistent with the $\frac{1}{x}$ form and could be fit using the penultimate term in Equation 8, with the only adjustable term being the co-factor which was in the range of 2 – 3. As shown in the figure, near the plate edge, the cone-jet is dominated by the cone. After this region, the jet theoretical prediction could be matched to the experiment through the cross-over point before loss of focus and jet motion affected the experimental data. For the theoretical fit in Figure 9a, the average experimental fiber radius of 13 μm would be expected to occur at $x = 11$ mm, which is reasonable, given visual observations of the experiment.

To further experimentally test the $r(x)$ model, informal velocimetry was utilized where imperfections (e.g., air bubbles) in the melt were identified in video data and tracked to estimate the average speed of the fluid flow. (For additional details, see the Experimental Methods section.) Because flow rate is a constant (i.e., there is no mass loss) as the fiber thins, the fluid velocity increases. Measured average velocities for each experimental case were compared with the theoretical average velocity, found by assuming a $\frac{1}{x}$ decrease in radius from the jet to the fiber, as shown in Figure 2.9b. The agreement is good for the lower conductivity cases where speeds are relatively low and solidification (i.e., formation of the solid fiber due to cooling) occurs relatively close to the source plate (within 1 – 2 cm of the total working distance of 10 cm). For lower

viscosity, higher conductivity cases, the velocity estimates are the same order of magnitude. In these cases, visual observations indicate that the fibers are at least semi-liquid upon arrival at the collector; however, the theoretical expression predicts hardening at the final fiber diameter much earlier (by ca. $x = 3$ cm). Thus experimentally the fiber is not thinning as rapidly as expected ($\frac{1}{x}$) in the region far from the source plate, which is likely due to increased viscosity from cooling and/or decreased electric field (both of which affect the co-factor of $\frac{1}{x}$ in Equation 8), as discussed further in Section 2.2.4.

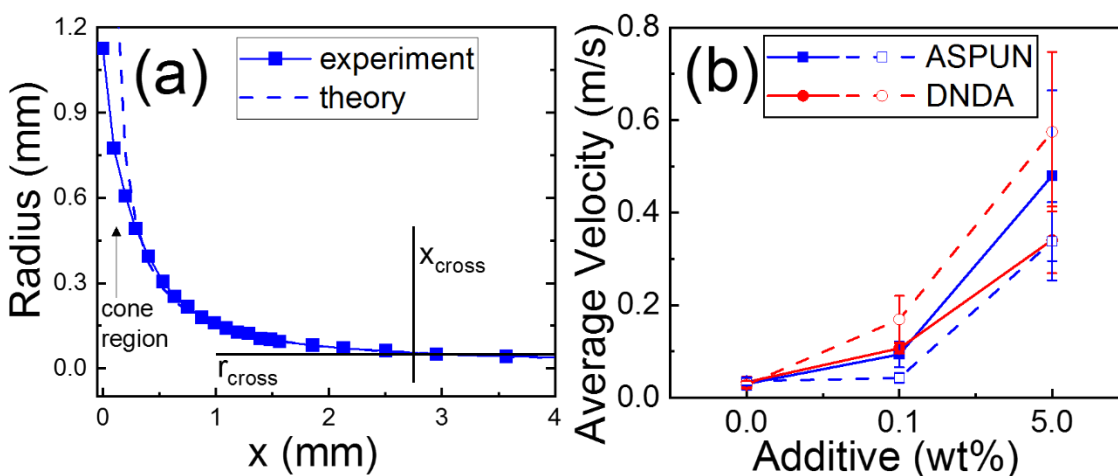


Figure 2.9. a) A characteristic experimental jet radius (blue squares, blue line) compared with theoretical predictions (blue dashed line) from Equation 8 for ASPUN. Near the plate edge, the cone-jet is dominated by the cone formula as expected. The $\frac{1}{x}$ form for the jet is consistent with the data out to and beyond the cross-over point, here marked by the average x_{cross} (2.75 mm) and r_{jet} ($r_{cross} = 50 \mu\text{m}$). After ca. 4 mm, motion of the forming fiber and loss of focus make the experimental data unreliable. The theoretical curves is about 75% of that predicted by Equation 8 (with a co-factor of 3) for this condition, within the expected error, and reaches the predicted fiber size (i.e., $13 \mu\text{m}$) at 11 mm. b) Measured average velocities for each experimental case (filled symbols, solid lines) for ASPUN (blue data) and DNDA (red data) were compared with the theoretical equivalent case (open symbols, dashed lines).

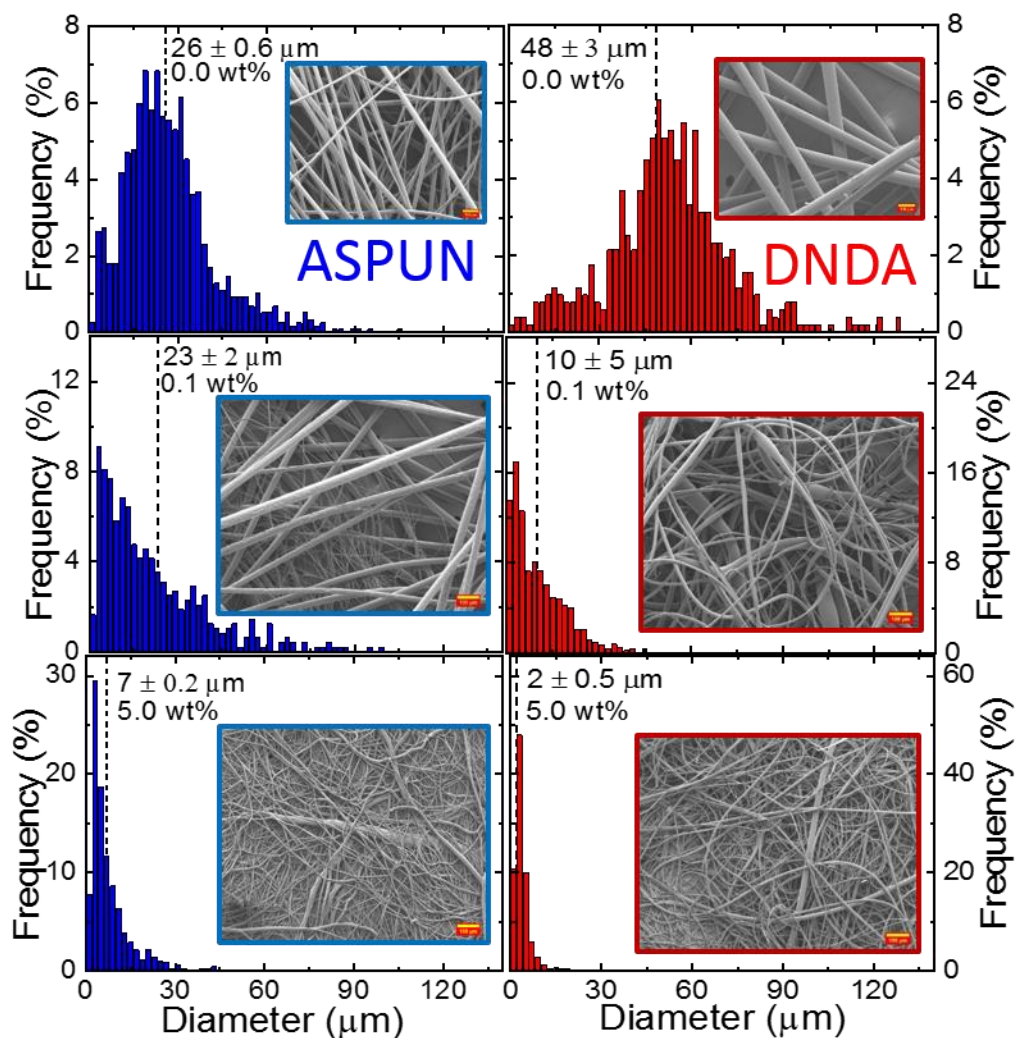


Figure 2.10. Histogram graphs of melt electrospun fiber diameters for ASPUN (blue data, left column) and DNDA (red data, right column) as a consequence of increased additive loading wt% (top to lower row). In each graph, the inset is an SEM image of the fibers; scale bars in each graph represent 200 μm.

Characteristic scanning electron microscopy images of the resultant electrospun fibers are presented in Figure 2.10, along with histograms of the fiber diameter and the resultant average size. For DNDA (Figure 2.10, right column), increasing conductivity (top to bottom rows) resulted in a decrease in fiber diameter by 20× (i.e., from $48 \pm 3 \mu\text{m}$ to $2 \pm 0.5 \mu\text{m}$). For the as-received DNDA (Figure 10, right column, top row), melt electrospun fibers removed from the collector

were thread-like with little observable fiber-fiber bonding, consistent with the relatively large fiber size and complete solidification before reaching the collector. After increased ionic conductivity via inclusion of the FA38 additive, the resultant fibers were visually cotton-like, with an average fiber diameter of $\sim 2 \mu\text{m}$. For higher viscosity ASPUN, the decrease in fiber diameter was $\sim 4\times$. These differences are discussed in the next section. Supporting Information Figure A-2.2 shows an expanded view of the lower histogram panels of Figure 10 for easier viewing. Increasing the melt conductivity results in a significant increase in fraction of fibers produced with sub-micron diameters: for example, for DNDA + 5 wt% FA38 20% of the fibers created were nanofibers, as compared with 0% for the neat DNDA.

2.2.4. The path from jet to fiber

As argued above, the jet radius, which sets the upper limit on fiber size, is a key parameter to understand and control when seeking to produce smaller fibers. As discussed in detail in Section 2.2.3.3, analysis and preliminary data show that ionic conductivity of the melt can be used in a practical sense to reduce jet size and the viscosity, perhaps surprisingly, is not an important parameter.

As discussed in Section 2.2.3.4, after the jet is established, the theoretical prediction indicates that jet/fiber diameter will continuously decrease while it remains pliable. To illustrate, the role of fluid parameters, we here discuss a few cases in detail. Summarized in Figure 2.9a, as-received ASPUN has an average radius $50 \mu\text{m}$ jet at $x = 2.75 \text{ mm}$ which produces a $4\times$ smaller fiber diameter ($13.5 \mu\text{m}$), which if the $\frac{1}{x}$ form holds, occurs at $x = 11 \text{ mm}$. Using Equation 8 (with a co-factor of 3) to theoretically predict the radius, velocity, and thus fluid transition time from $x = 1 \text{ mm}$ to the collector (with $r = r_{fiber}$ at and beyond $x = 11 \text{ mm}$), results in a predicted transition time of 2.8

s, which matches well with the experimental value of 3.3 ± 1.4 s. This analysis indicates that the fiber was pliable for about 2 s (the time taken to reach $x = 11$ mm). The results and analysis for neat DNDA match similarly.

For ASPUN with 5.0 wt% FA38 loading, the cross-over jet radius is $20 \mu\text{m}$, occurring at $x = 2.1$ mm with a fiber diameter of $3.4 \mu\text{m}$ reached at 14.5 mm, and a transition time prediction of 0.29 s compared well with the experimental estimate of 0.21 ± 0.1 s. The flow rate for this case is about two-thirds that of the as-received ASPUN but the velocities are higher because the fiber/jet is smaller. The "draw ratio" $\frac{r_{fiber}}{r_{jet}}$ for ASPUN with 5.0 wt% FA38 is again ~ 4 , with the fiber staying pliable for ca. 0.2 s. We expect that the time to cool and solidify will be smaller for finer fibers due to the increase in fiber surface area.

Lower viscosity melts (DNDA) with larger draw ratios, and longer time to solidification reveal limitations of the $\frac{1}{x}$ prediction. Although transition time estimates match to within error and the model shows larger distances before solidification (22 and 42 mm for 0.1 and 5.0 wt% FA38, respectively) as expected, the theory transition times are consistently lower than experiment, which indicates that thinning is slower than the theoretical limit. Experimentally, for the 5.0 wt% loading case, fibers appear to still be fluid when arriving at the collector which is $x = 10$ cm. Given the jet radius of $20 \mu\text{m}$ occurring at 1.3 mm, if the theory held, a fiber radius of ~ 200 nm is predicted, as opposed to the actual observed value of $1.2 \mu\text{m}$. As expected, this discrepancy indicates that the thinning process is slower and more complex in the spatial region far from the plate edge. The maximum draw ratio (around 17) is achieved for this DNDA + 5.0 wt% FA38 loading case, which has similar jet diameter and transition time as ASPUN + 5.0 wt% but remains liquid for significantly longer, which may be reflective of its lower viscosity.

Thus while the jet size, which can be controlled by conductivity, sets the upper limit on the fiber size, dynamics within the elongation region (after x_{cross}) influence the final fiber radius. These include the temperature in that region, the fiber size (due to increased heat loss) and viscosity. While viscosity does not have a dominant effect on the jet size, it has more influence on the transition from jet to fiber. For instance, the highest conductivity ASPUN formulation is more than 2× the conductivity the equivalent DNDA case and forms a similar jet diameter but results in fibers 4× larger. This effect is likely due to the larger melt viscosity.

2.2.5. The role of the additive in increasing melt conductivity

Most neat ionic compounds are unlikely to be compatible with hydrophilic thermoplastic polymers. Thus, use of ion-containing additives, intended for other purposes but designed to incorporate into particular polymeric systems, was an important component of achieving this work. A conductivity increase of 20-50× was achieved by incorporating the FA38 additive, which also resulted in a slight (<20%) decrease in melt viscosity. Conductivity reflects both the volume density of ionic charge and the ionic mobility, which can be impacted by viscosity. Estimating the maximum interaction between mobility and viscosity as an inverse linear relationship⁴¹⁻⁴⁴ indicates that the conductivity increase due to viscosity change should be proportionally small. Note that while the viscosity of the two formulations varies by 4×, their conductivities are almost identical for as-received and 0.1 wt% cases, and the highest conductivity is observed in the high viscosity LLDPE polymer (ASPUN) at 5.0 wt% additive loading. Thus, the dominant effect of additive doping appears to be relatively straightforward, that is, an increase in the number of mobile ions per volume.

2.2.6. Advantages of the open plate configuration

The high viscosity of polymer melts creates many practical challenges for electrospinning, including nozzle clogging and the need for high pressure pumping, when using "confined" or needle-based systems.²²⁻²⁷ The unconfined configuration utilized here prevents these problems but also has tangible benefits for fundamental studies because the fluid location and dynamics reveal order of magnitude information about fluid properties and the fluid-field interaction. We briefly discuss some examples below:

1) As discussed at the end of Section 2.2.3.1, the time to first perturbation is most strongly influenced by viscosity (in a system where the polymer is unchanging and thus γ is constant) with time $\approx \eta h/\gamma$. To demonstrate this empirically, for the four cases where the conductivity is relatively constant (as-received and with 0.1 wt% FA38), the time to first perturbation can be well predicted by an empirical form of either $(0.43 \pm 0.05)*\eta$ or $(0.10 + 0.02)*\eta^{1.3}$. In the first case, the relatively weak dependence of h (the y -extension) on viscosity ($\eta^{0.3}$) is neglected; in the second, it has been included explicitly. The y -extension also has a weak dependence on conductivity ($h \sim K^{-0.2}$). Fitting the higher conductivity data (5.0 wt% FA38) with the first form results in a co-factor of 0.2 – 0.3, which is consistent with this K dependence: using the power of -0.2, a 20 – 50 \times increase in conductivity should result in a decrease in the co-efficient by a factor of ~ 2 , which is consistent with these numbers (0.43 goes to 0.22). This means that the time to the first perturbation can be utilized as a measure of viscosity.

2) The location of the fluid edge relative to the plate (i.e., the x - and y - extension) is meniscus like, increases with viscosity (to the 0.3 power), and decreases weakly with conductivity (to the -0.2 power, see Section 2.2.3.1). Cone width has the same basic dependence on viscosity and conductivity, although it is correlated with the electric field at a different location (the apex of the

cone), and thus is systematically larger (due to the lower field). As in most electrospinning configurations, a sharp feature (here, the plate edge) is utilized to maximize the electric field, which results in an inhomogeneous field with position; thus minute changes in the x - and y -extensions result in a change in the electric field and thus the jet-to-jet spacing $\lambda = \left(\frac{3\pi}{\epsilon_0}\right)\frac{\gamma}{E^2}$. Both the x - and y - extensions and the jet-to-jet spacing are related directly to the capillary length $\gamma/(\epsilon_0 E^2)$, however while the extension length scale is small ($\sim 400 \mu\text{m}$) and difficult to image (best viewed from the side of the plate), the jet-to-jet spacing has a co-factor of ~ 12 , making it an order of magnitude larger, is repeated multiple times along the plate edge, and is easily viewed from above. Thus, increased jet density is an indication that the capillary length has decreased due to decreased viscosity, increased conductivity, or both, and thus the fluid now resides in a larger electric field. As an example of obtaining information about viscosity and conductivity directly from visual observations, consider images of the early electrospinning process for DNDA with 0.0, 0.1, and 5.0 wt% FA38 loading in Figure 2.11. The time to the first perturbation is similar in all cases (occurring between the third and fourth images), indicating that the viscosity is similar (which it is, varying by less than 20%). Compare these results to Figure 1 where the viscosity varies by $4\times$ and time increments in parts a) and b) also vary by $4\times$. The slight dependence of the time to first perturbation on conductivity is not easily quantified, even though the conductivity varies by $20\times$ from as-received to 5.0 wt%.

However, looking at the last image in each sequence, it is clear that the jet density increases and the cone width decreases as the weight percent of additive increases. Having already established that the viscosity is relatively constant by observing the time to first perturbation, these changes can be attributed to an increase in conductivity. The average jet-to-jet spacing decreased by $\sim 2\times$

from 0.0 to 5.0 wt% FA38, which indicates that the capillary length also halved. This result is consistent with the known increase in conductivity by a factor of 20 ($20^{-0.2} = 0.55$).

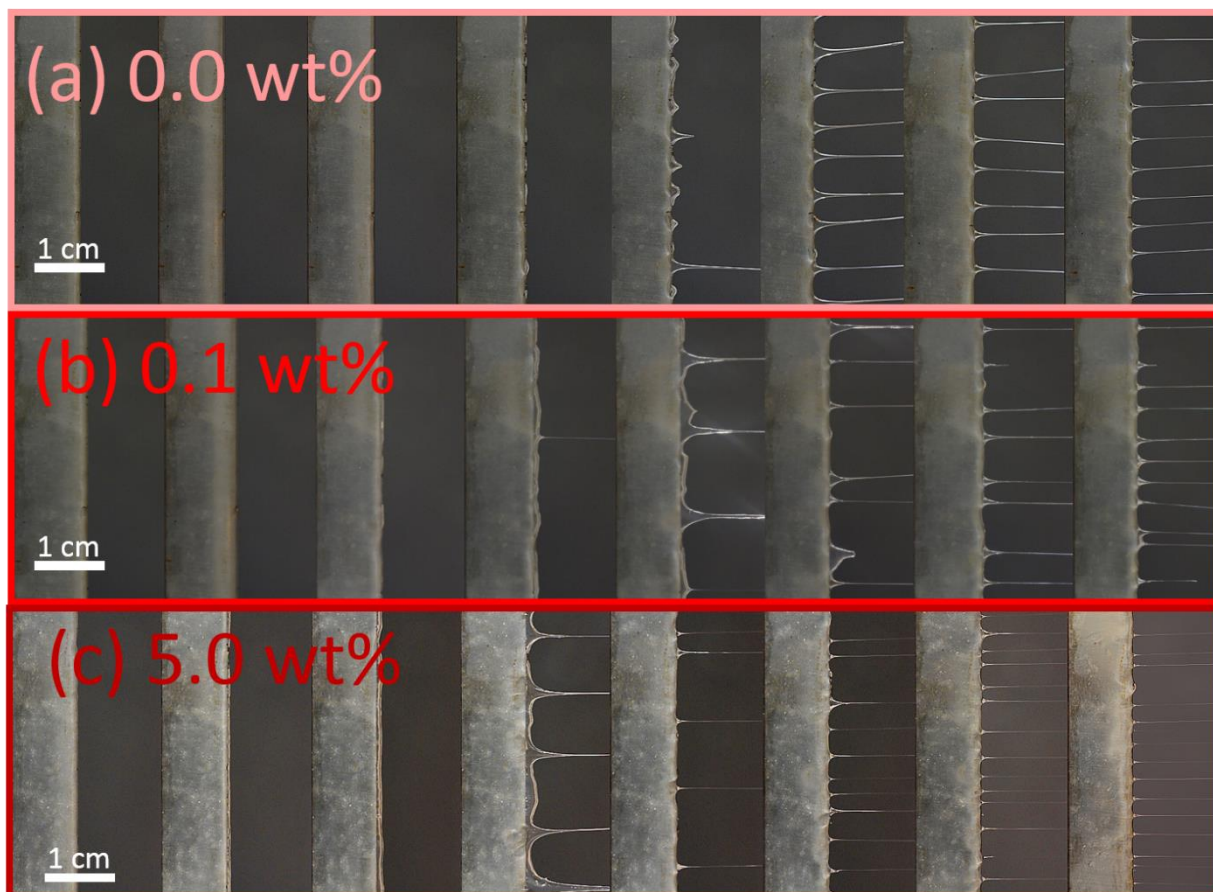


Figure 2.11. Photographic images of the spinning plate edge (top down view) captured every 15 seconds for 8 consecutive images (left to right) showing the evolution of protrusions and jets formation for samples composed of (a) as-received DNDA and those with the addition of (b) 0.1 wt%, and (c) 5.0 wt% loading FA38. The scale bar represents 1 cm in each image.

2.3. Conclusion

The conductivity of polyethylene melts was increased by up to 50× via incorporation of a commercial anti-static agent which provided additional ions to facilitate smaller characteristic size scales, including the meniscus size, cone width and jet width. The process by which a thin fluid film spontaneously forms an array of cone-jets in unconfined melt electrospinning was reviewed and the characteristic time to first perturbation described and connected to the fluid viscosity. In

this process, the fluid extends beyond the plate towards the collector and this characteristic length scale (the x - or y - extension) is determined by the fluid viscosity and conductivity and connected to the capillary length. For lower viscosity or high conductivity, the extension length is smaller (e.g., the fluid end is closer to the plate edge); due to the inhomogeneous electric field created by the sharp plate edge, the electric field at this location is larger, leading to increased jet density. Cone size is also a capillary length and proportional to the observed extension lengths. An extensive discussion of the factors that determine the jet radius and an argument that increasing the conductivity is the most facile means to decrease characteristic jet size are presented. Jet size is a particularly important parameter because the fiber begins forming at the jet; thus smaller characteristic jet sizes should enable thinner fibers. A decreased flow rate will also decrease the jet radius, but in an unconfined electrospinning geometry, such as utilized here and likely necessary for melt electrospinning due to high fluid viscosities, the flow rate is almost completely determined by the electric field and can be difficult to easily tune. In fact, in sampling a parameter space that included changing the viscosity by $4\times$ and the conductivity by $50\times$, the measured flow was constant to within a factor of 2. In addition, because the electric field is crucial to forming and maintaining the cone-jets, and thus enabling electrospinning, decreasing the electric field with the goal of decreasing flow rate will ultimately result in collapse of the cone-jet. The transition from jet to fiber is influenced by the distance the fluid travels after the jet and before the fiber solidifies. Thus, a second effect of narrower jets is higher fluid velocities at the jet, thus an ability to potentially travel further during the time before solidification and resultant formation of thinner fibers.

2.4. Experimental Methods

2.4.1. Materials and characterization

Two grades of linear low-density polyethylene (LLDPE) were utilized: ASPUN 6850A (ASPUN) and DNDA 1082 NT 7 (DNDA) (Dow Chemical) with a melt temperature (T_m) and melt flow index (MFI) of 131 °C, 30 g/10 min. and 125 °C, 160 g/10 min., respectively. LLDPE pellets were cryo-ground (SPEX CertiPrep 6750 freezer-mill) to obtain a powder. Dynamic scanning calorimetry (DSC) (Perkin Elmer Diamond DSC-7, 25 °C to 450 °C at 20 °C min.⁻¹) confirmed melting points in the range 131 – 135 °C and 125 – 129 °C, with no substantial change observed after cryo-grinding or heating at 200 °C for 60 minutes. The anti-static agent Hostastat FA38 (FA38) (Clariant) was utilized as a dilute ionic supplement. Additive and polymer powder were physically mixed and stirred for approximately 5 minutes prior to use to achieve homogeneity.

2.4.2. Apparatus

The melt electrospinning apparatus (Figure 2.12) consists of a machined aluminum source plate (base dimensions 16.25 × 5 × 2.5 cm) with a replaceable tungsten carbide-tipped blade (Magnate PK0618T 15 × 2.5 × 0.3 cm) attached flush to the plate surface with countersunk screws to provide a consistent, sharp plate edge. The thin edge has a radius of curvature of ~21 μm as measured in a confocal laser scanning microscope (Keyence VKx1100). (See appendix 2 Figure A-2.3 for a detailed drawing.) The source plate rests on a commercial hot plate (Fisher Scientific Type 1900) with the blade edge protruding by 0.4 cm. Before and after the electrospinning process, a type-K thermocouple (Omega) was inserted into the melt film to measure the temperature. The source plate is electrically-grounded using a copper metal rod attached to a thick aluminum braid. The aluminum collector (20 × 30 cm, covered with removable aluminum foil) is located 10 cm from

the source plate and held at a negative electric potential by a high voltage source (Glassman High Voltage Model FC60R2). The collector, source plate, and hot plate reside in an enclosure with cement board sides, a 1/4" tempered glass (United Plate Glass) top, and a removable polycarbonate viewing window on the front side. During experiments, the box is situated inside a chemical fume hood.

To initiate each experiment, the source plate is temporarily removed and the hot plate is set to temperature in order to warm the box interior. 10 gram of polymer powder (as-received or with additive) is uniformly spread over the source plate. After ~ 30 minutes when the enclosure interior reaches a steady state temperature of ~55 °C, the front window is briefly opened and the loaded source plate positioned on the hotplate. Once the enclosure is resealed, the polymer and source plate attain the desired equilibrium set temperatures (polymer melt ~195 °C; plate ~202 °C) within approximately 30 minutes. After an additional 5 minutes quiescent stabilization time, a mechanical handle temporarily engages the thermocouple onto the polymer melt surface to measure the temperature about 1 cm back from the source plate edge. Subsequently, a negative-polarity high voltage is applied to the collector, thereby initiating the electrospinning process and starting the experiment. Electrospinning continues for 20 minutes without any observed substantial decrease in polymer melt thickness. The measured DNDA and ASPUN LLDPE fiber fabrication rates were ca. 5.5, 6.6, and 7.7 g/hr and 2.1, 2.4 and 3.5 g/hr, respectively for samples containing 0.0, 0.1 and 5.0 wt% FA38. Thus, the calculated mass loss ranged from 0.7 – 2.6 g.

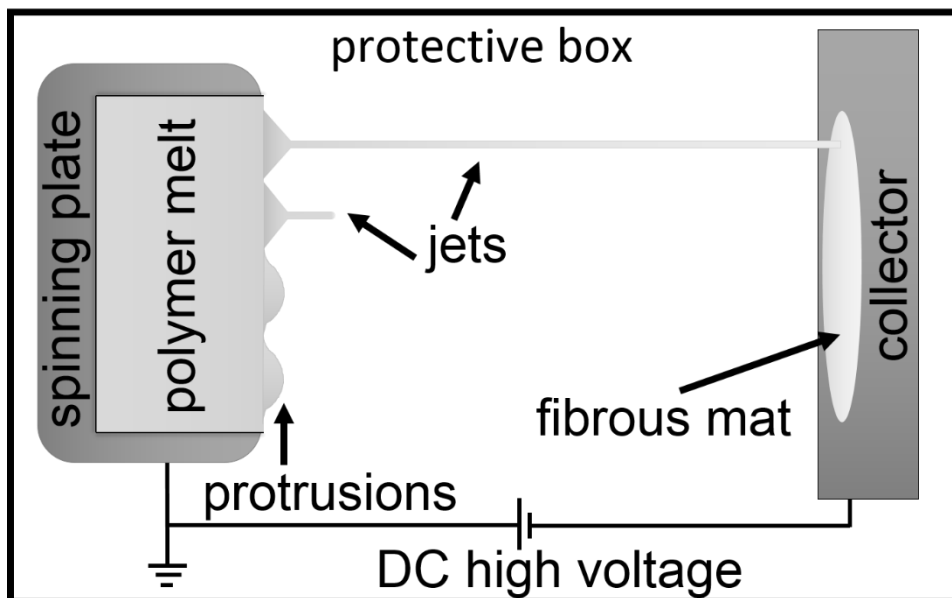


Figure 2.12. Schematic diagram (top-down view): after application of high voltage the polymer melt on the horizontal metal spinning plate spontaneously forms protrusions, leading to jet creation and subsequent fibrous mat deposition on the metal collector located 10 cm from the plate edge. Note: The spinning plate rests on top of a hot plate which is not shown in the image for enhanced clarity.

2.4.3. Characterizing the electrospinning process and fiber morphology

Neat ASPUN and DNDA LLDPE experiments were initially performed under a range of temperature (160 – 210 °C) and high voltage (-41, -43, -45, -47 kV applied to the collector) conditions to optimize operating parameters. Subsequent electrospinning experiments using polymer with additive (0.0, 0.1 and 5.0 wt% FA38) were performed under the optimized conditions with a high voltage of -45 kV and a polymer temperature of 190 – 200 °C. Both a camcorder and a high-resolution camera (Sony, Model HDR-CX240 and Sony, Model a7R IV with Canon EF 180mm f3.5L macro telephoto lens, respectively) separately observed the edge of the source plate (top and side views) to monitor the electrospinning process.

Data on size scales, number of jets versus time, fiber size, and the time to first perturbation is reported as an average with error the standard deviation of the average from four separate

experiments. Image analysis was conducted using post-processing software (Image-J) where jet number versus time was determined at one-minute intervals from single video frames. High resolution optical images were examined to measure the cone width and extension of the fluid film over the plate edge (x - and y -extension, see Section 2.2.2), as well as to quantify the jet/fiber radius as a function of distance from the source plate. Motion of the jets/fibers during the exposure time prevented clear visualization of the jets/fibers at distances further than 3 – 5 mm from the plate edge. Velocity estimates and measured diameters of the resultant fibers were utilized to extrapolate fluid behavior beyond this region. Fiber samples (retrieved from left, center and right regions of the collector) were obtained by fitting aluminum stubs with adhesive tabs into a wooden holder with equidistant separations, and pressing the stubs to the mat; thus enabling reproducible sampling locations from different experimental runs. To produce a conductive surface and reduce charging effects, stub-mounted samples were coated with ~60 nm of gold/palladium alloy in a sputter coater (Quoron Technologies, S67620) at a rate of 7 nm/minutes. Subsequent fiber diameters, diameter distribution, and overall mat morphology were determined via scanning electron microscopy (SEM) imaging (Phenom FEI desktop SEM operating at 5 kV).

Average fluid velocity was estimated using an informal velocimetry approach. Jets which possessed a notable imperfection (e.g., such as a bubble or particle identified from video data) were monitored with screenshots to calculate the time for the observed distinctive feature to travel from the plate edge to the collector. For higher conductivity fluids, the video playback speed was reduced to ensure adequate time resolution. Multiple (i.e., typically 3 – 4) cases were identified for each experimental condition with the average velocity determined via dividing the distance by the observed time interval. Theoretical estimates of jet radius versus position were obtained by using the penultimate form in Equation 8 with the experimental values of flow rate, viscosity, and

conductivity, the simulated electric field at the cross-over point (see Section 2.2.3.2) and a co-factor of 3. These theoretical curves matched experimental r versus x (the coordinate connecting the source plate and collector) data relatively well. The distance between the source plate and collector was divided into slices starting at $x = 1$ mm, and proceeding with 2.5 mm increments until 1 cm, and 1 cm increments thereafter until reaching the collector at $x = 10$ cm. Utilizing the theoretical jet radius versus position data and the experimental flow rate, the velocity at the beginning and end of each slice was determined. The transition time for each slice was the length of the slice divided by the average of the initial and final velocities. The slice transition times were summed to find a total transition time and the average velocity was calculated, in direct analogy with the experimental value, by dividing the total distance by the total time.

2.4.4. Calculation of electric fields

The electric field pattern within the electrospinning apparatus was simulated by a commercial modelling program (ANSYS electromagnetic desktop 2020). A three-dimensional electrostatic finite element analysis was employed with adaptive meshing. The initial mesh was generated using the TAU method with moderate mesh resolution and curvilinear meshing enabled while spatial detail was enhanced in areas of interest by specifying mesh operations on those geometries. The source plate edge was assigned a surface approximation mesh operation limiting the accepted normal angular deviation to 15° . A volume enclosing the path connecting the center of the plate edge and the collector center was set to have a maximum mesh length of $10\ \mu\text{m}$. The tetrahedral mesh was refined each pass by adapting the 30% highest error tetrahedrons until a desired percent energy error was reached; subsequently, the optimized final mesh had 7×10^6 tetrahedrons and 0.27% error in energy. Figure 2.13 shows the result for an applied voltage of -45 kV. The coordinate system has an origin near the upper edge of one corner of the plate (see Figure S3).

The z direction is parallel to the plate edge, x is the direction along which spinning occurs, starting at the plate edge and continuing to the collector, and y is the direction opposite gravity that reflects the height of the fluid film on the plate edge.

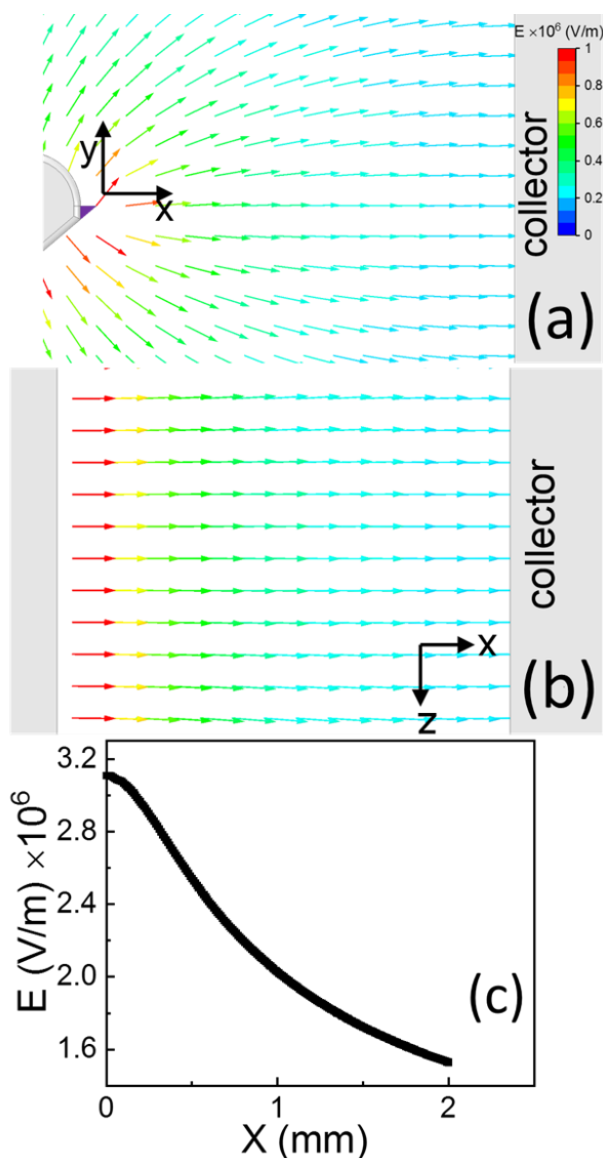


Figure 2.13. Electric field simulation results viewed from a) side, and b) top-down perspectives, respectively, with the field amplitude color scale given above. The purple triangle in a) indicates the blade edge where the polymer is placed. c) The magnitude of the electric field at the center of the plate and a location of $y = 380 \mu\text{m}$ (i.e., at the average location of the polymer surface where jets form) as a function of x , where the origin $x = 0 \mu\text{m}$ is located at the plate edge. The distance from plate edge to the collector is 10 cm.

2.4.5. Conductivity measurements

Conductivity measurements were performed (Hikoi IM3533-01 LCR meter) over the frequency range of 1 Hz – 200 kHz and temperature range of 120 – 200 °C on ASPUN and DNDA melts having three different concentrations of the antistatic additive (0, 0.1 and 5 wt%). Measured values were verified with an ultra-precision capacitance bridge (Andeen-Hagerling 2700a) in the overlapping frequency range 50 Hz – 20 kHz. Gold interdigitated electrodes (IDE) (Metrohm) with 125 digit pairs of 6750 μm length and a 10 μm gap residing on a rectangular glass substrate ($2.2 \times 7.6 \times 0.7$ cm in size) were ozonated for 30 minutes (Bioforce Nanosciences UV-Ozone Procleaner), followed by rinsing with isopropyl alcohol, and submersion for 12 hours in 1000:1 (toluene: dimethyl decyl chlorosilane) solution. The silane reacts with surface hydroxyl groups and replaces them with methyl and decyl groups, which results in a hydrophobic surface and reduces water contamination of the electrodes. After silanization, IDEs were rinsed with toluene, sonicated in methanol for 2 minutes, and stored in a closed container until use. Powder (polymer + additive) was placed on an individual IDE, heated on a hot plate to 140 °C, and then allowed to cool to form a polymeric film. Samples resided on a metal stage in a shielded probe station (Desert Cryogenics model #DC1472) for measurements under high-vacuum ($\sim 10^{-5}$ torr) or ambient conditions.

Complex impedance as a function of frequency (AC test signal 0.1 V_{rms}) was measured and the ionic conductivity determined by fitting the data to a model circuit (Figure 2.14). Nyquist plots were created (Zview version 3.2b software) for each temperature point using the full available frequency spectrum. RC models with a capacitor phasor element were used to fit Nyquist plot semicircles to obtain the bulk resistance values at zero frequency. Example data with fit are shown in Figure 2.14a. A single parallel RC circuit was used for fitting samples with low ionic

conductivities (i.e., with single semicircle in Nyquist plot Figure 2.14b) vs two parallel RC circuit in series for higher conductivities (i.e., with two semicircles in Nyquist plot Figure 14c). Final conductivity values, K (in S/cm), were calculated using $K = \frac{k}{R_B}$ where k is the cell constant of IDE (in cm^{-1}) and R_B is the bulk resistance.⁴⁵⁻⁴⁷ The IDE cell constant was confirmed by measuring a liquid conductivity standard (potassium chloride in water with conductivity of $5 \mu\text{S/cm}$, VWR) under ambient conditions. The measurement sensitivity limit is set by the background signal from the IDE, determined by measuring each IDE prior to use over the same frequency and temperature range (1 Hz – 200 kHz and 120 – 200 °C, respectively). The limit varies with temperature and is $\sim 1 \times 10^{-11}$ S/cm at T_m and $\sim 2 \times 10^{-10}$ S/cm at 190 °C. The conductivity at 195 °C (i.e., the average measured polymer melt temperature during electrospinning) used in calculations is a linear extrapolation of the experimental values at 190 and 200 °C.

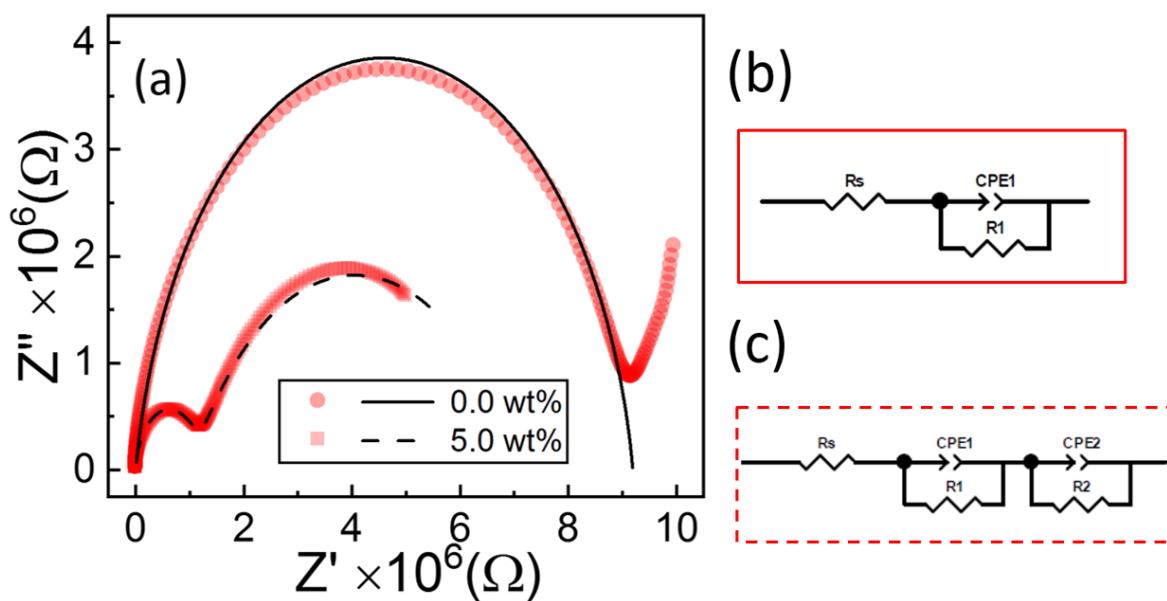


Figure 2.14. Experimental Nyquist plots (imaginary part versus real part of the complex impedance) for as-received DNDA (circles) and DNDA + 5.0 wt% FA38 (squares) at 200 °C. (b) A single RC circuit model was used to fit data from as-received and 0.1 wt% FA38 loading additive cases, and (c) a two parallel RC model circuit was used for data from 5.0 wt% additive melts, resulting in the fits shown as black lines (solid and dashed, respectively). Fitted R values from these curves were used to calculate the bulk resistance of the polymer melt sample.

2.4.6. Rheology measurements

Rheology measurements were performed on polymer and additive mixtures (parallel plate PP25 on an Anton Paar MCR-302 rheometer). Molten samples 25 mm in diameter and 1 mm thick were measured at temperatures from 120 – 200 °C. Amplitude sweeps were performed to determine the viscoelastic regime for each sample, working at the temperature extremes and using constant angular frequency with varying shear strain (0.01 – 100 %). Subsequent viscosity measurements were performed in this viscoelastic regime to minimize shear thinning for the given temperature range. Shear strain ranged between 0.1 – 5 % at a constant frequency of 1 Hz.

Conflicts of Interest

There are no conflicts of interest to declare.

Acknowledgements

This research was supported by the National Science Foundation (NSF) (grant CMMI-1635113). Some measurements were performed in the NC State Physics Education and Research Laboratory (EarL) as well also taken in part at the Analytical Instrumentation Facility (AIF) at North Carolina State University, which is supported by the State of North Carolina and the NSF (grant ECCS-154). The AIF is a member of the North Carolina Research Triangle Nanotechnology Network (RTNN), a site in the National Nanotechnology Coordinated Infrastructure (NNCI). The authors thank Ms. Birgit Anderson for DSC measurements, Mr. Hai Bui for precision machining of the spinning apparatus, and Prof. Russell Gorga for useful discussions. The authors also thank NC State libraries, the Department of Physics, and Dr. Ryan Boland for use of cameras, the Nonwovens Institute at NC State University for polymer material, Clariant for providing Hostastat FA38, and Prof. Keith Weninger and Prof. Karen Daniels for use of equipment.

2.5. References

- 1) Barnes, C. P.; Sell, S. A.; Boland, E. D.; Simpson, D. G.; Bowlin, G. L. Nanofiber technology: Designing the next generation of tissue engineering scaffolds. *Advanced Drug Delivery Reviews* 2007, 59, 1413-1433.
- 2) Cavaliere, S.; Subianto, S.; Savych, I.; Jones, D. J.; Roziere, J. Electrospinning: designed architectures for energy conversion and storage devices. *Energy Environ. Sci.* 2011, 4, 4761-4785.
- 3) Brown, T. D.; Daltona, P. D.; Hutmacher, D. W. Melt electrospinning today: An opportune time for an emerging polymer process. *Progress in Polymer Science* 2016, 56, 116-166.
- 4) Liang, D.; Hsiao, B. S.; Chu, B. Functional electrospun nanofibrous scaffolds for biomedical applications. *Advanced Drug Delivery Reviews* 2007, 59, 1392-1412.
- 5) Xue, J. J.; Wu, T.; Dai, Y. Q.; Xia, Y. N. Electrospinning and Electrospun Nanofibers: Methods, Materials, and Applications. *Chem. Rev.* 2019, 119, 5298-5415.
- 6) Lv, D.; Zhu, M. M.; Jiang, Z. C.; Jiang, S. H.; Zhang, Q. L.; Xiong, R. H.; Huang, C. B. Green Electrospun Nanofibers and Their Application in Air Filtration. *Macromol. Mater. Eng.* 2018, 303, 18.
- 7) Ma, X. Y. D.; Ang, J. M.; Zhang, Y. F.; Zeng, Z. H.; Zhao, C. Y.; Chen, F. G.; Ng, B. F.; Wan, M. P.; Wong, S. C.; Li, Z. B.; He, C. B.; Lu, X. H. Highly porous polymer nanofibrous aerogels cross-linked via spontaneous inter-fiber stereocomplexation and their potential for capturing ultrafine airborne particles. *Polymer* 2019, 179, 10.
- 8) Purwar, R.; Goutham, K. S.; Srivastava, C. M. Electrospun Sericin/PVA/Clay Nanofibrous Mats for Antimicrobial Air Filtration Mask. *Fiber. Polym.* 2016, 17, 1206-1216.

- 9) Asmatulu, R.; Khan, W. S. *Electrospun nanofibers for filtration applications*. Elsevier Science Bv: Amsterdam, 2019; p 135-152.
- 10) Zhang, S.; Rind, N. A.; Tang, N.; Liu, H.; Yin, X.; Yu, J.; Ding, B. *Electrospun Nanofibers For Air Filtration*. 2019; p 365-389.
- 11) Barhate, R. S.; Ramakrishna, S. *Nanofibrous filtering media: Filtration problems and solutions from tiny materials*. *J. Membr. Sci.* 2007, 296, 1-8.
- 12) dos Santos, D. M.; Correa, D. S.; Medeiros, E. S.; Oliveira, J. E.; Mattoso, L. H. C. *Advances in Functional Polymer Nanofibers: From Spinning Fabrication Techniques to Recent Biomedical Applications*. *ACS Appl. Mater. Interfaces* 2020, 12, 45673-45701.
- 13) Martins, A.; Araujo, J. V.; Reis, R. L.; Neves, N. M. *Electrospun nanostructured scaffolds for tissue engineering applications*. *Nanomedicine* 2007, 2, 929-942.
- 14) Martins, A.; Reis, R. L.; Neves, N. M. *Electrospinning: processing technique for tissue engineering scaffolding*. *International Materials Reviews* 2008, 53, 257-274.
- 15) McCullen, S. D.; Ramaswamy, S.; Clarke, L. I.; Gorga, R. E. *Nanofibrous composites for tissue engineering applications*. *Wiley Interdiscip. Rev.-Nanomed. Nanobiotechnol.* 2009, 1, 369-390.
- 16) Diani, J.; Liu, Y. P.; Gall, K. *Finite strain 3D thermoviscoelastic constitutive model for shape memory polymers*. *Polym. Eng. Sci.* 2006, 46, 486-492.
- 17) Greiner, A.; Wendorff, J. H. *Electrospinning: A fascinating method for the preparation of ultrathin fibres*. *Angewandte Chemie-International Edition* 2007, 46, 5670-5703.
- 18) Reneker, D. H.; Yarin, A. L.; Zussman, E.; Xu, H. *Electrospinning of nanofibers from polymer solutions and melts*. In *Advances in Applied Mechanics*, Vol 41, Aref, H.;

VanDerGiessen, E., Eds. Elsevier Academic Press Inc: San Diego, 2007; Vol. 41, pp 43-195.

- 19) Bhardwaj, N.; Kundu, S. C. Electrospinning: A fascinating fiber fabrication technique. *Biotechnology Advances* 2010, 28, 325-347.
- 20) Huang, Z. M.; Zhang, Y. Z.; Kotaki, M.; Ramakrishna, S. A review on polymer nanofibers by electrospinning and their applications in nanocomposites. *Compos. Sci. Technol.* 2003, 63, 2223-2253.
- 21) Web of Science. <http://apps.webofknowledge.com/>.
- 22) Wang, Q. Q.; Curtis, C. K.; Thoppey, N. M.; Bochinski, J. R.; Gorga, R. E.; Clarke, L. I. Unconfined, melt edge electrospinning from multiple, spontaneous, self-organized polymer jets. *Materials Research Express* 2014, 1.
- 23) Roman, M. P.; Thoppey, N. M.; Gorga, R. E.; Bochinski, J. R.; Clarke, L. I. Maximizing Spontaneous Jet Density and Nanofiber Quality in Unconfined Electrospinning: The Role of Interjet Interactions. *Macromolecules* 2013, 46, 7352-7362.
- 24) Thoppey, N. M.; Bochinski, J. R.; Clarke, L. I.; Gorga, R. E. Unconfined fluid electrospun into high quality nanofibers from a plate edge. *Polymer* 2010, 51, 4928-4936.
- 25) Thoppey, N. M.; Bochinski, J. R.; Clarke, L. I.; Gorga, R. E. Edge electrospinning for high throughput production of quality nanofibers. *Nanotechnology* 2011, 22, 345301.
- 26) Thoppey, N. M.; Gorga, R. E.; Bochinski, J. R.; Clarke, L. I. Effect of Solution Parameters on Spontaneous Jet Formation and Throughput in Edge Electrospinning from a Fluid-Filled Bowl. *Macromolecules* 2012, 45, 6527-6537.

- 27) Thoppey, N. M.; Gorga, R. E.; Clarke, L. I.; Bochinski, J. R. Control of the electric field-polymer solution interaction by utilizing ultra-conductive fluids. *Polymer* 2014, 55, 6390-6398.
- 28) Frenot, A.; Chronakis, I. S. Polymer nanofibers assembled by electrospinning. *Curr. Opin. Colloid Interface Sci.* 2003, 8, 64-75.
- 29) Hutmacher, D. W.; Dalton, P. D. Melt Electrospinning. *Chem.-Asian J.* 2011, 6, 44-56.
- 30) Hahladakis, J. N.; Velis, C. A.; Weber, R.; Iacovidou, E.; Purnell, P. An overview of chemical additives present in plastics: Migration, release, fate and environmental impact during their use, disposal and recycling. *J. Hazard. Mater.* 2018, 344, 179-199.
- 31) Natamai Subramanian, M. *Plastics additives and testing*. Wiley: Hoboken, New Jersey, 2013.
- 32) Ma, J.; Zhang, Q.; Mayo, A.; Ni, Z. H.; Yi, H.; Chen, Y. F.; Mu, R.; Bellan, L. M.; Li, D. Y. Thermal conductivity of electrospun polyethylene nanofibers. *Nanoscale* 2015, 7, 16899-16908.
- 33) Ma, J.; Zhang, Q.; Zhang, Y.; Zhou, L.; Yang, J. K.; Ni, Z. H. A rapid and simple method to draw polyethylene nanofibers with enhanced thermal conductivity. *Applied Physics Letters* 2016, 109, 5.
- 34) Rein, D. M.; Shavit-Hadar, L.; Khalfin, R. L.; Cohen, Y.; Shuster, K.; Zussman, E. Electrospinning of ultrahigh-molecular-weight polyethylene nanofibers. *Journal of Polymer Science Part B-Polymer Physics* 2007, 45, 766-773.
- 35) Givens, S. R.; Gardner, K. H.; Rabolt, J. F.; Chase, D. B. High-temperature electrospinning of polyethylene microfibers from solution. *Macromolecules* 2007, 40, 608-610.

- 36) Miloh, T.; Spivak, B.; Yarin, A. L. Needleless electrospinning: Electrically driven instability and multiple jetting from the free surface of a spherical liquid layer. *Journal of Applied Physics* 2009, 106, 114910.
- 37) de Gennes, P.-G.; Brochard-Wyart, F.; Quere, D. *Capillarity and Wetting Phenomena*. Springer: New York, 2010.
- 38) Potschke, P.; Pionteck, E.; Stutz, H. Surface tension, interfacial tension, and morphology in blends of thermoplastic polyurethanes and polyolefins. Part I. Surface tension of melts of TPU model substances and polyolefins. *Polymer* 2002, 43, 6965-6972.
- 39) Higuera, F. J. Stationary viscosity-dominated electrified capillary jets. *Journal of Fluid Mechanics* 2006, 558, 143-152.
- 40) Higuera, F. J. Numerical computation of the domain of operation of an electrospray of a very viscous liquid. *Journal of Fluid Mechanics* 2010, 648, 35-52.
- 41) Avramov, I. Relationship between diffusion, self-diffusion and viscosity. *Journal of Non-Crystalline Solids* 2009, 355, 745-747.
- 42) Seki, S.; Hayamizu, K.; Tsuzuki, S.; Takahashi, K.; Ishino, Y.; Kato, M.; Nozaki, E.; Watanabe, H.; Umebayashi, Y. Density, Viscosity, Ionic Conductivity, and Self-Diffusion Coefficient of Organic Liquid Electrolytes: Part I. Propylene Carbonate plus Li, Na, Mg and Ca Cation Salts. *J. Electrochem. Soc.* 2018, 165, A542-A546.
- 43) Yamaguchi, T.; Nakahara, E.; Koda, S. Quantitative Analysis of Conductivity and Viscosity of Ionic Liquids in Terms of Their Relaxation Times. *Journal of Physical Chemistry B* 2014, 118, 5752-5759.
- 44) Subbiah, B.; Morison, K. R. Electrical conductivity of viscous liquid foods. *J. Food Eng.* 2018, 237, 177-182.

- 45) Gómez, F.; Bernal, J.; Rosales, J.; Cordova, T. Modeling and Simulation of Equivalent Circuits in Description of Biological Systems - A Fractional Calculus Approach. *Journal of Electrical Bioimpedance* 2012, 3, 2-11.
- 46) Jacquelin, J. A Number of Models for CPA Impedances of Conductors and for Relaxation in Non-Debye Dielectrics. *Journal of Non-Crystalline Solids* 1991, 131, 1080-1083.
- 47) Qian, X. M.; Gu, N. Y.; Cheng, Z. L.; Yang, X. R.; Wang, E. K.; Dong, S. J. Methods to study the ionic conductivity of polymeric electrolytes using a.c. impedance spectroscopy. *J. Solid State Electrochem.* 2001, 6, 8-15.

CHAPTER 3

Modeling the effect of ionic conductivity on fiber diameter of melt electrospun fibers

Neelam Sheoran, Brent Boland, Jason R. Bochinski, and Laura I. Clarke**

N. Sheoran, B. Boland, Prof. J. R. Bochinski, and Prof. L. I. Clarke
Department of Physics, North Carolina State University, Raleigh, NC 27695-8202,
United States

Email: jason_bochinski@ncsu.edu and laura_clarke@ncsu.edu

3.1. Introduction

Nano- and meso-scale fibers are optimal for high efficiency filtration: high surface area to volume minimizes the interior fraction of each fiber, which does not filter but only takes up space and thus detrimentally affects properties like pressure drop and lifetime.¹⁻³ Fiber strength is also important for filtration applications. At larger length scales, high molecular weight commercial thermoplastics are often utilized due to their robust mechanical properties. These materials are generally insoluble and thus inaccessible to many nanofiber manufacturing techniques which are solution-based. One example is electrospinning, which can be utilized to facilitate produce nanofibers from solution.⁴ This technique can also be performed with melts; however, it is historically unpopular: the traditional electrospinning configuration (a needle, placed a high voltage, through which the fluid is pumped) is incompatible with high viscosity melts and viscosity is often informally cited as the primary cause of large resultant fibers (~10 μm). In this work, we conduct electrospinning with thermoplastic melts, utilizing an unconfined experimental scheme (a flat plate covered with polymer melt, described previously⁵) which resolves issues with needle clogging and pumping. Regarding fiber diameter, we note that the electrospinning process relies on ions within the fluid: thermoplastic melts have very low ionic conductivity. Manipulation of fiber size by altering conductivity for relatively low viscosity and high conductivity fluids (than melts) has previously been reported. In this work, we intentionally altered the ionic conductivity of thermoplastic melts over several orders of magnitude by using commercial additives. We report significant reduction in fiber size as conductivity increases; these results scale in a similar manner as solutions with 4 orders of magnitude lower viscosity and 8 orders of magnitude higher conductivity, indicating that ionic conductivity may be a limiting factor influencing fiber size.

3.2. Experimental methods

3.2.1. Material used

A variety of linear low density polyethylene formulations (using three different base polymers and four different additives) were utilized, with viscosities that ranged from ~60 to 300 Pa-s and conductivities between 10^{-9} and 10^{-4} S/m (Table 3.1). Some additives (Hostastat FE2Pdr and ATMER 129) were sufficiently volatile at 195 °C to result in decreased conductivity over the experiment time (10 -20 m); thus, the working temperature was dropped to 165 °C. T_m for ASPUN 6850 (DNDA 1082/1088) was 131 (125) °C. Calcium stearate was used as (i) an example compound with a known chemical formula and (ii) as a stabilizing agent (slightly increasing viscosity and additive evaporation). Polymer (Dow) was cryoground (SPEX 6750 freezer/mill) and additive powders (Clariant and Corda Technologies) were incorporated. Surface tension measurements (dataphysics OCA 25 goniometer was used for pertinent temperatures (165 °C and 195 °C) indicated a maximum change in surface tension of 25%. Goniometer uses lamella method and uses CCD and backlighting to get the polymer melt curvature which was fitted using laplace equation and final surface tension values were calculated (assuming no significant change in density due to additive or temperature variation).

3.2.2. Electrospinning Process

For all pure LLDPE cases (ASPUN 6850a, DNDA 1082, DNDA 1088), various temperature and voltage ranges were utilized to optimize (smooth spinning and finest fiber morphology) the operating values. A polymer melt temperature of 195 °C and a high voltage of -45 kV was used for samples (1-6) as listed in table 1. However, for the next set of samples (7-13), a lower polymer melt temperature of 165 °C and the same voltage of -45 kV were used due to some additives' volatile nature (which evaporate at higher temperatures). For comparison between the

two cases, DNDA 1088 and DNDA 1088 + 5wt % FA38 were electrospun at each temperature. To maintain the ambient temperature ($\sim 55\text{ }^{\circ}\text{C}$) and relative humidity (23%), the box was preheated, and a Reptile Humidifier controlled by an Inkbird IHC 200 Humidity Controller was turned on. Once the steady state of temperature and humidity was reached (in ~ 30 mins), 10 grams of polymer powder (as received or with additive) was uniformly spread over the source plate sitting outside the enclosure. The front window of the enclosure was briefly opened, and the loaded source plate was positioned on the hotplate. After closing the box, samples 1-6 were heated for 30 mins (samples 7-13 were heated for ~ 15 mins) till the processing temperature of $195\text{ }^{\circ}\text{C}$ ($165\text{ }^{\circ}\text{C}$) was reached. A k type thermocouple was inserted (from outside the box using a mechanical handle so that box remains sealed) into the polymer melt to measure at 1 cm back from the plate edge and log this temperature using a j type thermocouple read by a MAX31856. Subsequently, a negative-polarity high voltage is applied to the collector, initiating the electrospinning process and starting the experiment. Electrospinning continues for 20 minutes for samples 1-6 (10 minutes for samples 7-13) without any substantial decrease in polymer melt thickness. A schematic of the electrospinning apparatus is provided in Figure 3.1.

3.2.3. Imaging of electrospinning process

A high resolution still images from a Sony camera (Sony, Model a7R IV with Canon EF 180mm f3.5L macro telephoto lens) were utilized for taking top-view still images of the electrospinning process (as shown in figure 3.2). A Utilitech Halogen Stand Work Light was used to side light the electrospinning process to achieve higher contrast images without motion blur. The distance between the center of the simultaneous cones was measured and averaged to get the experimental lambda values for each sample listed in Table 3.1. Along with the top imaging, zoomed-in side-view images were also taken using the same camera and telephoto lens. An LED backlight was

employed for enhanced contrast a reference marking was used to calibrate the length scale. Both the X and Y extension experimental values were measured from these images. All the data presented is averaged over three or more runs.

3.2.4. Rheology and Conductivity measurements

Viscosity was determined from rheological measurements (MCR 302 WESP) in parallel-plate configuration with shear rates of 0.1 to 5%. The reported values are for a set frequency of 1 Hz. Conductivity measurements were performed using two different techniques. For samples 1-6 at a higher processing temperature of 195 °C, a prober system that uses micro-manipulate probe tips to hold the electrode and electrode was heated from the bottom using a temperature controller; the technique has been described in detail elsewhere.⁵ However, the exact conditions for the conductivity measurement matter for sensitive and relatively unstable additives (FE2Pdr and ATMER129 sample 7-13 listed in table 3.1); hence, a homemade in situ fixture was constructed. This home fixture, enabled an interdigitated electrode (Metrohm, 125-digit pairs of 6750 μm length with a 10 μm gap on glass; treated with silanes to reduce the presence of water⁵ to be placed face down on the molten polymer in situ in the electrospinning set-up (conductivity measurements were taken with no applied electrospinning voltage). Nyquist plots were plotted using the data collected from the LCR meter for both these techniques and fitted Fitting procedures utilized RelaxIS software (RHD instruments) and are described in detail in elsewhere.⁵

Table 3.1. The linear low-density polyethylene (LLDPE) formulations utilized in this work with measured values for conductivity and viscosity at the stated electrospinning working temperature.

Sample number	Polymer	Additional Additive	Working temp. (°C)	Viscosity (Pa-s)	Conductivity (S/m)
1	ASPUN 6850		195	299 ± 9	7.3 ± 0.1 x 10 ⁻⁸
2	ASPUN 6850	0.1wt% Hostastat FA38	195	268 ± 8	7.8 ± 0.1 x 10 ⁻⁸
3	ASPUN 6850	5.0wt% Hostastat FA38	195	252 ± 8	2.9 ± 1.0 x 10 ⁻⁶
4	DNDA 1082		195	70 ± 2	6.8 ± 1.1 x 10 ⁻⁸
5	DNDA 1082	0.1wt% Hostastat FA38	195	60 ± 2	8.3 ± 0.1 x 10 ⁻⁸
6	DNDA 1082	5.0wt% Hostastat FA38	195	58 ± 2	1.8 ± 0.1 x 10 ⁻⁶
7	DNDA 1088		165	84 ± 2	4.9 ± 0.3 x 10 ⁻⁹
8	DNDA 1088	1.0wt% Calcium Stearate (CaSt)	165	94 ± 2	3.6 ± 0.1 x 10 ⁻⁸
9	DNDA 1088	5.0wt% Hostastat FA38	165	78 ± 2	1.2 ± 0.1 x 10 ⁻⁵
10	DNDA 1088	5.0wt% ATMER 129	165	68 ± 1	6.9 ± 0.1 x 10 ⁻⁶
11	DNDA 1088	5.0wt% Hostastat FE2Pdr	165	69 ± 2	8.2 ± 0.1 x 10 ⁻⁶
12	DNDA 1088	4.0wt% ATMER 129 + 1.0 wt% CaSt	165	71 ± 9	6.1 ± 0.1 x 10 ⁻⁵
13	DNDA 1088	4.0wt% Hostastat FE2Pdr + 1.0 wt% CaSt	165	72 ± 3	5.6 ± 0.1 x 10 ⁻⁵

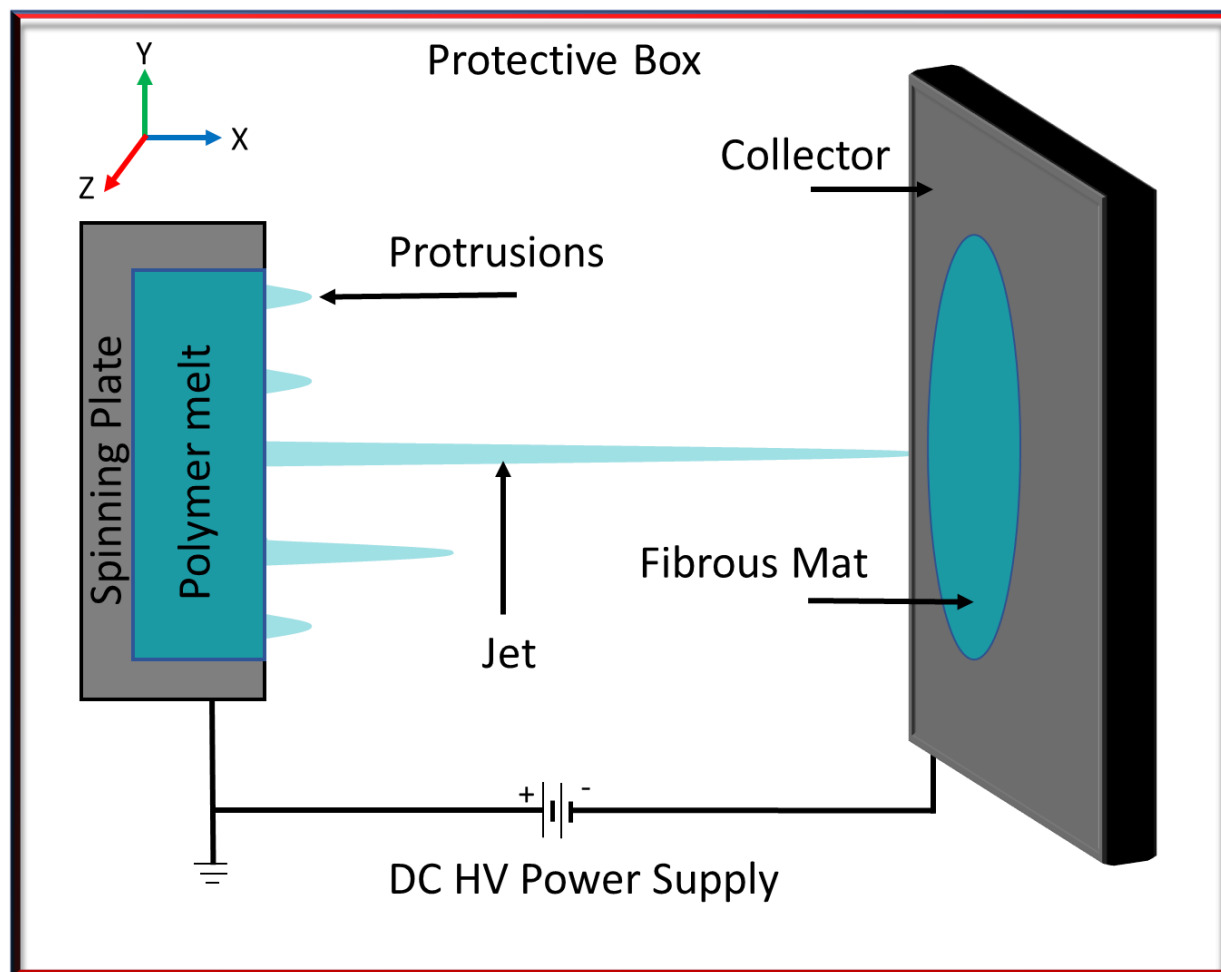


Figure 3.1. (a) Experimental schematic (from above) consisting of two metal plates attached by a high voltage power supply. The grounded source plate resides on the surface of a hot plate (not shown). The polymer melt is shown in blue. After voltage is applied, first protrusions and then cone-jets are formed in the direction of the collector (held at high voltage). Jets thin until the polymer solidifies as a fiber, which is deposited onto the collector.

3.3. Results and Discussion

After voltage is applied, the process of unconfined electrospinning involves several steps, as discussed in detail in previous works.⁶⁻⁸ Figure 1b illustrates a typical case: a thin sheet of polymer is pulled towards the collector, the sheet spontaneously fingers to form many protrusions, and the protrusions convert to equally spaced fiber-forming cone-jets. The conductivity and viscosity of the fluid impact most aspects of the electrospinning process,

including the timing and the size of the characteristic length scales (like cone size)⁵. Evident from Figure 3.2 is that characteristic length scales (up to and including the jet radius, which sets the maximum value for the fiber size), generally decrease with increased conductivity.

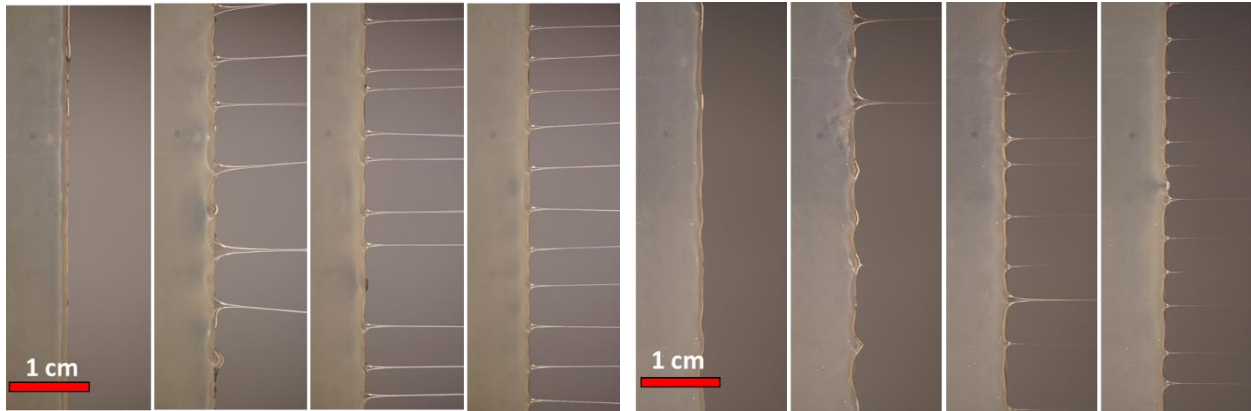


Figure 3.2. (a) Images of the source plate edge at 1, 2, 3, 4 minutes after voltage applied for DND A 1088 at 165 °C. (c) Same as b but for DND A 1088 with 5% FA38 (165 °C) for 1, 1.25, 1.5, 1.75 minutes. For the higher conductivity case, the jet width is noticeably narrower.

We have previously argued⁵ that many of the larger length scales in this process are set by the electric capillary length, κ^{-1} , where the capillary (γ/κ^{-1}) and electric pressures ($\epsilon_0 E^2$) balance. For instance, the thickness of the fluid at the plate edge ($y_1 = \kappa^{-1}$), and the spacing between cone-jets ($\lambda = 3\pi\kappa^{-1}$)⁹ depend on this quantity. In general, capillary lengths are a steady-state relaxation distance (e.g., a flat plate inserted vertically into a fluid will exhibit a stable meniscus (fluid pulled up the plate) controlled by the gravity capillary length) enabling the fluid to smoothly transition (from mobile to stationary or around a perturbation like the plate), with a small enough length/mass scale so that the driving force (i.e., gravity or the electric force) is negligible.¹⁰ The capillary pressure increases with decreased size, and thus dominates at small lengths.

Considering the electric pressure, as in most electrospinning configurations, which utilize either a small radius needle or a sharp plate edge, the electric field has a maximum value at the plate

edge and decreases with distance. Thus, the electric pressure is larger closer to the plate edge. The capillary length at any given location is determined by the local electric field, $\kappa^{-1}(x) = \gamma/\epsilon_0 E^2(x)$, graphed in Figure 3.3 using an electric field from simulations (using ANSYS electromagnetic desktop 2020) as previously described.⁵ and two pertinent values of the surface tension The fluid thins near the edge (height y_1) and slightly protrudes over it (distance x_1): these length scales are similar ($x_1 \sim y_1$ for any given fluid). For the fluid to stably reside at a location x_1 , the capillary length at that location must also be x_1 , as shown with the black line (capillary length = x). Given a particular surface tension, there is a limited range over which this condition is met, which in this case is 300 - 500 μm . Examining the experimental data (Figure 3.4), for Y_1 and $\lambda/3\pi$, we observe that these quantities match well. In addition, they are clustered around the expected region of 300 -500 μm .

These experimentally observed capillary lengths are presented versus conductivity (K) in Figure 5 (solid points). The highest viscosity cases (ASPUN polymer melts with ~ 3 x the viscosity of DNDA) are marked with stars and have higher capillary length for the same conductivity (with a $\eta^{0.4}$ dependence, open symbols). Beginning at low conductivity, as K increases, the capillary length decreases (as $K^{-0.25}$, open symbols). This indicates that increased conductivity increases the electric pressure, which from a molecular perspective is σE where σ is the surface charge density and E is the effective electric field at the surface (setting $\sigma/\epsilon_0 = E$, as a perfect boundary condition results in $\epsilon_0 E^2$). Electrospinning requires a “lossy dielectric” fluid (lying between insulating and conducting behaviors). Some mobile ions must be present to enable surface charge but penetration of the electric field into the interior is also needed to result in bulk transport (i.e., a conductor cannot be electrospun).

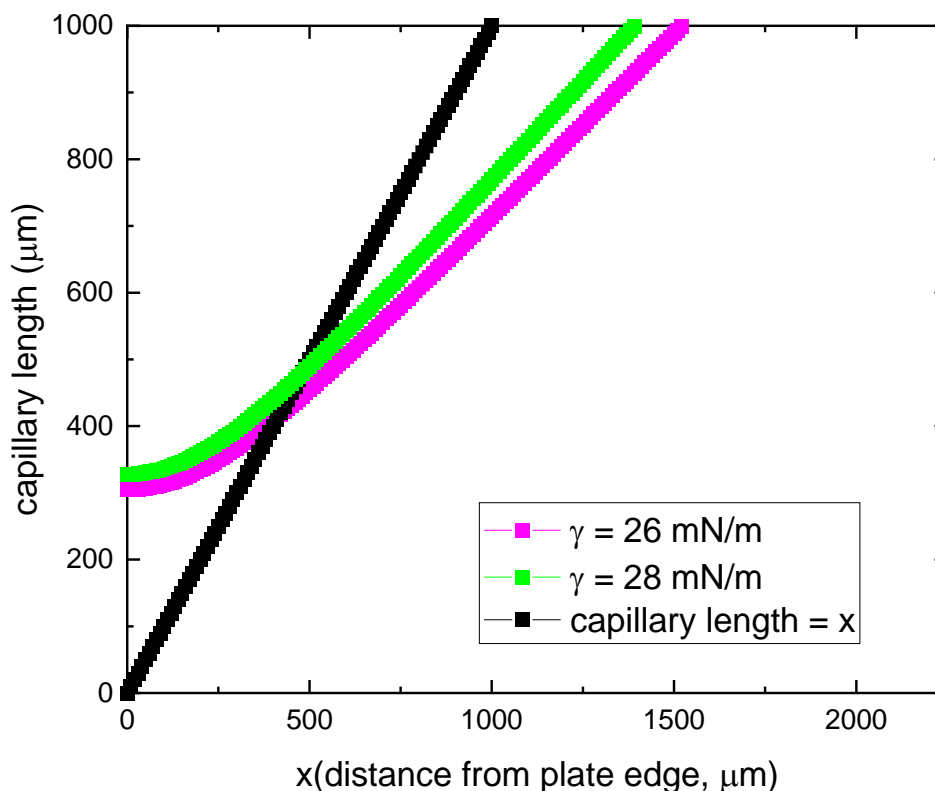


Figure 3.3. Theoretical prediction of the capillary length as a function of distance from the plate edge for a fixed y value utilizing electric field simulation results and reasonable estimates [ref surface tension as a function of temperature] of the surface tension for a linear low density polyethylene melt at 165 -195°C. Experimental tracking of the surface tension as a function of additive was consistent with these limits.

We hypothesize that for low conductivity melts, the charge at the surface is limited by ion availability ($\sigma < \epsilon_0 E_{\text{external}}$) and increases with conductivity. This increases the electric pressure and thus decreases the capillary length. In examining Figure 3.5, upon further conductivity enhancement, the capillary length increases (now as $K^{0.25}$, open symbols), indicating a weakening of the electric pressure. In this case, the internal electric field (E) may be weakening due to enhanced screening, which decreases the electric pressure.

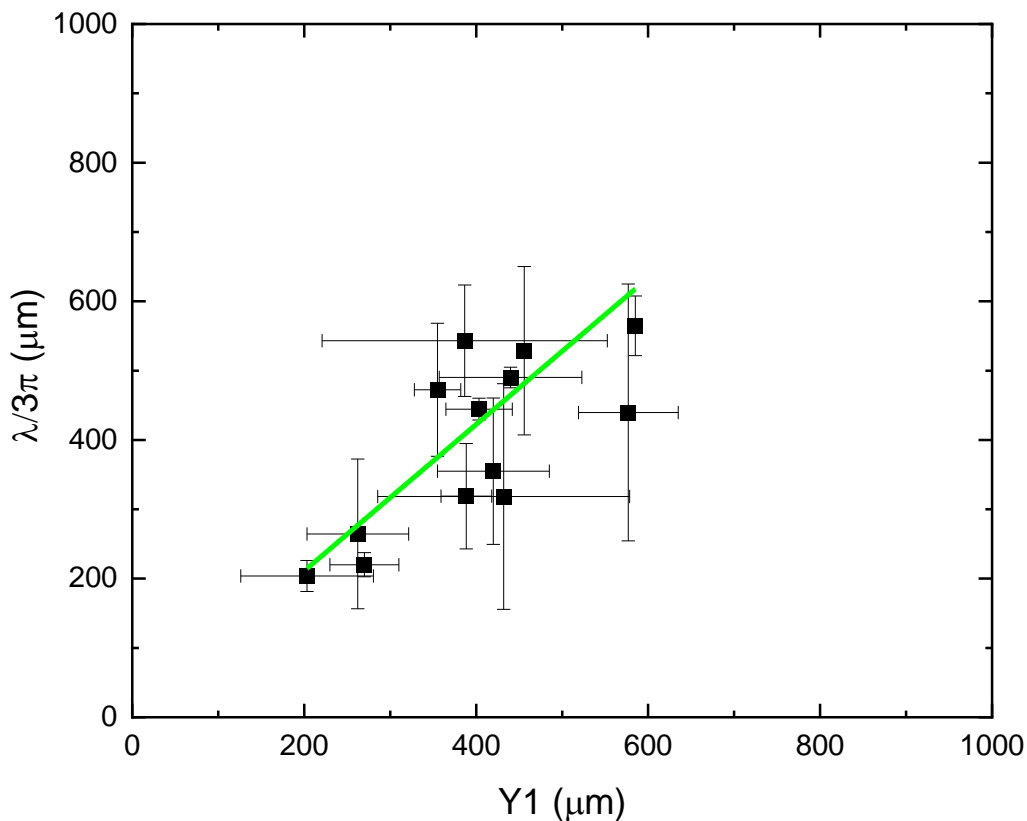


Figure 3.4. For each of the 13 cases (with a minimum of three experiments per case) described in Table 1, the distance between neighboring cone-jets λ , (scaled by 3π) is plotted versus $Y1$ (thickness of the fluid at the plate edge). The fit line has a slope of 1. The values are clustered in the region of 300-500 microns as estimated from Figure 3.

In examining Figure 3.5, upon further conductivity enhancement, the capillary length increases (now as $K^{0.25}$, open symbols), indicating a weakening of the electric pressure. In this case, the internal electric field (E) may be weakening due to enhanced screening, which decreases the electric pressure.

While the larger length scales (cone width, λ , $x1$, and $y1$) clearly reflect conductivity and viscosity, they do not necessarily directly impact fiber size. As discussed in detail in a previous

work⁵, the jet radius occurs at the location where the initial mode of charge transfer, which is bulk conduction $I = \pi r^2 KE$ ($r(x)$ is the radius of the fluid in the cone-jet transition region, $E = E(x)$) transitions to surface convection $I = 2\pi r\sigma v$ ($\sigma(x)$ is surface charge density, $v(x)$ the velocity), the strength of the field due to the surface charge is a significant fraction of the external applied field, and the viscous tension is balanced by the electric pressure.^{5,11} These

constraints lead to $r_{jet} = \frac{\eta^{1/2} Q^{1/3} \epsilon_0^{1/6}}{k^{1/4} E^{1/6}}$, where Q is the flow rate. The only parameter in the r_{jet}

equation with an x dependence is E ; however, using the largest possible electric field range (a factor of 2-3), r_{jet} is only altered by ca. 20% because of the relatively weak $1/6$ dependence.

Thus, r_{jet} is well defined and depends only on fluid properties and one control parameter (Q).

Past the cross-over point where r_{jet} occurs, the jet-fiber radius is theoretically predicted to decrease as $1/x$ (in the absence of a whipping instability, a valid assumption in this work) until the fluid solidifies and the final fiber is formed.

Following this reasoning, r_{jet} sets the maximum fiber size and thus is a crucial parameter to achieve finer fibers. Examining the equation, the strongest dependence is on the flow rate. In unconfined electrospinning, flow rate is not directly controlled by the operator and is relatively constant (for a given applied voltage range) even when significant changes in viscosity and conductivity occur, as summarized in Figure 3.6 for the 13 cases enumerated in Table 3.1. Flow rate for each experimental conditions were determined by calculating the mass throughput value of fiber produced divided by the number of jet-sec and the density of the polymer (assuming the density of the polymer doesn't change significantly over the given process parameters). The number of jets at source plate edge were measured from the videos recorded by using HD camcorder (Sony, Model HDR-CX240) for the entire electrospinning process.

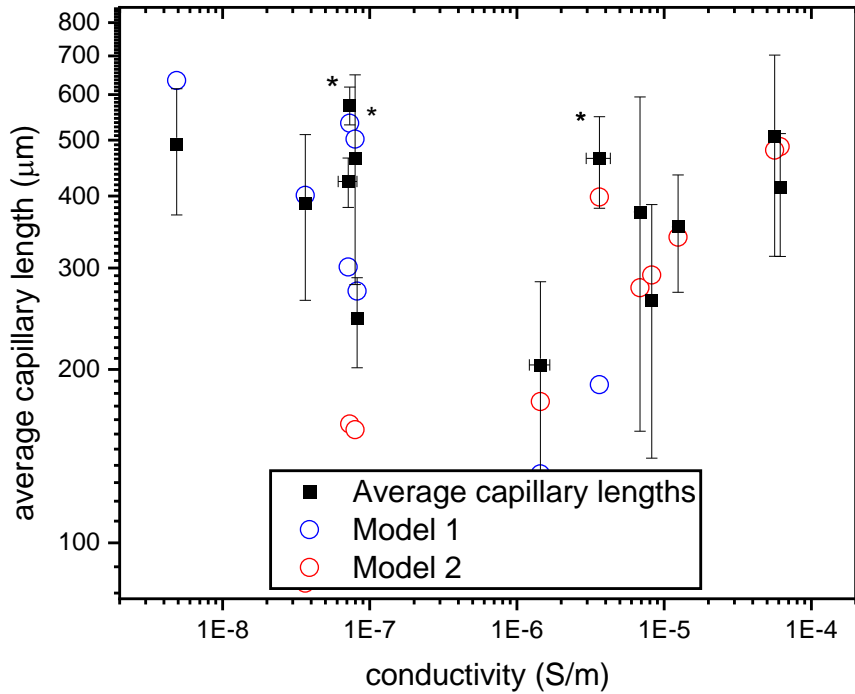


Figure 3.5 Average observed capillary length (from $Y1$ and $\lambda/3\pi$) for each of the 13 cases in Table 1 (filled symbols) plotted versus conductivity. The open symbols are a model: for $K < 1e-6$ S/m, $\kappa^{-1} \sim K^{-0.25}\eta^{0.40}$, for $K > 1e-6$ S/m, $\kappa^{-1} \sim K^{0.25}\eta^{0.40}$. The agreement between model and experiment is good.

This can be understood as follows: $Q = \pi r^2 v$ (at any given location). Considering the near plate region where Q is established, a change in fluid viscosity will inversely change the initial creeping velocity $\sim \gamma/\eta$ but will also proportionally alter the characteristic length scales that determine r near the plate edge ($r^2 \sim (\eta^{0.4})^2 = \eta^{0.8}$) resulting in a near cancellation of the two effects. Similarly, for regions where the conductivity increases electric pressure (and thus driving force and v), characteristic length scales decrease and counteract the effect. Because Q is constant and the r_{jet} dependence on viscosity is negligible (1/12 power), the size of the jet radius is most easily altered by changing the conductivity.

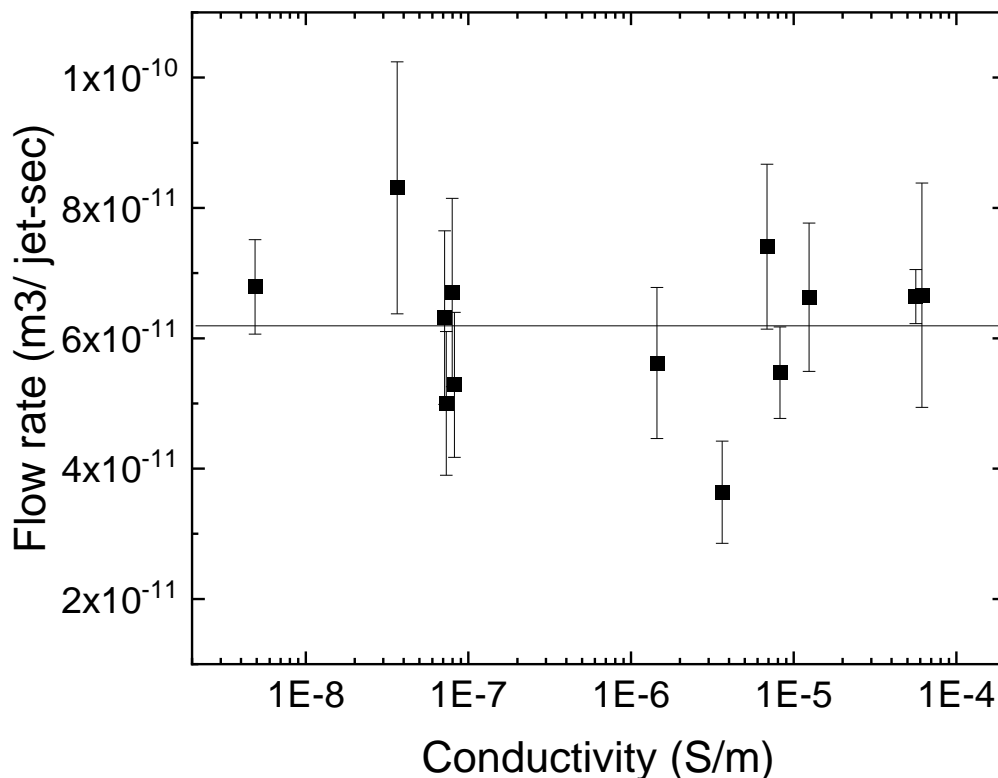


Figure 3.6 Flow rate (measured from mass loss divided by number of jet-seconds determined from videographs of each experiment). The average value over all data is $6.2 \pm 1.1 \text{ m}^3/\text{jet-sec}$ indicated by the horizontal line, which overlaps with the error bar of most points, indicating no dependence on conductivity over 4 orders of magnitude nor viscosity (which varies by a factor of 5, see table 3.1).

The jets in this work were sufficiently narrow, mobile, and removed from the edge where the image was focused that extensive quantitative analysis was hindered. However, fiber size could be directly observed and quantified. Figure 3.7 presents fiber radius as a function of melt conductivity (for all cases shown in Table 3.1). Because some cases (lines 10 and 11 in Table 3.1, ATMER and FE2PDR additives without the presence of calcium stearate) were unstable

with time, resulting in a small number of large fibers, the average fiber radius and standard deviation shown are for the smallest 70% of the fibers for each case.

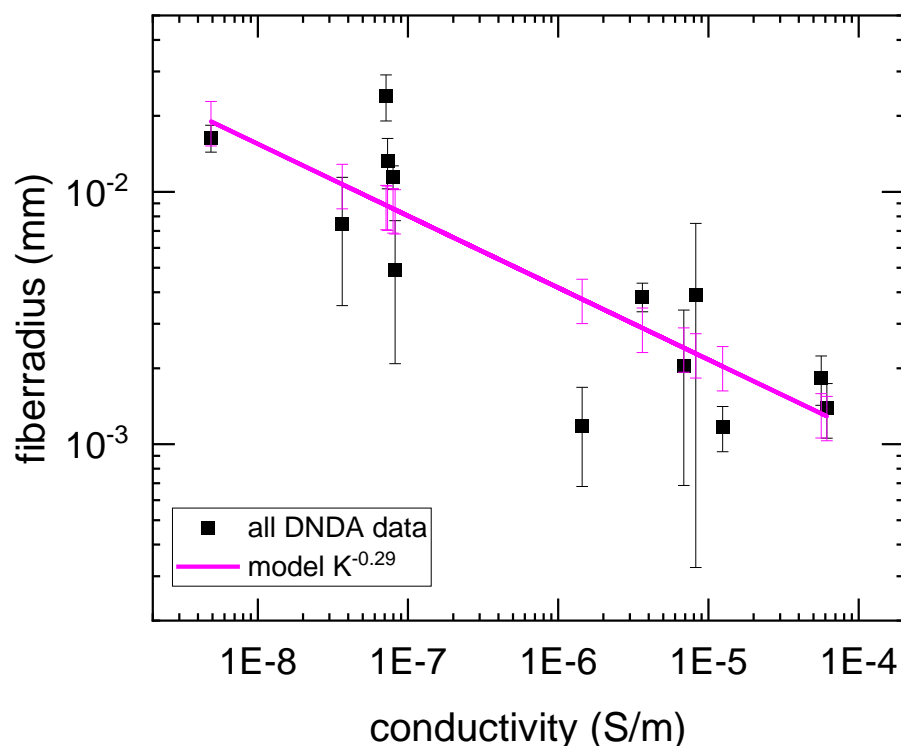


Figure 3.7 Fiber radius for the 13 cases in Table 1 as a function of measured melt ionic conductivity. The fit line has a slope of $K^{-0.29}$.

The raw data shows the same trend, but with larger error bars for some cases. The fit line is $K^{-0.29}$, which is slightly stronger than and consistent with the predicted jet dependence on K . One can also compare these results with previous work where conductivity was tuned for much lower viscosity, higher conductivity solutions to tune fiber size. Data harvested from [Angamma and Jayaram, IEEE Trans. Indust. Appl. 47 1102 (2011)] where conductivity of a polyethylene oxide solution in water was adjusted by adding NaCl (Figure 3.8) shows a very similar trend despite the approximately 5 orders of magnitude lower viscosity, 8 orders of magnitude higher

conductivity, and use of a pumped needle configuration. Overall, this work and comparison indicates that even for highly viscous melts, ionic conductivity plays a crucial role in determining jet size and thus ultimate fiber size.

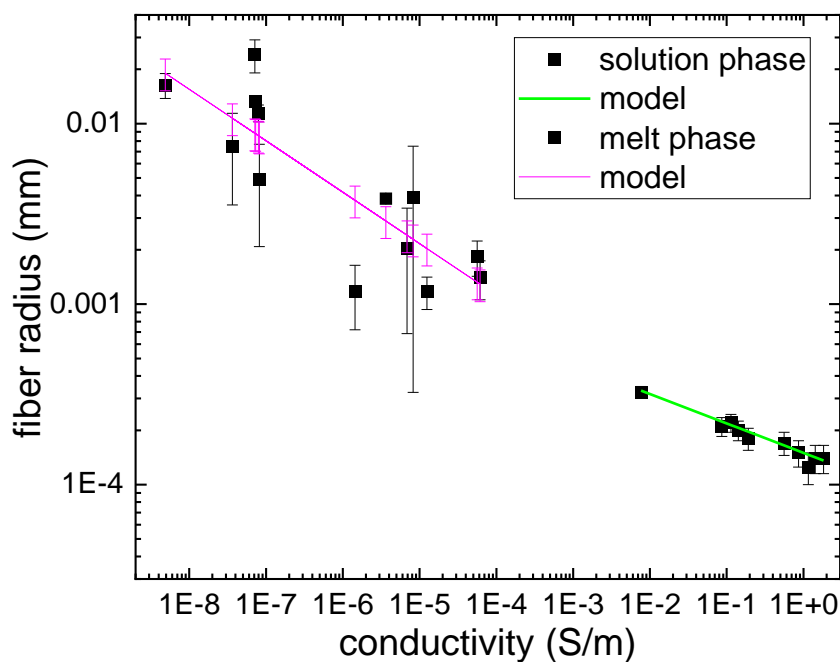


Figure 3.8 Comparison of the fiber radius versus conductivity data in this work to literature precedent with a conductivities 8 orders of magnitude larger. The slope line for the solution phase data (after the original reference [Angamma and Jayaram, IEEE Trans. Indust. Appl. 47 1102 (2011)] is $K^{-0.16}$.

Acknowledgements:

We thank Dow, Clariant, and Corda Technologies for polymer and additive samples.

3.4. References

- 1) Barhate, R.; Ramakrishna, S. Nanofibrous Filtering Media: Filtration Problems and Solutions from Tiny Materials. *Journal of Membrane Science* **2007**, *296* (1–2), 1–8. <https://doi.org/10.1016/j.memsci.2007.03.038>.
- 2) Asmatulu, R.; Khan, W. S. Electrospun Nanofibers for Filtration Applications. In *Synthesis and Applications of Electrospun Nanofibers*; Elsevier, 2019; pp 135–152. <https://doi.org/10.1016/B978-0-12-813914-1.00007-9>.
- 3) Lu, T.; Cui, J.; Qu, Q.; Wang, Y.; Zhang, J.; Xiong, R.; Ma, W.; Huang, C. Multistructured Electrospun Nanofibers for Air Filtration: A Review. *ACS Appl. Mater. Interfaces* **2021**, *13* (20), 23293–23313. <https://doi.org/10.1021/acsami.1c06520>.
- 4) Amna, R.; Ali, K.; Malik, M. I.; Shamsah, S. I. A Brief Review of Electrospinning of Polymer Nanofibers: History and Main Applications. *JNMES* **2020**, *23* (3), 151–163. <https://doi.org/10.14447/jnmes.v23i3.a01>.
- 5) Sheoran, N.; Boland, B.; Thornton, S.; Bochinski, J. R.; Clarke, L. I. Increasing Ionic Conductivity within Thermoplastics via Commercial Additives Results in a Dramatic Decrease in Fiber Diameter from Melt Electrospinning. *Soft Matter* **2021**, *17* (41), 9264–9279. <https://doi.org/10.1039/D1SM01101D>.
- 6) Thoppey, N. M.; Bochinski, J. R.; Clarke, L. I.; Gorga, R. E. Edge Electrospinning for High Throughput Production of Quality Nanofibers. *Nanotechnology* **2011**, *22* (34), 345301.
- 7) Wang, Q.; Curtis, C. K.; Thoppey, N. M.; Bochinski, J. R.; Gorga, R. E.; Clarke, L. I. Unconfined, Melt Edge Electrospinning from Multiple, Spontaneous, Self-Organized

- Polymer Jets. *Mater. Res. Express* **2014**, *1* (4), 045304. <https://doi.org/10.1088/2053-1591/1/4/045304>.
- 8) Thoppey, N. M.; Bochinski, J. R.; Clarke, L. I.; Gorga, R. E. Unconfined Fluid Electrospun into High Quality Nanofibers from a Plate Edge. *Polymer* **2010**, *51* (21), 4928–4936. <https://doi.org/10.1016/j.polymer.2010.07.046>.
- 9) Miloh, T.; Spivak, B.; Yarin, A. L. Needleless Electrospinning: Electrically Driven Instability and Multiple Jetting from the Free Surface of a Spherical Liquid Layer. *Journal of Applied Physics* **2009**, *106* (11). <https://doi.org/10.1063/1.3264884>.
- 10) Gennes, P.-G.; Brochard-Wyart, F.; Quéré, D.; Reisinger, A.; Widom, B. Capillarity and Wetting Phenomena: Drops, Bubbles, Pearls, Waves. *Physics Today - PHYS TODAY* **2004**, *57*, 66–67. <https://doi.org/10.1063/1.1878340>.
- 11) Higuera, F. J. Numerical Computation of the Domain of Operation of an Electro spray of a Very Viscous Liquid. *Journal of Fluid Mechanics* **2010**, *648*, 35–52. <https://doi.org/10.1017/S0022112009993235>.

CHAPTER 4

Optimizing the melt electrospinning parameters to increase the nanofibers count

Neelam Sheoran, Jason R. Bochinski, and Laura I. Clarke**

N. Sheoran, Prof. J. R. Bochinski, and Prof. L. I. Clarke
Department of Physics, North Carolina State University, Raleigh, NC 27695-8202,
United States
Email: jason_bochinski@ncsu.edu and laura_clarke@ncsu.edu

4.1. Introduction

Our previous work has focused on increasing the ionic conductivity in thermoplastic melts with the goal of decreasing jet diameter, which sets the limit on the maximum fiber size. In this section, we discuss other control parameters, including applied voltage, the temperature of the molten polymer, and the temperature in the region where the fiber solidifies (away from the plate). We are particularly focused on the transition from jet to fiber and explore how this step can be controlled.

4.2. Results and Discussion

Figure 4.1 shows example data of fiber diameter versus applied voltage. For voltages below this range, the process is unstable. For voltages above this range, we observe overt frequent streaming discharge which also impacts stability. As the figure indicates, the fiber diameter is not strongly influenced by the applied voltage.

Figure 4.2 shows data at different melt temperatures and voltages. A general decrease in fiber diameter with increasing temperature is observed. Based upon our analysis of data at 165 and 195 deg. C, correlating those results with the measured viscosity and conductivity, the decrease in fiber diameter with increased temperature is likely due to increased melt ionic conductivity.

We note that for all cases explored, a minimum average fiber diameter of 2 microns is observed. For instance, considering the optimal value of -51 kV in Figure 4.2, there is no effect of temperature on average fiber diameter from 165 to 195 deg. C.

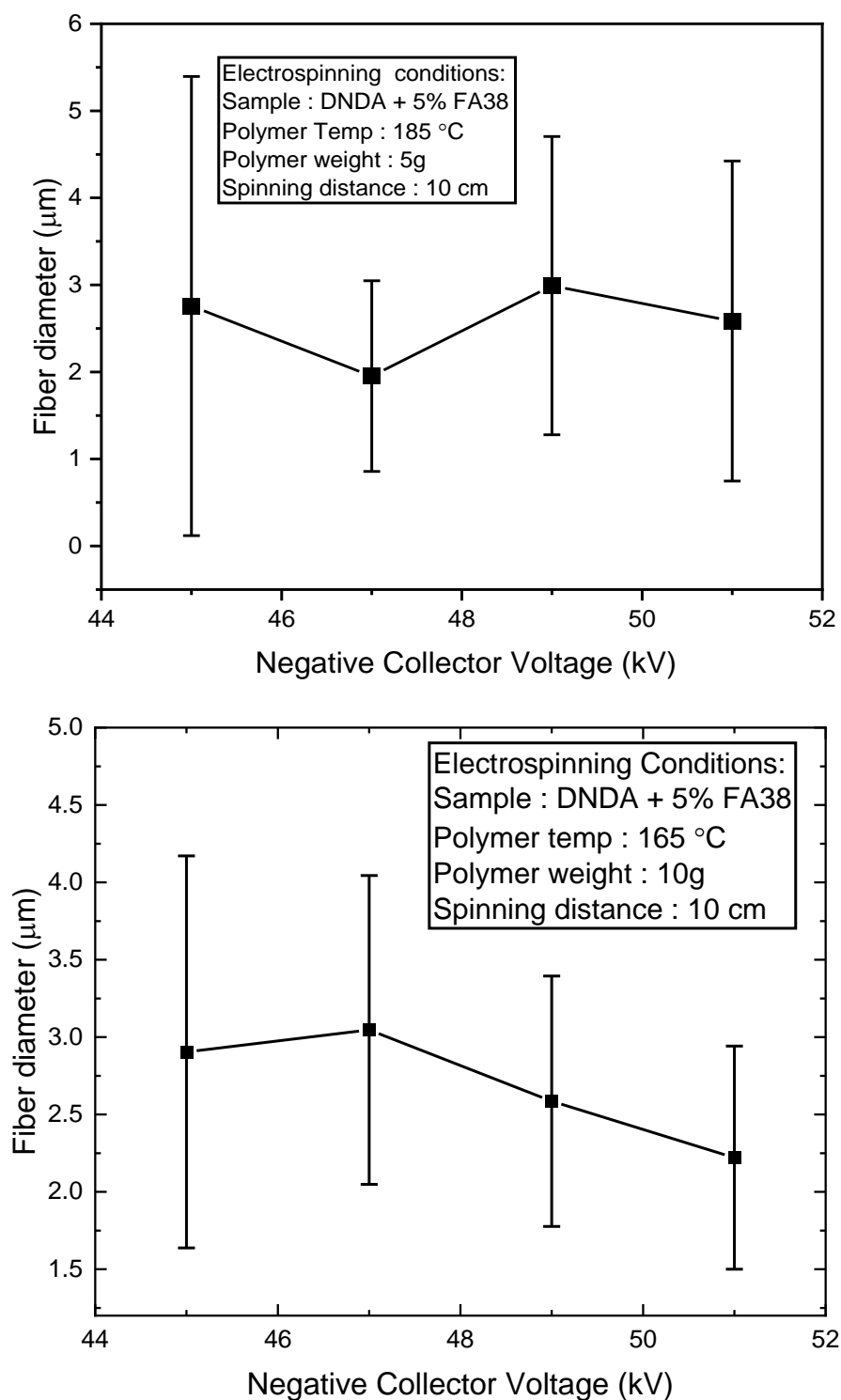


Figure 4.1. Fiber diameter as a function of applied voltage for DNDA 1088 with 5wt% FA38 with a) 5 g of polymer melt at 185 deg. C and b) 10 g of polymer melt at 165 deg. C. No significant change is observed as voltage is altered over the working range

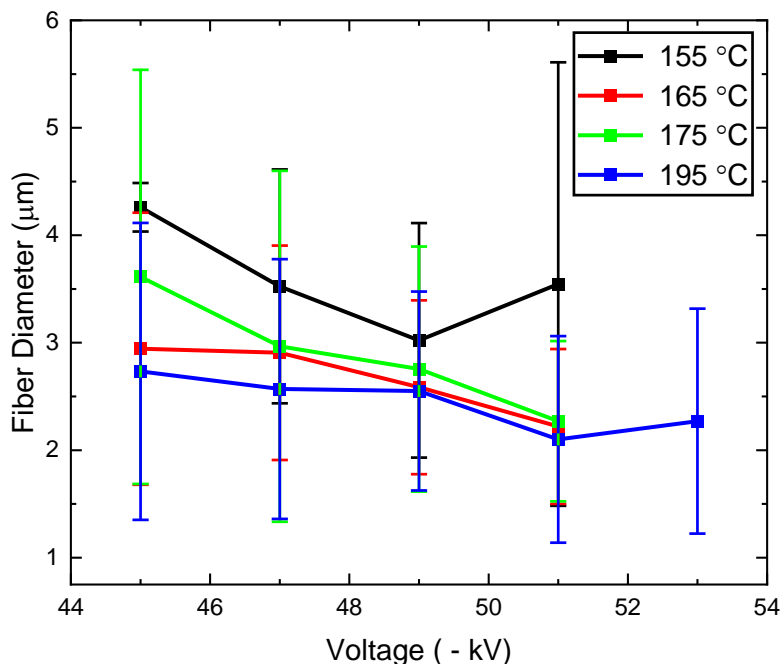


Figure 4.2. Fiber diameter versus applied voltage for different melt temperatures of DNDA 1088 with 5wt% FA38 (10 grams on plate). A general decrease with temperature is observed.

An example of a minimum fiber size difficult to alter through processing parameters is shown in Figure 4.3. Here, the elongation region, past the plate edge, where the jet transitions into a fiber has been heated. This should decrease the viscosity in the elongation region and potentially enable further fiber thinning. The black data shows the neat DNDA case, which has a low conductivity and a resultant larger jet diameter, and ultimate fiber diameter. In this case, increasing the elongation region temperature, results in a significant decrease in fiber radius, by ca. a factor of 3. However, consider the other cases in the graph with significantly higher (by 4 orders of magnitude) ionic conductivity and correspondingly smaller fiber diameters. Here the change in fiber radius when increasing the background temperature is only about 10%. These

observations will be further explored in work beyond this thesis.

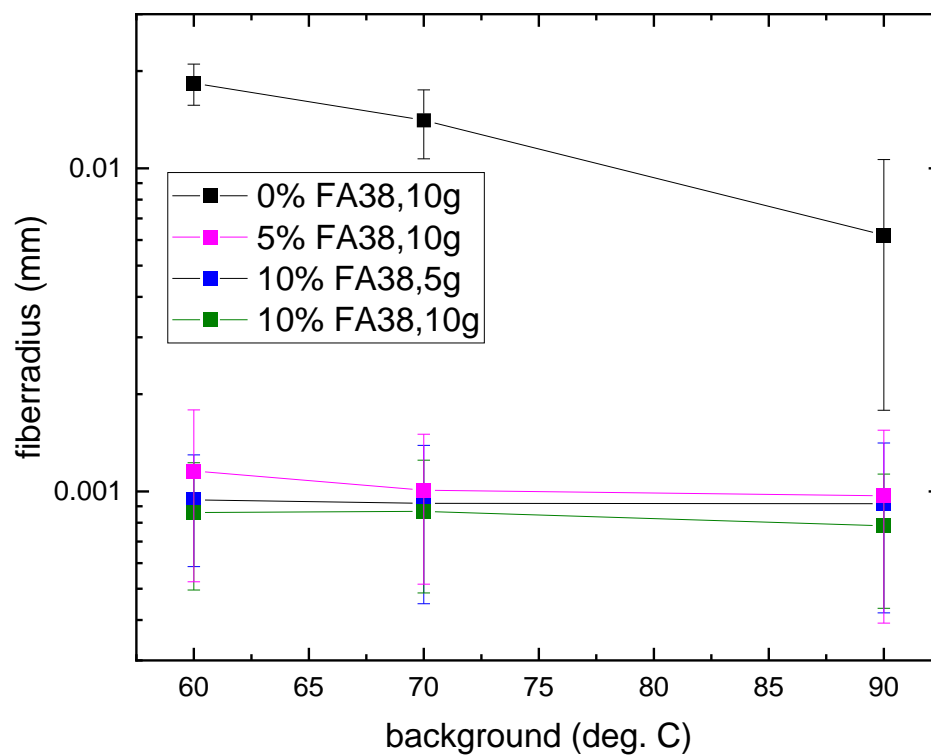


Figure 4.3. Fiber radius for various formulations where the region beyond the plate where elongation of the jet into a fiber occurs.

CHAPTER 5

5. 1. Conclusion

Compared with the current meso fibers, melt-spun fibers have improved mechanical properties and other attributes such as recyclability and low cost, making them an ideal candidate for air/water filtration applications.¹⁻³ In the last few years, many developments have been made in improving the melt electrospinning setups due to the limitation of needle clogging and low throughput in using traditional needle electrospinning setup. Numerous studies utilizing these recent setups were conducted to understand the impact of different external parameters such as polymer melt temperature, electric field, ambient temperature, and humidity to get smaller fibers.⁴⁻⁷ However, the average diameter of fibers produced is usually around tens of microns, except for a couple of exceptions.^{1,8,9} Usually, the high viscosity of polymer melt is blamed for such a large fiber diameter, and researchers have found that reducing the viscosity does improve the fiber diameter.¹⁰⁻¹⁵ However, the effect of ionic conductivity of the polymer melt is still underexplored and an area that needs more comprehensive research. It has been discussed that fiber diameter in solution electrospinning results in nanoscale range due to initial jet elongation and whipping.^{9,10,16} However, for melt electrospinning, due to low ionic conductivity and larger initial jet diameter, the whipping region has not been reported.

In this Ph.D. dissertation, the ionic conductivity of the thermoplastics was modified by five orders of magnitude (10^{-9} to 10^{-4} S/m) to obtain the average fiber diameter of less than 2 microns. The viscosity of the polymer also varied by a factor of four (50 – 200 Pa-s). Throughout this thesis, four different additives with three different types of LLDPE polymers of different additive packaging and viscosities were used (a maximum of 5wt% additive in the polymer was used) to

obtain this conductivity range in thirteen different stable spinning cases. The effects of manipulating the ionic conductivity on various characteristics length scales (such as protrusions, cone radius, jet spacing (λ), and jet radius) were analyzed using different fluid models. A capillary length model was used to establish the importance of capillary length in setting different length scales such as protrusions, cone radius, and jet spacing. Average capillary length first decreased (as $K^{-1/4}$) and then increased (as $K^{1/4}$) with an increase in the conductivity, suggesting that capillary length does not necessarily govern the formation of fiber radius as it consistently decreases with an increase in conductivity. Analysis done in this thesis revealed that ionic conductivity plays a significant role in setting the initial jet diameter, which sets the upper limit on the fiber size despite the given range of viscosities. In addition to this, our model suggests that both jet and fiber radius scales as $K^{-1/4}$, which matched well with existing solution-phase electrospinning even with eight orders of magnitude higher conductivity and four orders of magnitude lower viscosity.

Our studies¹⁷ and other reports¹⁸ also observed that jet solidification point could impact the size of fibers. As the external electrostatic force can stretch the jet only in its melted form, the longer the jet stays melted, the more stretching can be applied, causing thinner jets and thinner fibers. Hence, to increase the length of the melted jet, the ambient temperature was increased, an average fiber diameter of ~ 1.5 microns was observed with more than 30% nanofibers (averaged around 400nm). A further investigation on optimizing various parameters, including a system that can provide uniform heating, could help decrease the average fiber diameter to less than a micron.

In this work, the conductivity of thermoplastic melts was changed from very low to being moderately conductive. In the next phase of this project, to test the model of fiber radius scaling

as ($K^{-1/4}$), a further increase in the conductivity of the melt (through different additives or by tuning the proportion of the existing ones) would be explored to decrease the further fiber radius, without compromising the quality of fibers by keeping a minimum level of additive weight percentage.

5.2. References

- (1) Shabani, E.; Gorga, R. Effect of the Spin-line Temperature Profile on the Mechanical Properties of Melt Electrospun Polyethylene Fibers. *Journal of Applied Polymer Science* **2021**, *138*. <https://doi.org/10.1002/app.50668>.
- (2) Koenig, K.; Beukenberg, K.; Langensiepen, F.; Seide, G. A New Prototype Melt-Electrospinning Device for the Production of Biobased Thermoplastic Sub-Microfibers and Nanofibers. *Biomaterials Research* **2019**, *23* (1), 10. <https://doi.org/10.1186/s40824-019-0159-9>.
- (3) Borojeni, I. A.; Gajewski, G.; Riahi, R. A. Application of Electrospun Nonwoven Fibers in Air Filters. *Fibers* **2022**, *10* (2), 15. <https://doi.org/10.3390/fib10020015>.
- (4) Liu, Y.; Deng, R.; Hao, M.; Yan, H.; Yang, W. Orthogonal Design Study on Factors Effecting on Fibers Diameter of Melt Electrospinning. *Polymer Engineering & Science* **2010**, *50* (10), 2074–2078. <https://doi.org/10.1002/pen.21753>.
- (5) Xie, G.; Chen, Z.; Ramakrishna, S.; Liu, Y. Orthogonal Design Preparation of Phenolic Fiber by Melt Electrospinning. *J. Appl. Polym. Sci.* **2015**, *132* (38), n/a-n/a. <https://doi.org/10.1002/app.42574>.
- (6) Mu, X.; Zheng, Y.; Li, X.; Xin, B.; Lin, L. Effects of Temperature on Melt Electrospinning: Experiment and Simulation Study. *Fibers Polym* **2021**, *22* (4), 964–971. <https://doi.org/10.1007/s12221-021-0465-4>.
- (7) Liu, Y.; Li, X.; Ramakrishna, S. Melt Electrospinning in a Parallel Electric Field. *Journal of Polymer Science Part B: Polymer Physics* **2014**, *52*. <https://doi.org/10.1002/polb.23511>.

- (8) Malakhov, S. N.; Chvalun, S. N. Melt Electrospinning of Polyethylene Fibres for Oil Collection from Water Surface. *J. Phys.: Conf. Ser.* **2019**, *1347* (1), 012082. <https://doi.org/10.1088/1742-6596/1347/1/012082>.
- (9) Deng, R.; Liu, Y.; Ding, Y.; Xie, P.; Luo, L.; Yang, W. Melt Electrospinning of Low-Density Polyethylene Having a Low-Melt Flow Index. *Journal of Applied Polymer Science* **2009**, *114*, 166–175. <https://doi.org/10.1002/app.29864>.
- (10) Effect of viscosity and electrical conductivity on the morphology and fiber diameter in melt electrospinning of polypropylene - Rajkishore Nayak, Rajiv Padhye, Ilias Louis Kyratzis, Yen Bach Truong, Lyndon Arnold, 2013 <https://journals.sagepub.com/doi/abs/10.1177/0040517512458347> (accessed 2022 -03 -22).
- (11) Nayak, R.; Ilias, I.; Kyratzis, I.; Yen, Y.; Rajiv, P.; Arnold, L. Melt-Electrospinning of Polypropylene with Conductive Additives. *Journal of Materials Science* **2012**, *47*, 6387–6396. <https://doi.org/10.1007/s10853-012-6563-3>.
- (12) Wang, X.; Huang, Z. Melt-Electrospinning of PMMA. *Chin J Polym Sci* **2010**, *28* (1), 45–53. <https://doi.org/10.1007/s10118-010-8208-9>.
- (13) Li, H.; Chen, H.; Zhong, X.; Wu, W.; Ding, Y.; Yang, W. Interjet Distance in Needleless Melt Differential Electrospinning with Umbellate Nozzles. *Journal of Applied Polymer Science* **2014**, *131* (15). <https://doi.org/10.1002/app.40515>.
- (14) Zhiyuan, C.; He, J.; Fengwen, Z.; Yuexing, L.; Yong, L.; Huilin, Y. Effect of Polar Additives on Melt Electrospinning of Nonpolar Polypropylene. *Journal of the Serbian Chemical Society* **2014**, *79* (5), 587–596.

- (15) Malakhov, S. N.; Dmitryakov, P. V.; Pichkur, E. B.; Chvalun, S. N. Nonwoven Materials Produced by Melt Electrospinning of Polypropylene Filled with Calcium Carbonate. *Polymers* **2020**, *12* (12), 2981. <https://doi.org/10.3390/polym12122981>.
- (16) Rangkupan, R.; RENEKER, D. Electrospinning Process of Molten Polypropylene in Vacuum. *J. Met. Mater. Miner.* **2003**, *12*.
- (17) Sheoran, N.; Boland, B.; Thornton, S.; Bochinski, J. R.; Clarke, L. I. Increasing Ionic Conductivity within Thermoplastics via Commercial Additives Results in a Dramatic Decrease in Fiber Diameter from Melt Electrospinning. *Soft Matter* **2021**, *17* (41), 9264–9279. <https://doi.org/10.1039/D1SM01101D>.
- (18) Shabani, E.; Azimi Yancheshme, A.; Ronen, A.; Gorga, R. Effect of the Spin-Line Temperature Profile on the Translocation of the Solidification Point and Jet Thinning in Unconfined Melt Electrospinning. *ACS Applied Polymer Materials* **2020**, *3*. <https://doi.org/10.1021/acsapm.0c01082>.

APPENDICES

Appendix A-1

A-1.1. Conductivity measurement

A-1.1.1. Impedance spectroscopy

Impedance spectroscopy (IS) is a rapid and easily automatized technique to investigate the electric properties of diverse types of materials¹. The basic assumption for impedance measurement is that the electrode–material system properties are time-invariant. Hence, the IS method is used to determine the material properties and their dependencies on various controllable variables such as temperature, pressure, and applied static voltage or current bias.

The most common method for IS measurement is to apply an electrical stimulus (a known voltage or current) to the electrodes and observe the response (the resulting current or voltage). An ideal dielectric only "conducts" through reorientation of permanent dipoles or formation of induced dipoles in the presence of the electric field. Since different dipole motions occur at different time scales and because there is no steady state current in this case (after some time all dipoles have reoriented or formed, and the current goes to zero) a time-varying voltage is used. In the presence of varying voltage, when an ideal dielectric (with no losses, and almost instantaneous dipole response) conducts, the voltage and current are out of phase by $\pi/2$. However, for a real dielectric material (often characterized by the dielectric constant, ϵ_r , which is a measure of the number of dipole that can respond at a particular frequency) there is a delay in the response, causing V and I to be out of phase by $\pi/2 - \delta$, where δ is the known as loss angle. Using these measurements, a complex quantity $Z = V/I$ known as impedance is calculated for the system. Impedance is defines as the effective resistance of an electric circuit occurring from the combined effects of ohmic resistance (related to charge actually flowing through the material, like an ion moving through a polymer) and reactance (the effect of dipole reorientation and capacitance charging), and has two

components, i.e., real impedance, and imaginary impedance, as shown in Figure A-1.1 and is defined as $Z = Z' + iZ''$, where Z' is real impedance, Z'' is imaginary impedance and, $\tan(\delta) = Z'/Z''$

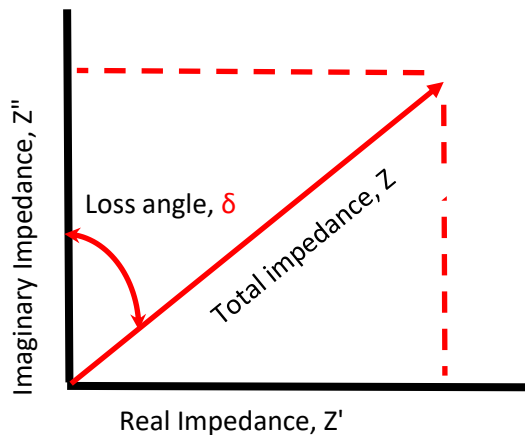


Fig A-1.1. A graphical representation of the complex impedance plane

Apart from impedance, other derived quantities, namely admittance Y , modulus M , and relative permittivity ϵ , are used for IS data analysis. For this thesis we will focus on impedance, dielectric loss tangent ($\tan\delta$), dielectric permittivity and ac conductivity to analyze the effect of different temperatures and additive wt%.

We will be using some of these quantities to understand the conductive behaviors of thermoplastic melts, modelled as leaky dielectrics, and how it changes with temperature and various additives. For these studies, we will also be using Broadband Dielectric Spectroscopy (BDS) analysis, a subsection of IS focusing on studying dipolar molecular relaxations and characterizing the dynamics of ion motion.^{2,3}

A-1.1.2. Measurement Techniques

A-1.1.2.1. Prober System

For this analysis, two different instruments were used. The Andeen-Hagerling AH2700A Ultra-Precision Capacitance Bridge (CB) can quantify conductivities down to 10^{-13} S/cm, but only over a relatively narrow frequency range (50Hz – 20kHz). The Hikoi IM3533-01 LCR meter is less sensitive (probing conductivities from 10^{-10} S/cm to 10^1 S/cm) but over a much larger frequency range (1 mHz – 200 kHz). For a detailed understanding of how the CB and LCR meter operate, please refer to the reference⁴. CB data taking was automated using LabView Software. The user inputs a frequency range and averaging parameters, along with the amplitude of the applied voltage. Capacitance and tan(delta) values are recorded. The LCR meter uses proprietary software and saves measurements to a USB drive: output values are total impedance, and phase angle.

Two measurement systems were used to make contact with an interdigitated electrode containing the polymer melt. The Prober system (Lakeshore, as shown in Figure A-1.2a, uses micro-manipulate probe tips, as shown in Figure A-1.2c. Measurement were made at ambient, elevated temperatures, or using turbo (Varian model #9699365) and scroll pumps (Varian model # SH-110), create a vacuum pressure in the range of 10^{-5} torr. A temperature controller (LakeShore #331) was used to vary the temperature from room temperature (20 °C) to 200 °C.

The second experimental set-up enabled measurement of the surface of the polymer melt in-situ in the experimental electrospinning apparatus.

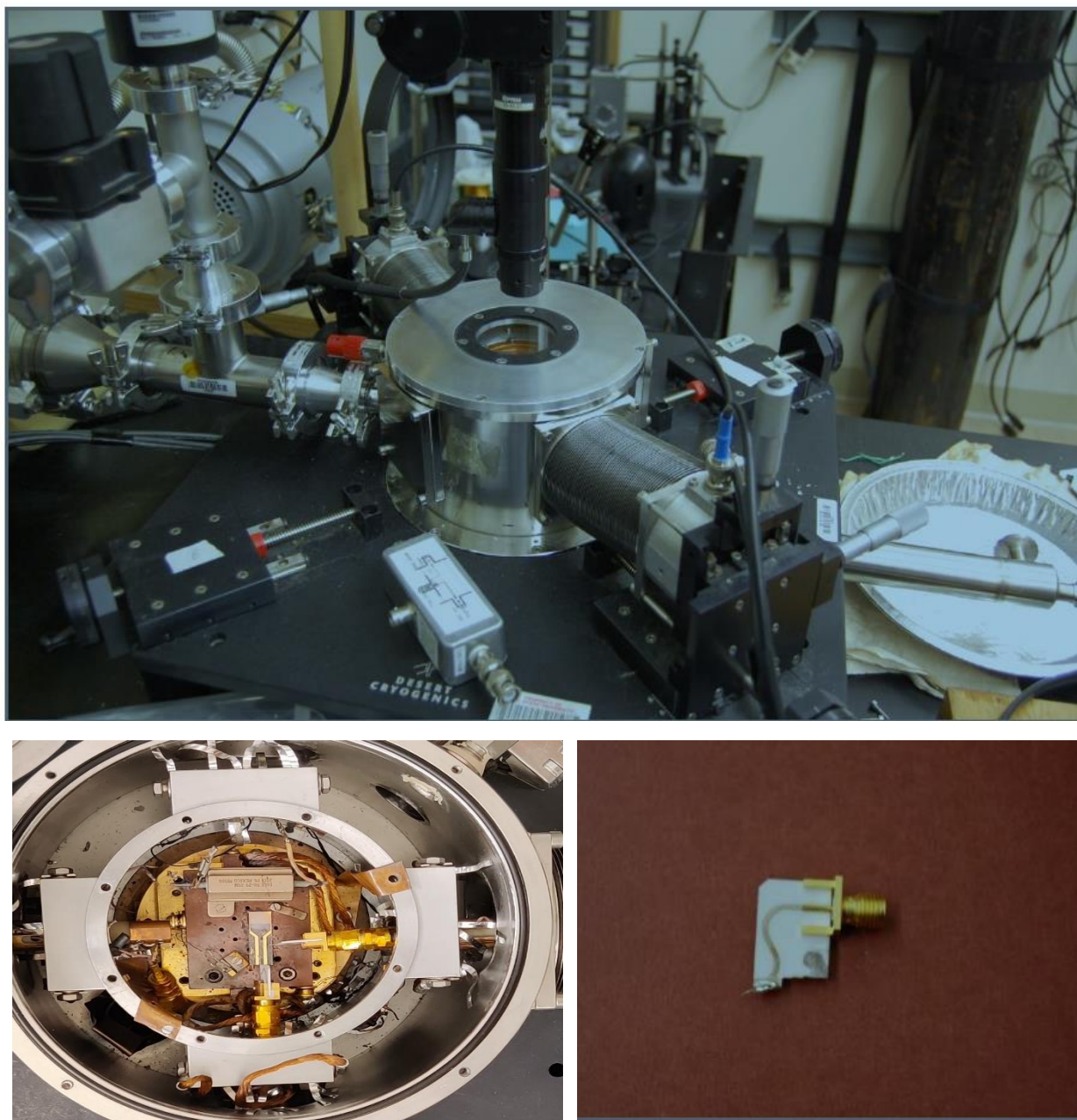


Figure A-1.2. (Top) Prober system setup with two probe arms and metal stage chamber (Bottom Left) Close up of metal stage chamber with IDE loaded with polymer sample (Bottom right) Close up of the probe.

A-1.1.2.2. In-situ conductivity measurement: equipment modification

Some additives with low melt temperatures, such as Hostastat FE2Pdr and ATMER 129 used in Chapter 3 evaporate as soon as they start to melt. This means that the exact conditions of the

conductivity measurement are important. Hence instead of melting the polymer on the electrode to form polymer film, an in-situ fixture was constructed. This fixture is shown in figure A-1.3 and was utilized instead of technique 1 (Prober) for conductivity measurements presented in chapter 3. The polymer was melted on the metal source electrospinning plate residing on the hot plate within the electrospinning set-up and heated to reach the measurement temperature. Once the temperature was reached, the fixture was put in place and impedance measurements were performed using LCR meter. Some electrical noise was observed in the data while using the fixture. For reference, pure DNDA 1088 and DNDA 1088 + 5% FA38 for the given temperature was measured using both the fixture and prober. There was no significant difference in conductivity measure with the two different measurement techniques (Prober and in-situ) for pure DNDA 1088, which indicates that the fixture provides accurate data. However, an increase in conductivity (conductivity is higher than measured in the Prober configuration) for DNDA 1088 + 5% FA38 was observed (shown in figure A-1.4). The increase in the conductivity could be due to decreased evaporation (there is a larger mass of the polymer on the metal plate compared to film on the electrode, thus decreasing the surface area to volume, and thus potentially the evaporation rate). Also, since the additive works by moving to the surface of the polymer when melted, flipping the electrode and placing it on the surface could have caused increase in the conductivity.

Using the in-situ fixture, it was noted that the conductivity of DNDA 1088 with additives changes with time. For example, change in conductivity with time for DNDA 1088 + 5%FA38 is shown at the end of the appendix in Figure A-1.13. For the ATMER and FE2Pdr additives, the conductivity changed by orders of magnitude with time as shown in Figure A-1.14. Due to this reason, the time for electrospinning run with these compounds was reduced from 20 m (in chapter 2) to 10 m (in chapter 3) and the working temperature was reduced by 30 °C. At lower temperature, this

conductivity change was less dramatic but still significant. These results indicated that FA38 is more stable additive in this temperature range than ATMER and FE2Pdr. Hence FA38 was chosen for fiber diameter optimization for chapter 4.

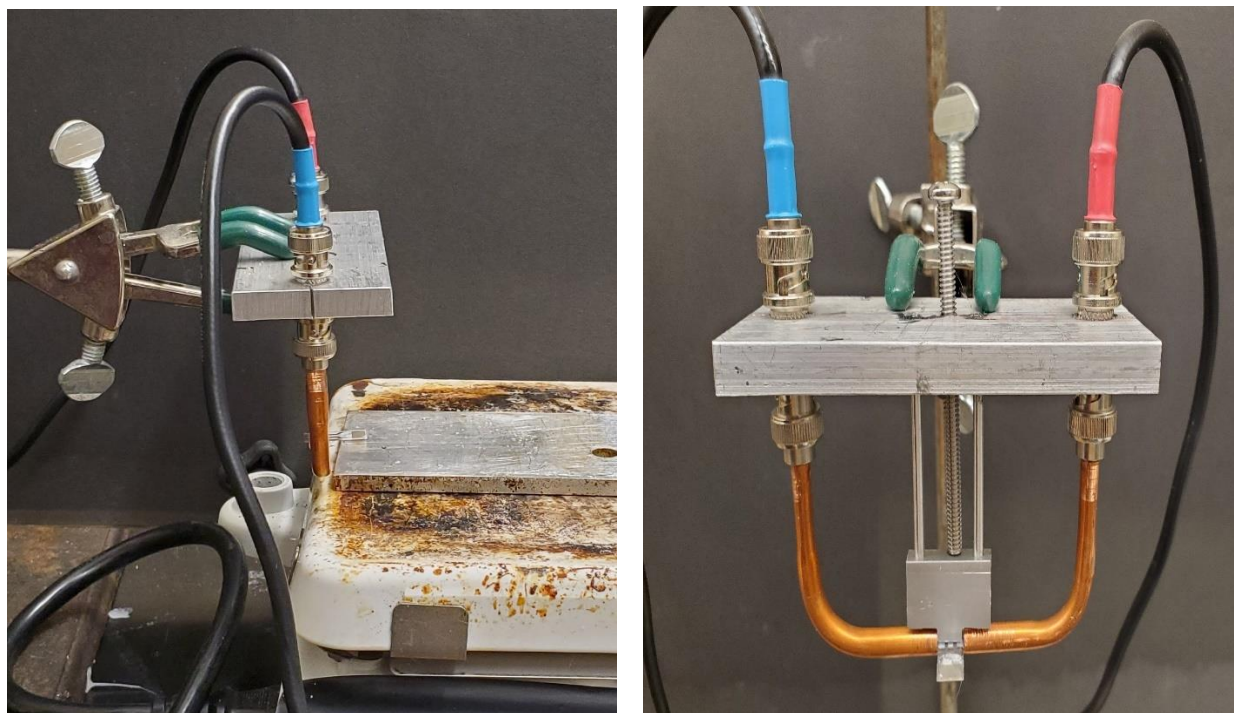


Figure A-1.3. In-situ measurement setup a) side view and b) front view, holding the IDE along with metal plate sitting on the hot plate

The CB output values, Capacitance (C) and $\tan(\delta)$ as a function of ω were converted to the real and imaginary impedance using following equations:

$$Z' = R / (1 + R^2 \omega^2 C^2)$$

$$Z'' = R^2 \omega C / (1 + R^2 \omega^2 C^2), \text{ Where } R = 1 / \omega C \tan \delta$$

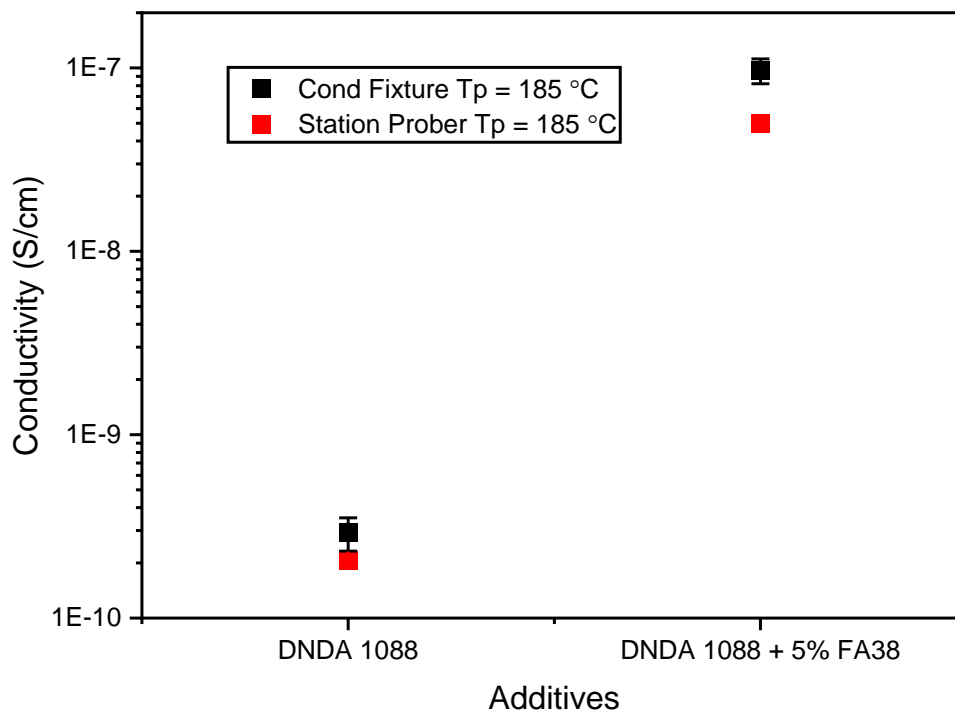


Figure A-1.4. Conductivity as a function of pure DNDA 1088 and DNDA 1088 + 5% FA38 is plotted for two measurement techniques (black squares – in-situ measurement and red square – station prober measurement)

Nyquist plots (as shown in figure A-1.7) were constructed and fitted using equivalent R-C circuits by utilizing Zview or RelaxIS software.

The LCR generally output impedance and loss angle converted to get real and imaginary impedance value as:

$$Z' = Z \sin(\delta), \quad Z'' = Z \cos(\delta)$$

Final conductivity values were calculated from the bulk resistance value (R in the RC model, which reflects the resistance to ionic current) obtained from the Nyquist fit using the interdigitated electrode cell constant value (which reflects the effective cross-sectional area and distance between electrodes). Interdigitated electrode cell constants were provided by the manufacturer and

confirmed by taking IS data of the conductivity standard (a solution with known ionic conductivity). Python programs (shared at the end of this appendix) were used to automate calculations and conversions.

A-1.1.2.3. Interdigitated electrodes

Gold interdigitated electrodes (IDE) (Metrohm) with 125-digit pairs of 6750 μm length and a 10 μm gap residing on a rectangular glass substrate ($22.8 \times 7.6 \times 0.7$ mm in size) (Figure A-1.5) were used for measurements.

An IDE is a long open-faced capacitor. Each contact pad connects to an electrode that has many evenly spaced protrusions (fingers)⁴. The fingers interleave with those from the other electrode creating a large surface area, small gap capacitor, with an open surface on which a material under test can be placed. Figure A-1.6 shows a comparison between electric field lines of a parallel plate capacitor and an IDE. The electric field lines penetrate through the material under test and thus the impedance can be determined. IDEs on glass produced a cell constant that was relatively constant with temperature and enabled sensitive measurements, limited only by the ionic conductivity of the glass ($\sim 1 \times 10^{-11}$ S/cm at T_m and $\sim 2 \times 10^{-10}$ S/cm at 190 °C). For these experiments, IDEs were UV-ozone cleaned for 30 minutes (Bioforce Nanosciences UV-Ozone Procleaner), followed by rinsing with isopropyl alcohol, and submersion for 12 hours in 1000:1 (toluene: dimethyl decyl chlorosilane) solution. The silane reacts with surface hydroxyl groups and replaces them with methyl and decyl groups, which results in a hydrophobic surface and reduces water contamination of the electrodes. After silanization, IDEs were rinsed with toluene, sonicated in methanol for 2 minutes, and stored in a closed container until use.

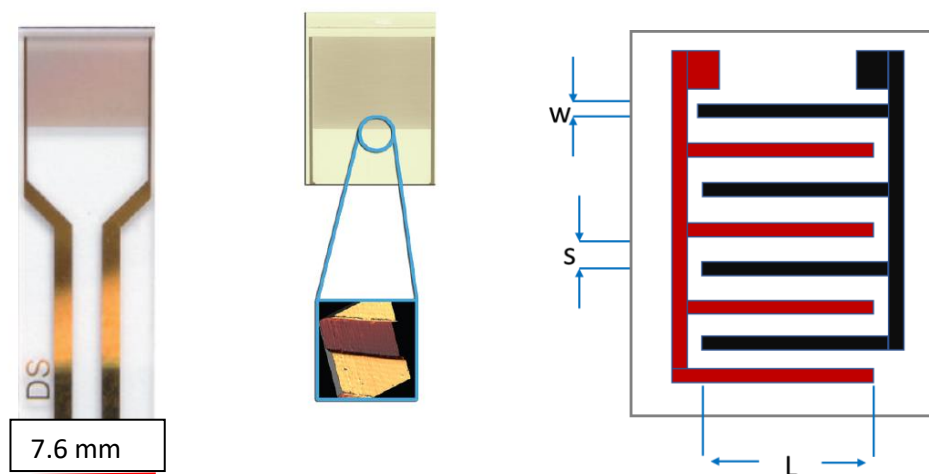


Figure A-1.5. a) Metrohm 10 μm bands/gaps Gold interdigitated on glass substrate b) Stereo microscope (top) and AFM 3D (bottom) images of G-IDEAU10, 10 μm bands/gaps IDE c) Schematic of planar interdigitated electrode.

For measurement technique 1 (Prober), polymer (cryoground into powder with and without additives) was placed on an individual IDE, heated on a hot plate to 140 $^{\circ}\text{C}$, and then allowed to cool to form a polymeric film. The resultant polymer film was placed on the prober metal stage.

For measurement technique 2 (in-situ), a gig held the interdigitated electrode and wiring in place and was inverted to place the surface of the IDE onto the surface of the molten polymer on the electrospinning plate.

Conductivity of different polymer samples at various temperatures with and without additives was measured. Three different types of pure (as obtained from DOW) LLDPE polymers namely ASPUN 6850A, DNDA 1082 and DNDA 1088 of varying melt flow index along with four different types of additives namely Hostastat FA38, Hostastat FE2Pdr, ATMER 129 and Calcium

Stearate were used Varied wt% (0.1% – 10%) of these additives were mixed with the pure polymers to perform these measurements.

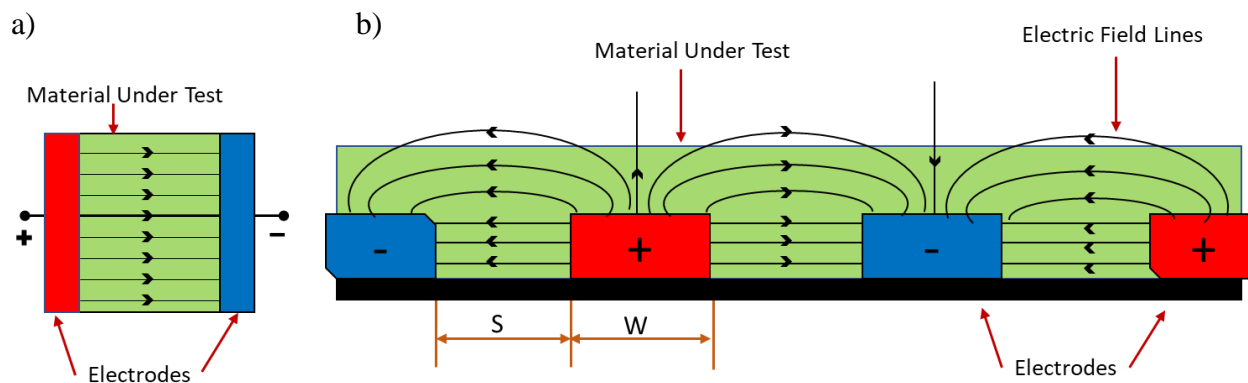


Figure A-1.6. a) Electric field pattern in parallel plate electrode configuration b) Electric field pattern in IDE

A voltage of 0.1 Vrms was selected carefully, examining the effect of different voltages (varying from 0.005V – 1 V) on the results. Higher voltages result in more dominant electrode polarization effect for relatively higher conductive polymer samples. And lower voltages lead to the noise in the data for lower conductivity samples specially in lower frequency range.

Due to the broader frequency range, which facilitates more accurate fitting of Nyquist plots, when possible, the LCR meter was used for measurements. However, because of the LCR limitation in performing high impedance measurements, the CB was used for "pure" (as received, with no additive added by us) low-temperature measurements (especially below the melt temperature). For higher temperatures measurement of pure polymer, the overlap of CB and LCR meter data for the given respective frequency ranges demonstrated consistency from the two different instruments as shown in Figure A-1.7.

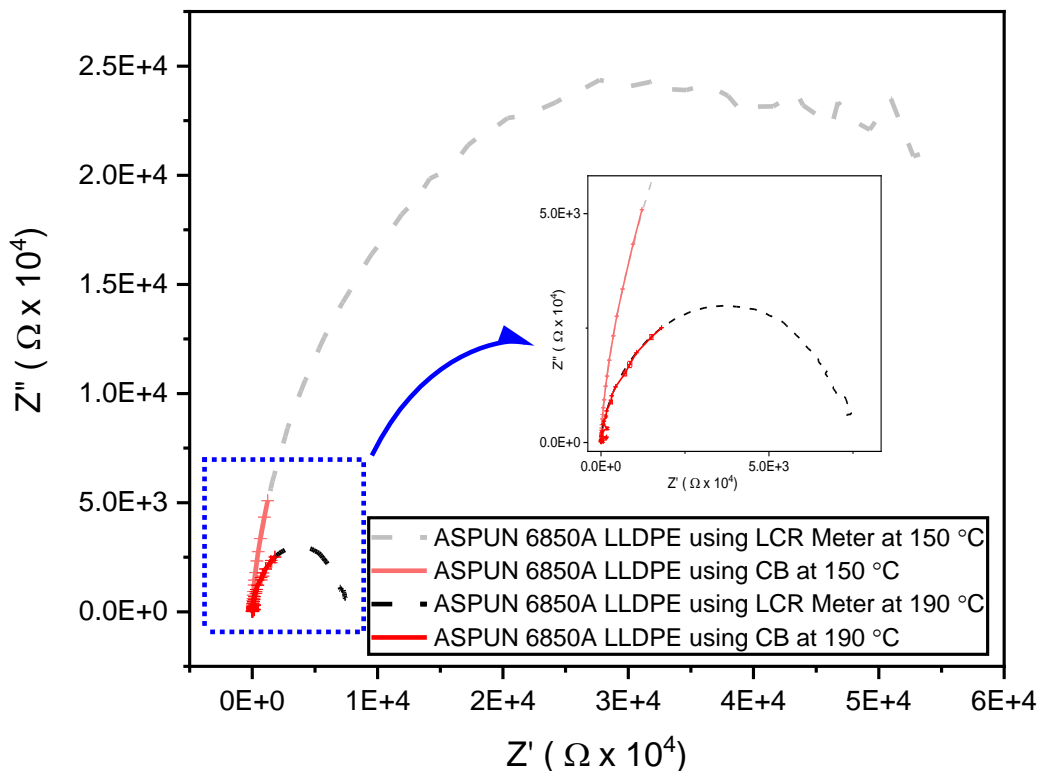


Figure A-1.7. Nyquist plot of ASPUN 6850A for two different melt temperatures (150 °C and 190 °C) showing an overlap over measured frequency range for both CB (solid lines) and LCR (dotted lines) measurements.

A-1.1.3. Effect of ambience on measurement

In addition to the measurements under 10^{-5} torr vacuum pressure, air measurements were also performed to determine the effect of room humidity on the impedance. This is important because some of the selected additives are static reduction agents which may work with adsorbed water from the air. For pure polymer cases, there was no significant effect as expected because PE is hydrophobic. Figure A-1.8 shows an example for ASPUN 6850 PE.

However, when an antistatic agent such as FA38 was added to the LLDPE, a significant change in the impedance as a function of environment (air or vacuum) was observed (Figure 8). Antistatic

agents are reported to be very sensitive to the amount of water vapors present in the ambient environment. Thus, conductivity measurements were performed in air in order to best match the effective conductivity present during actual electrospinning, which occurs in air. The second measurement technique (in-situ) was also developed to ensure a good match between the effective ionic conductivity during actual electrospinning and the explicit conductivity measurements.

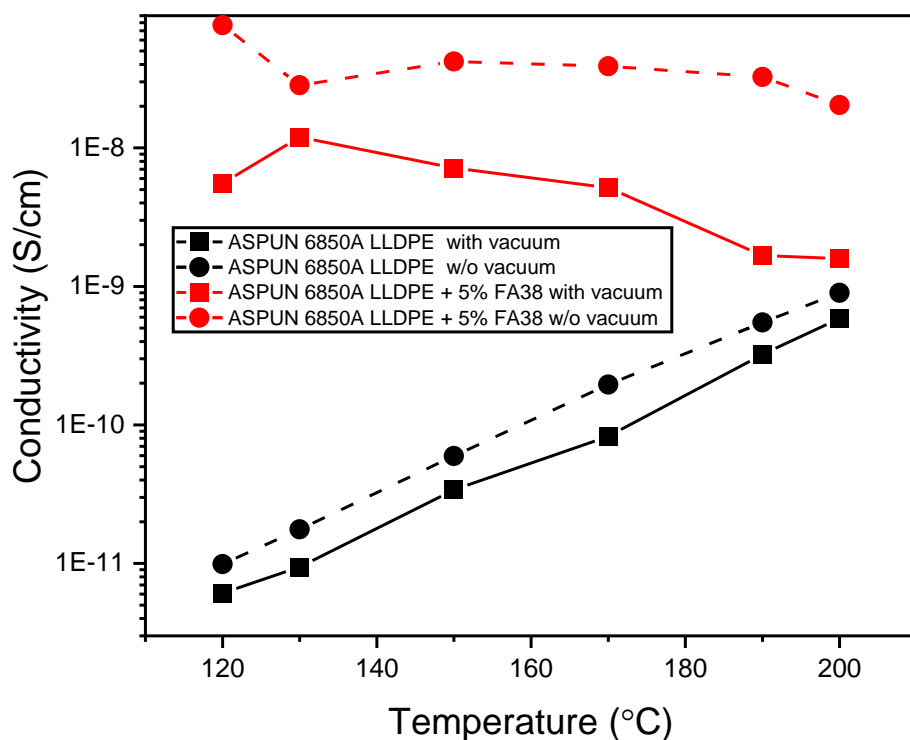


Figure A-1.8. Ionic conductivity as a function of polymer melt temperature for ASPUN 6850A LLDPE with no additive (black lines) and with 5wt% Hostastat FA38 additive (red lines) measured inside prober system with vacuum (solid lines) and without vacuum (dotted lines)

A-1.1.4. Broadband dielectric analysis to study the effect of different temperatures and additive wt%

A-1.1.4.1. Dielectric loss tangent curves

Dielectric loss tangent ($\tan \delta$) is the ratio of loss energy to storage energy, defined as,

$\tan \delta = \epsilon''/\epsilon' = Z'/Z''$. The maximum in delta occurs where $\omega\tau = 1$, ω is the applied frequency, and τ is the relaxation time (the characteristic time at which a conductive process within the material occurs)⁵. In other words, these peaks occur when the applied electric field frequency matches the molecular rotation frequency. Single relaxation peaks were observed in almost these cases, apart from the lowest temperatures for pure DNDA polymer because in these cases, the molecular frequency was lower than the experimental frequency range.

Figure 9 shows characteristic loss curves. Examining Figure A-1.9a (pure DNDA 1082), it is clear that relaxation peaks are moving towards the higher frequency with an increase in the temperature. This shift indicates that the relaxation time goes down with increased temperature, which is expected (for instance, for thermally activated segmental motion). With increased temperatures, enhancing the polymer segmental motion can cause faster ion dynamics. Since relaxation time is directly proportional to the ohmic component of the system, a decrease in relaxation time can cause an increase in conductivity.

However, when 5% FA38 is introduced (Figure A-1.9b), all the dynamics are faster (potential plasticization) and relaxation peaks do not shift as clearly with increased temperature. The broadening of the peak as we move from pure DNDA to additive DNDA suggests that there might be multiple relaxation times, as was also confirmed by the Nyquist plots where a depressed semicircle instead of a normal semicircle was observed.

Finally, with an increase in additive wt% (from 0 to 10) for lower temperatures (Figure A-1.9c), we see an increase in loss values at lower frequencies, which could be due to electrode polarization, confirmed by the second semicircle or spike (part of semicircle) in nyquist plots shown in next section.⁶ This effect is not that significant at higher temperatures (data pertinent to electrospinning in Fig A-1.9d), and the shift in the relaxation peaks suggests that we have faster dynamics for additives cases which may be one component leading to increased ionic conductivity.

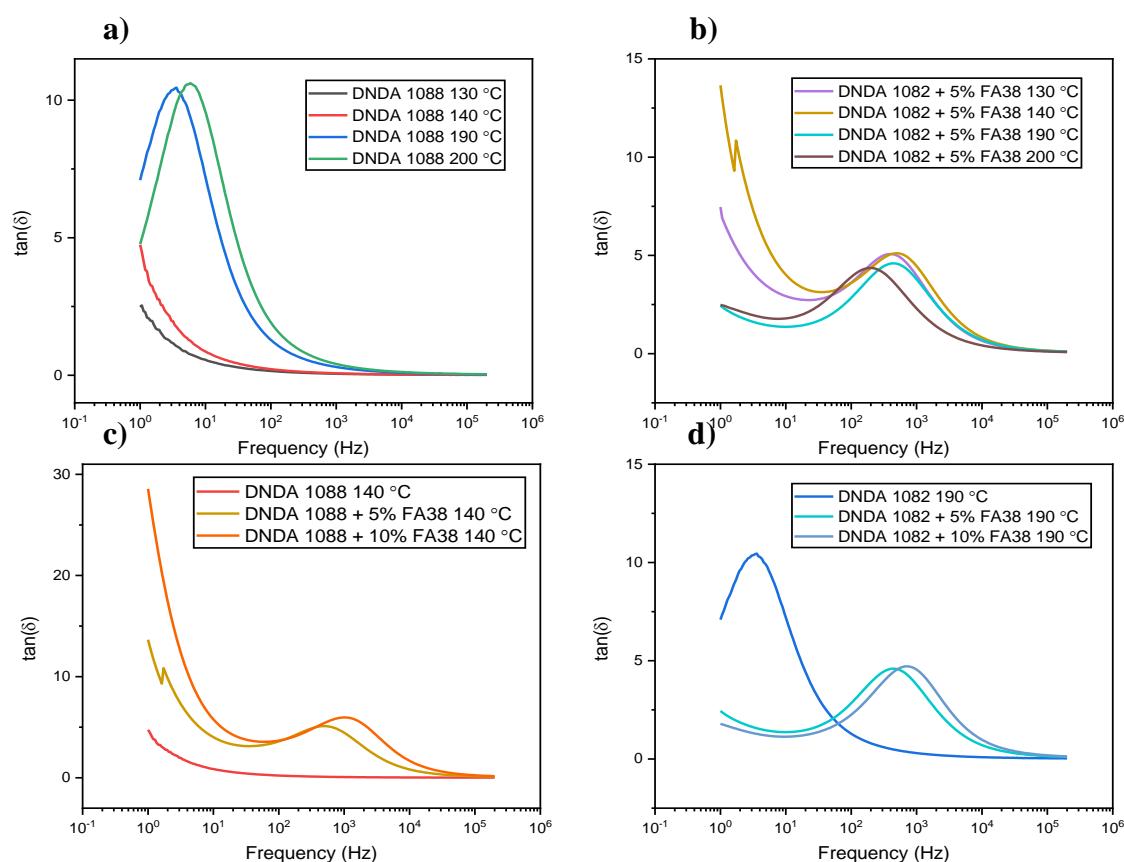


Figure A-1.9. Dielectric loss tangent as function of frequency was plotted for a) pure DNDA 1082 and b) DNDA 1082 with 5% FA38 additive as function of melt temperature (130 °C to 190 °C) c) and d) DNDA 1082 with increasing wt% of FA38 at lower (140 °C) and higher (190 °C) melt temperatures respectively.

A-1.1.4.2. Nyquist plots

A semicircle on the Nyquist plot suggests that the polymer system has a single relaxation time constant. Such Nyquist plots are fitted using different RC circuits. As shown in figure A-1.10 below, for pure DNDA 1082 at low temperatures, a half semicircle is observed; the LCR instrument limit results in noise-limited data for lower frequencies. As temperature increases, the radius of the semicircle (which accounts for the bulk resistance of the polymer) decreases. This is consistent with the dielectric tangent loss curve, where relaxation time decreases with increasing temperature as the polymer chains are more flexible, allowing the ions to move more freely.

With the increase in the FA38 additive wt% to DNDA 1082, we observe a significant drop (orders of magnitude lower) in the impedance values. This shows that the additive is compatible with the polymer and has decreased the overall bulk resistance of the polymer: probably both by plasticizing and adding free ions. Two semicircles are observed for the additive cases. The lower frequency semicircle corresponds to the electrode polarization effect; the higher frequency data corresponds to ion conduction in polymer bulk. For both 5 wt% and 10wt% FA38, higher frequency semicircles increase in size with an increase in the temperature, suggesting that the bulk resistance increases with an increase in the temperature. This could be due to additive evaporation or that increased thermal segmental motion (above a certain point) will impede ion transport (much like resistance in electron-carrying resistors increases with temperature). The equivalent RC circuits used for this measurement to calculate the bulk resistance are shown in Figure A-1.11.^{5,7}

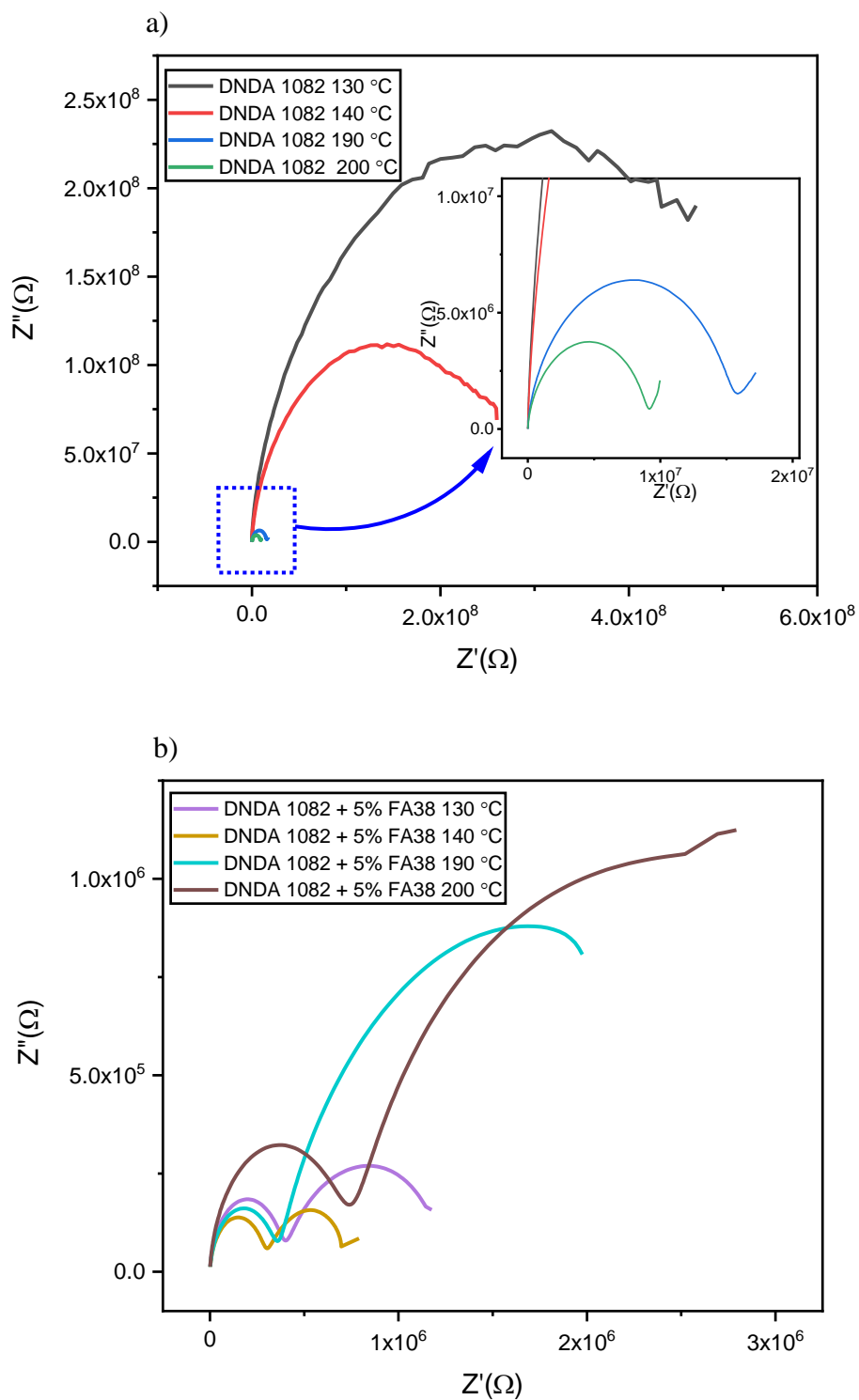


Figure A-1.10. Nyquist plots for given range of frequency (1Hz to 20kHz) were plotted for a) DNDA 1082 and b) DNDA 1082 + 5% FA38 with varying melt temperatures (130 °C to 200 °C)

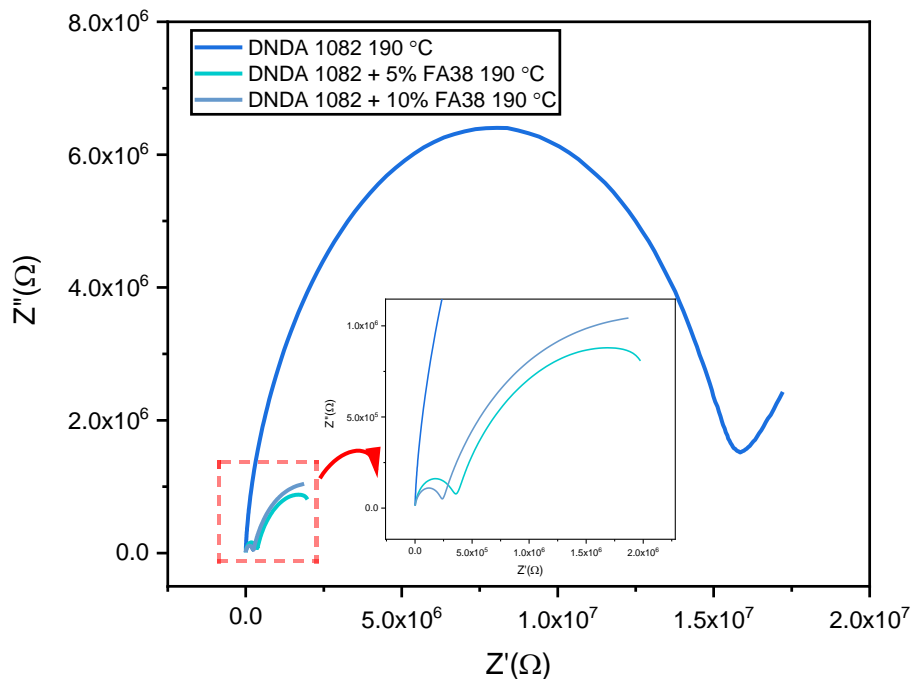


Figure A-1.11. Nyquist p Nyquist plots for given range of frequency (1Hz to 20kHz) were plotted for DNDA 1088 with varying (0,5,10) Hostastat FA38 additive wt% at higher melt temperature (190 °C)

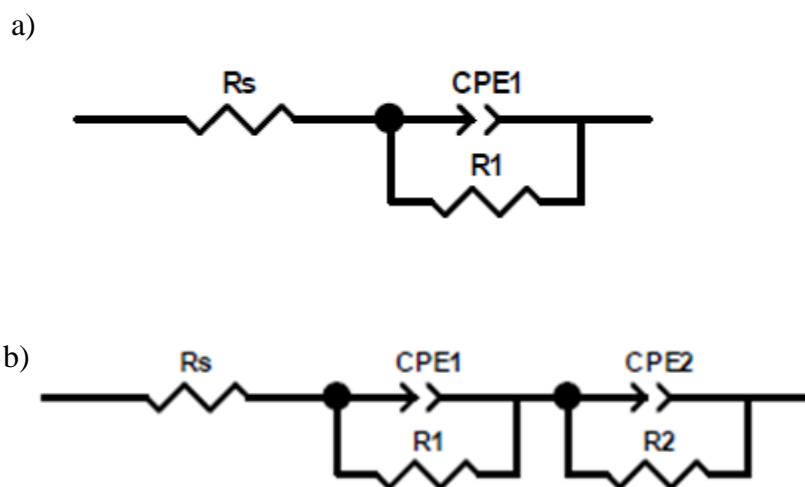


Figure A-1.12 Equivalent RC circuits for Nyquist plots a) for fitting one semicircle b) for fitting two semicircles. Constant phase element (CPE) instead of ideal capacitance is used to fit depressed semicircle of varying radii

A-1.1.4.3. Dielectric permittivity curves

Another way to understand the effect of additives on polymer ionic conductivity, is to observe the frequency dependence of the real and imaginary electrical permittivity, also known as dielectric constant and dielectric loss, respectively. Dielectric constant provides information about the material's polarizing (dipole reorientation) ability upon the application of the field, and dielectric loss provides information about energy loss in aligning the molecular dipoles in the field direction as well as other processes like leakage current. Both dielectric constant and dielectric loss shows the trend of decrease in their values with increasing frequency shown in figure A-1.12.

For low frequency regime, a high value of dielectric constant ϵ' is observed which can be attributed to dominant electrode polarization effect (as shown in Nyquist plots as well). This electrode polarization occurs due to the charge accumulation at the electrode polymer interface which creates its own electric field cancelling the external electric field thereby causing a decrease in the dielectric constant.⁸ Further, with increase in the frequency the dielectric relaxation process dominates causing the dielectric constant to decrease. As we increase the additive wt% the dielectric constant value increases indicating that this could be due to the increased number of chargers leading to higher dielectric constant and higher conductivity.⁹ At higher frequency dielectric constant is independent of the frequency. This makes sense as at higher frequencies, slow processes cannot respond and thus do not contribute to the dielectric constant. Comparing at lower frequency, we see an increase in dielectric constant with an increase in the additive wt% and the temperature for a given sample.

For the dielectric loss, ϵ'' show a decrease in its value attributed to dc resistivity at low frequency and dipole reorientation at high frequencies.^{10,11}

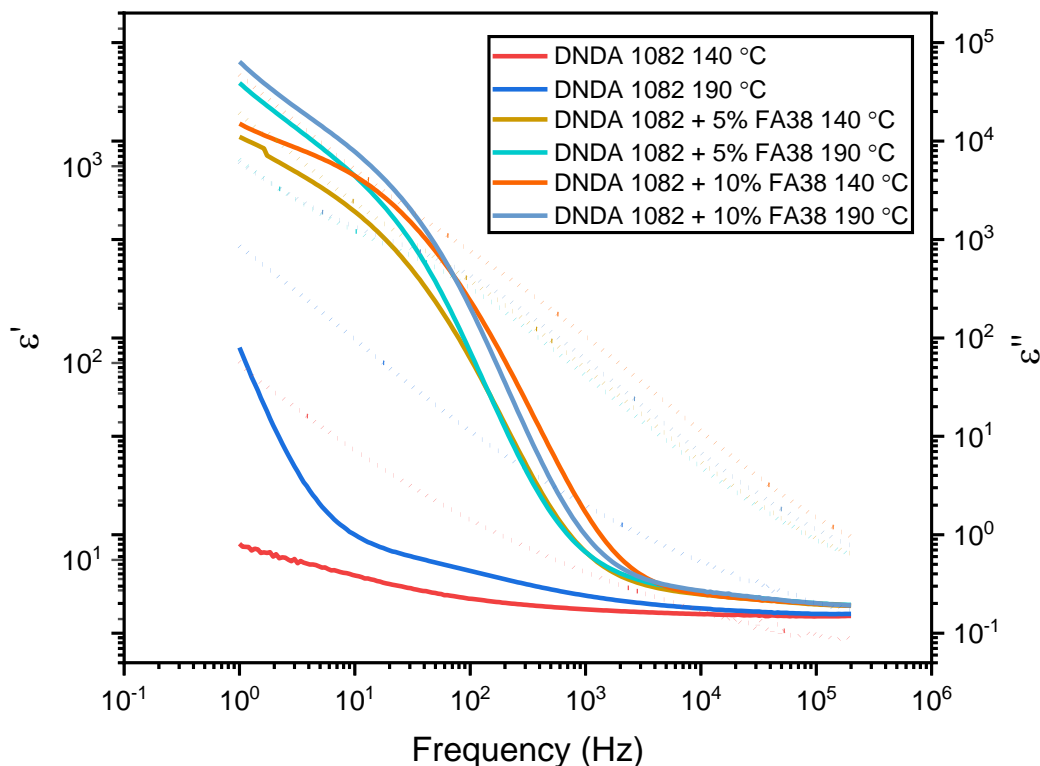


Figure A-1.13. Real (ϵ') and complex (ϵ'') dielectric permittivity as a function of frequency were plotted for DNDA 1082 with varying Hostastat FA38 additive wt% (0, 5, 10) at two different polymer melt temperatures (140 °C and 190 °C)

A-1.1.4.4. AC Conductivity curves

AC conductivity for leaky dielectrics has been obtained using $\sigma' = \sigma_{ac} = \omega \epsilon_0 \epsilon''$

Where ω is the angular frequency, ϵ_0 is the free space's dielectric permittivity, and ϵ'' represents the dielectric loss.¹²

Figure A-1.13 shows a typical graph of the real part of conductivity as a function of frequency for the polymer system. This graph consists of three different regions. Region 1 is the low-frequency region where conductivity increases rapidly with frequency mainly due to electrode polarization.¹³

Region 2 is an intermediate frequency plateau region corresponds to dc conductivity occurs mostly due to the long-range conduction of charge carriers. Region 3 is the region of high frequency, where the conductivity increases again with the increase in frequency and is also known as the near-constant loss (NCL) region as for this range of frequencies, the dielectric constant is independent of the frequency. At this high-frequency range, ion movement could be short-range (hopping) associated with ac conductivity, linearly increasing with linearly increasing with frequency.^{8,14-16}

A power law shown in following equation has been used by the researchers to fit the ac conductivity data

$$\sigma_{ac} = \sigma_{dc} + A\omega^n$$

Where σ_{dc} term is for the plateau intermediate frequency region and A is temperature dependent constant and n is a power law constant where usually $0 \leq n \leq 1$.¹⁴ Modified version of this power law has been used recently to include the low frequency electrode polarization.¹⁰⁴ DC conductivity values were extracted from graph A-1.12 by extrapolating the plateau region to zero frequency.

As we can see in Figure A-1.14, for pure DNDA, ac conductivity for lower temperature (near polymer melt temperature) is approaching the plateau; for the higher temperatures, we observe the plateau region. However, there is no electrode polarization for this case as free ion concentration in pure DNDA is small.

With the increase in the additive wt%, we observe all three regions. For the low-frequency region, the slopes for lower temperatures were smaller than those for higher temperatures. This indicates that the electrode polarization effect is more dominant for higher temperatures. This effect is also

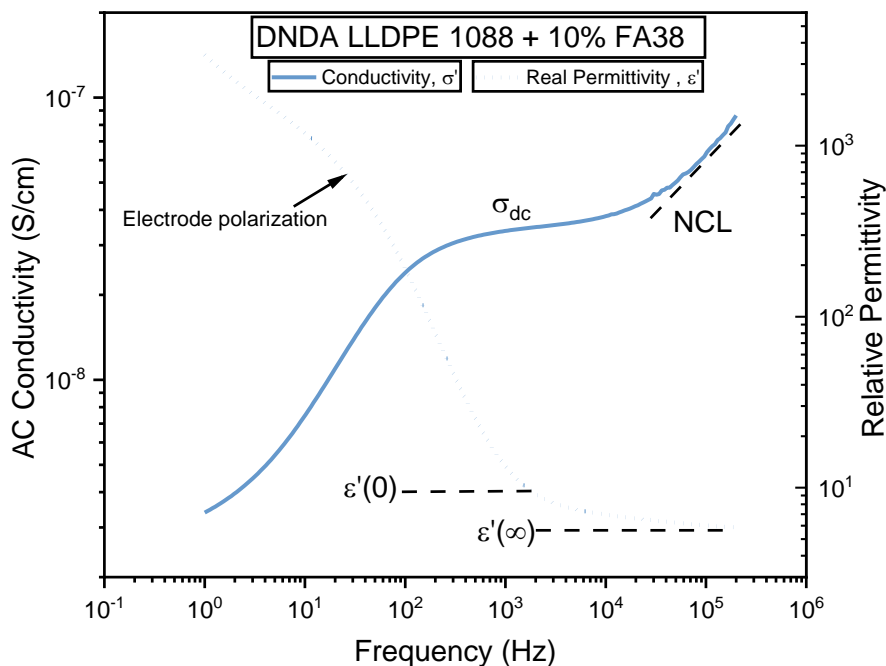


Figure A-1.14. Ac conductivity and real relative permittivity are plotted as function of frequency. Graph represents the lower and high frequency region dispersion region and intermediate frequency plateau region along with some limiting features.

visible in the Nyquist plot, where a second semicircle is observed for higher frequencies. For intermediate frequencies, dc conductivity is higher for lower temperatures. This effect is due to the long-range conduction of charge carriers and is consistent with the idea that increased concentration results in additional mobile ions thereby increasing the ionic conductivity.¹⁸ As we increase the temperature for respective additive wt%, increasing the polymer's thermal energy, we observe a slight decrease in conductivity. As mentioned above, this decrease could result from losing free ions from the polymer's surface due to the additive's evaporation at these higher temperatures, or that increased segmental motion is now impeding ion transport. For high frequency dispersive region, the ac conductivity increases with increase in frequency for all the

given cases. From pure DNDA to additive cases, this region shifts more towards higher frequencies and is confined in a much smaller range of frequencies, representing a faster ion migration. However, most of the frequency range of this graph corresponds to the plateau region as we increase the additive wt%, which suggests ions are conducting mainly due to long-range conduction phenomena.¹⁹

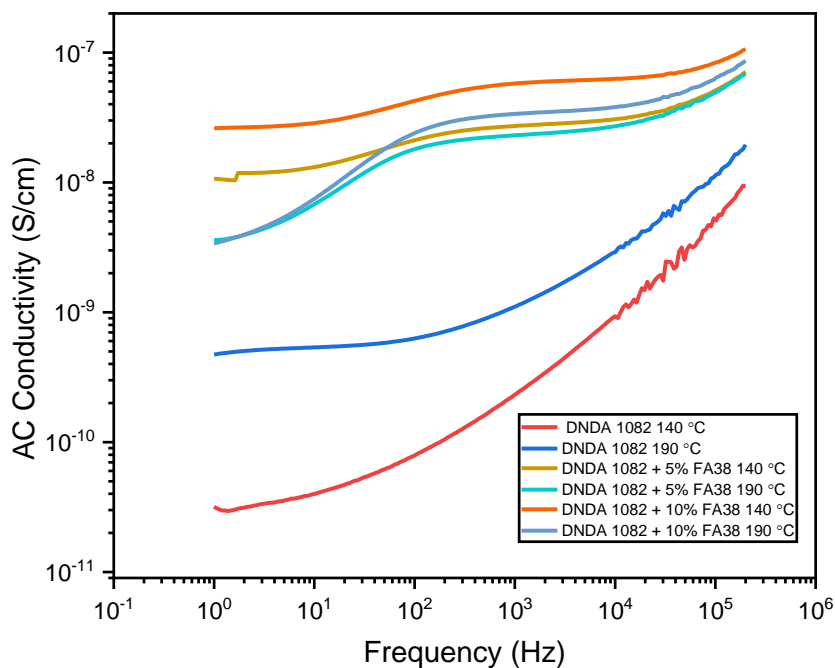


Figure A-1.15. AC conductivity as a function of frequency were plotted for DNDA 1082 with varying Hostastat FA38 additive wt% (0, 5, 10) at two different polymer melt temperatures (140 °C and 190 °C)

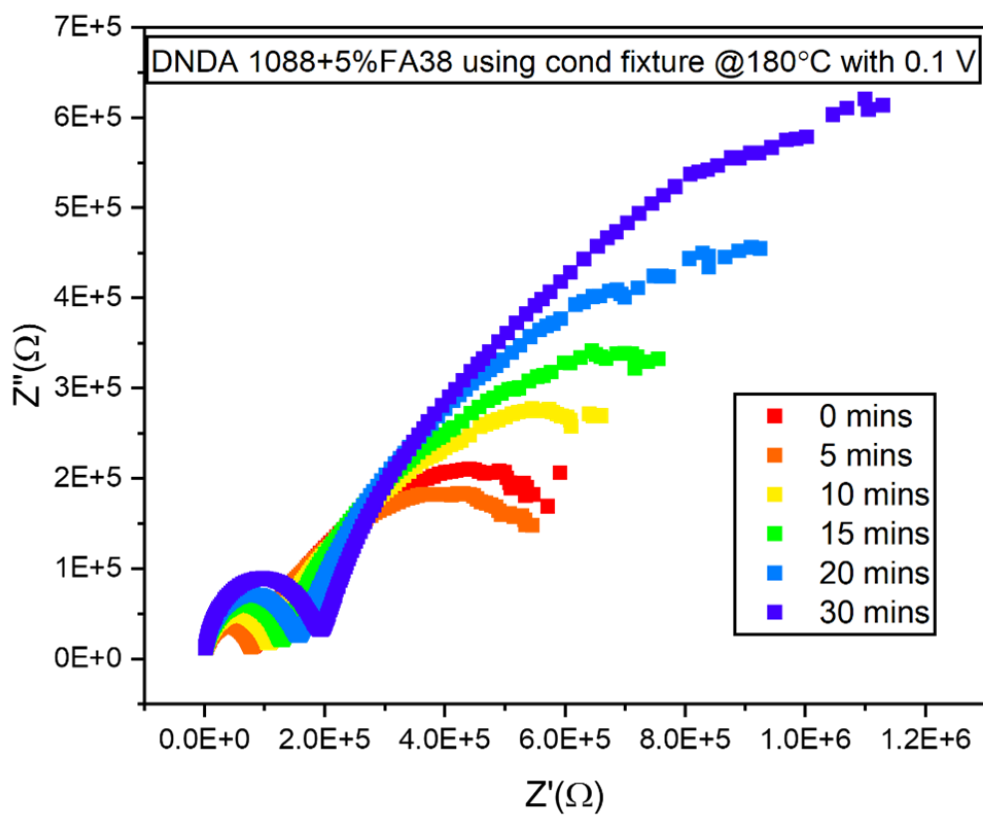


Figure A-1.16. Nyquist plot for DNDA 1088 + 5% FA38 measured via in-situ conductivity measurement as a function of time which the polymer was heated on the metal stage (0 mins is when polymer is fully melted, and temperature reaches 180 °C) was plotted.

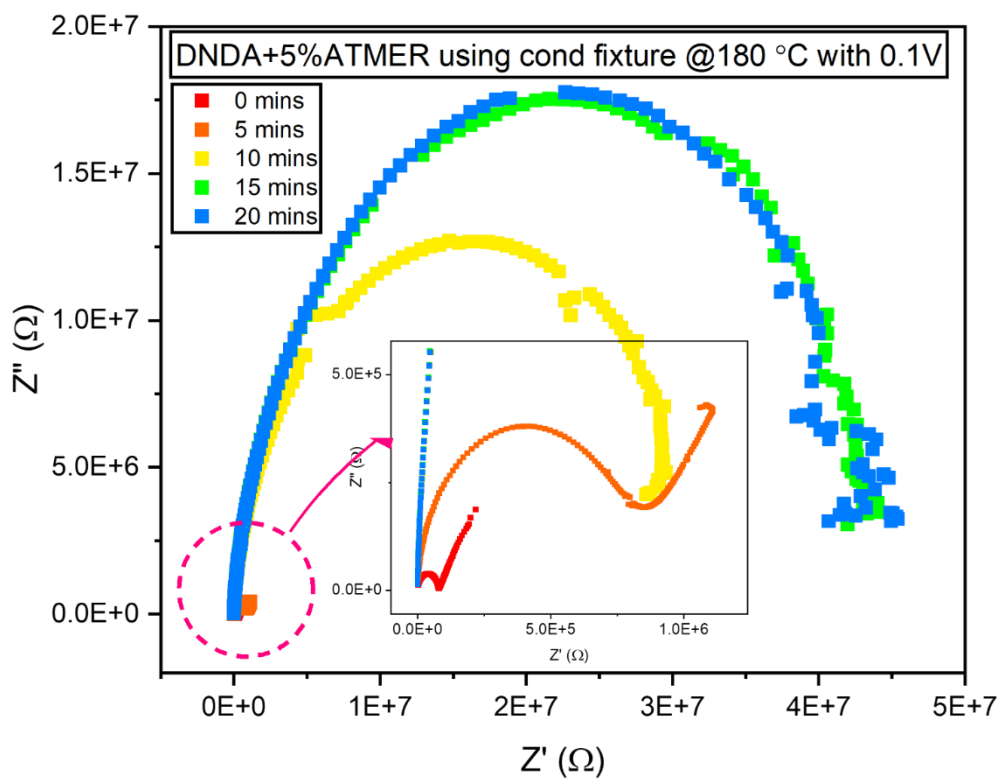


Figure A-1.17. Nyquist plot for DNDA 1088 + 5% ATMER129 measured via in-situ conductivity measurement as a function of time for which the polymer was heated on the metal stage (0 mins is when polymer is fully melted, and temperature reaches 180 °C) was plotted.

A-1.2.1. Program for automated analysis of LCR data

```

1 # -*- coding: utf-8 -*-
2 """
3 Created on Fri Oct 23 10:15:01 2020
4
5 @author: Neelam Sheoran
6 """
7
8 import argparse #for command line arguments
9 import pandas as pd #for csv dataframes
10 import numpy as np #For mathematics
11 import os #for directory structure
12
13 ap = argparse.ArgumentParser()
14
15 ap.add_argument('-i', '--input_path', type=str, required=True, help="path to input
16 folder")
17
18 ap.add_argument('-o', '--output_path', type=str, required=True,
19                 help="path to output folder")
20
21 args = vars(ap.parse_args())
22
23 input_path = args['input_path'] + '\input files'
24
25 for filename in os.listdir(input_path):
26     print(filename)
27     pd_dataframe = pd.read_csv(input_path+"\\" +filename, header=None)
28
29
30
31     pd_dataframe = pd_dataframe.iloc[13:, :] #Removing the 1st 16 rows
32                                     #(13 because 3 rows are empty)
33     if(pd_dataframe.shape[1] == 1):
34         pd_dataframe = pd.DataFrame(pd_dataframe.iloc[:, 0].str.split("\\"))
35         # Because the csv file has the delimiter as : "
36
37         pd_dataframe = pd.DataFrame(
38             pd_dataframe.iloc[:, 0].tolist(), index = pd_dataframe.index)
39         #Converting the string data to list then to columns
40
41
42     pd_dataframe.columns = pd_dataframe.iloc[0]
43     pd_dataframe = pd_dataframe[1:]
44         #Renaming columns
45
46
47     #Changing to float from string for calculations
48     pd_dataframe['Z[ohm]'] = pd_dataframe['Z[ohm]'].astype(float)
49     pd_dataframe['PHASE[deg]'] = pd_dataframe['PHASE[deg]'].astype(float)

```

```

50     pd_dataframe['FREQUENCY(Hz)'] = pd_dataframe['FREQUENCY(Hz)'].astype(float)
51
52     #Making 2 new columns as per requirement
53     pd_dataframe['ReZ'] = np.abs((pd_dataframe['Z[ohm]'] *
54 np.cos(((pd_dataframe['PHASE[deg]']*3.14)/(180)))))
55
56     pd_dataframe['ImZ'] = np.abs((pd_dataframe['Z[ohm]'] *
57 np.sin(((pd_dataframe['PHASE[deg]']*3.14)/(180)))))
58
59     pd_dataframe['omega'] =pd_dataframe['FREQUENCY(Hz)']*3.14*2
60
61     pd_dataframe['tan(delta)'] = pd_dataframe['ReZ']/pd_dataframe['ImZ']
62
63     pd_dataframe['logf'] = np.log(pd_dataframe['FREQUENCY(Hz)'])
64
65     pd_dataframe['ReE'] =(0.83*pd_dataframe['ImZ'])/(8.85*10**(-
66 12)*pd_dataframe['omega']*pd_dataframe['Z[ohm]']*pd_dataframe['Z[ohm]'])
67
68     pd_dataframe['ImE'] = (0.83*pd_dataframe['ReZ'])/(8.85*10**(-
69 12)*pd_dataframe['omega']*pd_dataframe['Z[ohm]']*pd_dataframe['Z[ohm]'])
70
71     pd_dataframe['ReM'] = (pd_dataframe['omega'])*(8.85*10**(-
72 12)/(0.83))*(pd_dataframe['ImZ'])
73
74     pd_dataframe['ImM'] = (pd_dataframe['omega'])*(8.85*10**(-
75 12)/(0.83))*(pd_dataframe['ReZ'])
76
77     pd_dataframe['Sigma'] = (pd_dataframe['omega'])*(8.85*10**(-
78 12)*(pd_dataframe['ImE']))
79
80     #Manipulating output file name
81     out_filename = filename[:-4]+" zview sorted.txt" #Excluding .csv at the last
82
83     output_path = args['output_path'] + '\\output files\\' + out_filename
84
85     #Changing float to scientific notation
86     pd_dataframe['ReZ'] = pd_dataframe['ReZ'].map(lambda x : '{:.4E}'.format(x))
87     pd_dataframe['ImZ'] = pd_dataframe['ImZ'].map(lambda x : '{:.4E}'.format(x))
88     pd_dataframe['FREQUENCY(Hz)'] = pd_dataframe['FREQUENCY(Hz)'].map(lambda x :
89 '{:.4E}'.format(x))
90     pd_dataframe['omega'] = pd_dataframe['omega'].map(lambda x :
91 '{:.4E}'.format(x))
92     pd_dataframe['tan(delta)'] = pd_dataframe['tan(delta)'].map(lambda x :
93 '{:.4E}'.format(x))
94     pd_dataframe['logf'] = pd_dataframe['logf'].map(lambda x : '{:.4E}'.format(x))
95     pd_dataframe['ReE'] = pd_dataframe['ReE'].map(lambda x : '{:.4E}'.format(x))
96     pd_dataframe['ImE'] = pd_dataframe['ImE'].map(lambda x : '{:.4E}'.format(x))
97     pd_dataframe['ReM'] = pd_dataframe['ReM'].map(lambda x : '{:.4E}'.format(x))
98     pd_dataframe['ImM'] = pd_dataframe['ImM'].map(lambda x : '{:.4E}'.format(x))
99     pd_dataframe['Sigma'] = pd_dataframe['Sigma'].map(lambda x : '{:.4E}'.format(x))

```

```
#Exporting the required 3 columns
pd_dataframe.iloc[:, [0,1,2,3,-10,-9,-8,-7,-6,-5,-4,-3,-2,
1]].to_csv(output_path, index = False, sep=',', header = True)
else:
    print("JOB DONE!") # Printing Final Message
```

A-1.2.2. Program for automated analysis of capacitance bridge (CB) data

hilite.me converts your code snippets into pretty-printed HTML **format**, easily embeddable into blog posts, emails **and** websites.

Just copy the source code to the left pane, select the language **and** the color scheme, **and** click "Highlight!". The HTML **from** the right pane can now be pasted to your blog **or** email, no external CSS **or** Javascript files are required.

Source code:

```
import numpy as np
import pandas as pd
import re
from os import listdir
from os.path import isfile, join
targetfolder='C:/Clarke Lab/Python Files/Python Scripts/Input for data
massager' #'C:/Users/brent_000/Documents/Clarke Lab/labview files/My 2700A
files/Data/'
outputfolder='C:/Clarke Lab/Python Files/Python Scripts/Output for data
massager'
#files=['NtPEO20NaIafterinpedanceanalyzer_redo_r1 03-19-
2018','NtPEO20NaIafterinpedanceanalyzer_redo_r2 03-19-
2018','NtPEO20NaIafterinpedanceanalyzer_redo_r3 03-19-
2018','AB_PEO20NaIafterinpedanceanalyzer_redo_r1 03-19-
2018','AB_PEO20NaIafterinpedanceanalyzer_redo_r1 03-20-
2018','AB_PEO20NaIafterinpedanceanalyzer_redo_r2 03-20-
2018','AB_PEO20NaIafterinpedanceanalyzer_redo_r3 03-20-2018']

def GetFiles(folder):
    onlyfiles = [f for f in listdir(folder) if isfile(join(folder, f)) and
re.search(' analyzed.txt\Z',f)==None and re.search(' meta.txt\Z',f)==None]
    return onlyfiles

def message(_folder_,_file_,_outputfolder_, avfreq=True, labarr=[2,4,5,6,7]):
    '''
    avfreq determines wether to average all measurements of the same frequency
    labarr determines which parts of the file name will be used in the origin
    comments as a label
    time determines how to display time 'relative' will give relative to the
    first measurement or
    specify a string format such as 'MM-DD-YYYY hh:mm:ss' am/pm not supported
    '''
    _file_=re.sub('.txt\Z','',_file_)
    path=join(_folder_,_file_+'.txt')

    data=pd.read_csv(path,delimiter='\t')
    data_sub=data.loc[1:,:].copy().dropna()

    unitav=data.iloc[0:1,1:]
    if timef=='relative':
        unitav.loc[0,'Time']='s'
    unitstd=unitav.copy()
    unitav.columns=unitav.columns+' av.'
    unitstd.columns=unitstd.columns+' std'
    units=pd.concat([data.iloc[0:1,0:1],unitav,unitstd],axis=1)
```

```

data_sub=data_sub.dropna()
data_sub=data_sub.astype({'Freq.':float,'Cap.':float,'Loss':float})
data_sub.loc[:,'Time']=data_sub.loc[:,'Time'].apply(lambda
x:timeparse(x,timef))

if avfreq==True:
    dataAv=pd.pivot_table(data_sub,index='Freq.',aggfunc=np.mean)
    dataStd=pd.pivot_table(data_sub,index='Freq.',aggfunc=np.std)
    dataAv.columns=dataAv.columns+' av.'
    dataStd.columns=dataStd.columns+' std'
    numDataAv=pd.concat([dataAv,dataStd],axis=1).reset_index()

else:
    numDataAv=data_sub.sort_values(by='Freq.')

numDataAv.columns=numDataAv.columns[0:1].append(numDataAv.columns[1:]+ ' av. ')

newindex=pd.Index(['Freq.','omega','Loss av.','Loss std','ReZ
av.','ReZstd','ImZ av.','ImZstd','AbsZ','AbsZstd'])
numDataAv=numDataAv.reindex(columns=newindex)
DataAv=pd.DataFrame(index=[0],columns=newindex)
units=units.reindex(columns=newindex)
units.loc[0,'omega']='rad/s'
units.loc[0,'ReZ av.':'ImZ av.']='Ohms'

#####
#####-----Convert to w and Farads-----#####
#####
numDataAv.loc[:,'Cap. av.':'Cap. std']=numDataAv.loc[:,'Cap. av.':'Cap.
std']*(10**(-12))
numDataAv.loc[:,'omega']=numDataAv.loc[:,'Freq.']*2*np.pi
units.loc[0,'Cap. av.']='F'
units.loc[0,'Cap. std']='F'

#####
##### Calculate real and imaginary R #####
#####
def ReZ(x):
    W=x['omega']
    C=x['Cap. av. ']
    T=x['Loss av. ']
    R=1/(C*T*W)
    ReZ=R/(1+C**2*R**2*W**2)
    return ReZ

def ReZstd(x):
    W=x['omega']
    C=x['Cap. av. ']
    dC=x['Cap. std']
    T=x['Loss av. ']
    dT=x['Loss std']
    R=1/(C*T*W)
    dR=(dT**2/(C**2*T**4*W**2)+dC**2/(C**4*T**2*W**2))**.5

```

```

ReZstd=( (4*C**2*dC**2*R**6*W**4+dR**2*(1-
2*C**2*R**2*W**2+C**4*R**4*W**4) ) / (1+C**2*R**2*W**2) **4) ** .5
return ReZstd

def ImZ(x):
W=x['omega']
C=x['Cap. av. ']
T=x['Loss av. ']
R=1/(C*T*W)
ImZ=(C*R**2*W)/(1+C**2*R**2*W**2)
return ImZ

def ImZstd(x):
W=x['omega']
C=x['Cap. av. ']
dC=x['Cap. std']
T=x['Loss av. ']
dT=x['Loss std']
R=1/(C*T*W)
dR=(dT**2/(C**2*T**4*W**2)+dC**2/(C**4*T**2*W**2))**0.5
ImZstd=( (R**2*W**2*(dC**2*R**2+C**4*dC**2*R**6*W**4+C**2*(4*dR**2-
2*dC**2*R**4*W**2) ) ) / (1+C**2*R**2*W**2) **4) ** .5
return ImZstd
numDataAv.loc[:, 'ReZ av. ']=numDataAv.apply(ReZ,axis=1)
numDataAv.loc[:, 'ReZ std']=numDataAv.apply(ReZstd,axis=1)
numDataAv.loc[:, 'ImZ av. ']=numDataAv.apply(ImZ,axis=1)
numDataAv.loc[:, 'ImZ std']=numDataAv.apply(ImZstd,axis=1)

def AbsZ(x):
ReZ=x['ReZ av. ']
ImZ=x['ImZ av. ']

return (ReZ**2+ImZ**2)**.5

def AbsZstd(x):
ReZ=x['ReZ av. ']
ImZ=x['ImZ av. ']
dReZ=x['ReZ std']
dImZ=x['ImZ std']

return ((dImZ*ImZ**2)/(ImZ**2+ReZ**2)+(dReZ**2*ReZ**2)/(ImZ**2+ReZ**2))**0.5

numDataAv.loc[:, 'MagZ av. ']=numDataAv.apply(AbsZ,axis=1)
numDataAv.loc[:, 'MagZ std']=numDataAv.apply(AbsZstd,axis=1)

numDataAv.loc[:, 'ReZ av. 10^-6']=numDataAv.loc[:, 'ReZ av. '].apply(lambda
x: x*10**-6)
numDataAv.loc[:, 'ReZ std 10^-6']=numDataAv.loc[:, 'ReZ std'].apply(lambda
x: x*10**-6)
numDataAv.loc[:, 'ImZ av. 10^-6']=numDataAv.loc[:, 'ImZ av. '].apply(lambda
x: x*10**-6)
numDataAv.loc[:, 'ImZ std 10^-6']=numDataAv.loc[:, 'ImZ std'].apply(lambda
x: x*10**-6)
numDataAv.loc[:, 'MagZ av. 10^-6']=numDataAv.loc[:, 'MagZ
av. '].apply(lambda x: x*10**-6)

```

```

numDataAv.loc[:, 'MagZ std 10^-6'] = numDataAv.loc[:, 'MagZ
std'].apply(lambda x: x*10**-6)

if timef=='relative':
    numDataAv.loc[:, 'Time av.']=numDataAv.loc[:, 'Time av.']-
numDataAv.loc[:, 'Time av.'].min()
    numDataAv=numDataAv.dropna(axis=1)

# namematch=re.search('(.*?) (S[0-9]+) (NtN*[0-9]+) ([0-9]+) ([0-9a-zA-
Z]*) (R[0-9]+) (.*) ?([0-9][0-9]-[0-9][0-9]-[0-9][0-9][0-9][0-9]).*', _file_)
name=''
for labi in labarr:
    try:
        name+=namematch[labi]+' '
    except:
        pass
name=re.sub('\Z', '', name)
DataAv.loc[:, :] = name
DataAv=units.append(DataAv)
DataAv=DataAv.append(numDataAv.astype('str'), ignore_index=True)
DataAv=DataAv.reindex(columns=newindex)

DataAv.to_csv(join(_outputfolder_, _file_+'
analyzed'+'.txt'), sep='\t', index=False)

#def timeparse(time, form):
    tmatch=re.search('([0-9][0-9])-([0-9][0-9])-([0-9][0-9][0-9][0-9])-([0-
9][0-9]):([0-9][0-9]):?([0-9]?[0-9]?)', time)
mon, day, year, hour, mi, sec=tmatch.group(1), tmatch.group(2), tmatch.group(3), tmat
ch.group(4), tmatch.group(5), tmatch.group(6)
    if sec=='':
        sec='00'
    if form=='relative':
        mon, day, year, hour, mi, sec=[int(a) for a in [mon, day, year, hour, mi, sec]]

    totalsec=sec+mi*60+hour*60**2+day*60**2*24
    return totalsec
else:
    def replace(subf, unit):
        n=len(subf.group(0))
        return unit[-n:]
    form=re.sub('M+', lambda x: replace(x, mon), form)
    form=re.sub('D+', lambda x: replace(x, day), form)
    form=re.sub('Y+', lambda x: replace(x, year), form)
    form=re.sub('h+', lambda x: replace(x, hour), form)
    form=re.sub('m+', lambda x: replace(x, mi), form)
    form=re.sub('s+', lambda x: replace(x, sec), form)

    return form

def run(avfreq=True):
    files=GetFiles(targetfolder)

```

```
for file in files:
    message(targetfolder,file,outputfolder,avfreq=avfreq)
#
#     try:
#         message(targetfolder,file,outputfolder,avfreq=avfreq,timef=timef)
#     except:
#         print(file+' not analyzed')
```

A-1.3. References

- 1) Lasia, A. Electrochemical Impedance Spectroscopy and Its Applications. 117.
- 2) Woodward, W. H. H. Broadband Dielectric Spectroscopy—A Practical Guide. In *ACS Symposium Series*; Woodward, W. H. H., Ed.; American Chemical Society: Washington, DC, 2021; Vol. 1375, pp 3–59. <https://doi.org/10.1021/bk-2021-1375.ch001>.
- 3) Yin, H.; Schönhals, A. Broadband Dielectric Spectroscopy on Polymer Blends. In *Polymer Blends Handbook*; Utracki, L. A., Wilkie, C. A., Eds.; Springer Netherlands: Dordrecht, 2014; pp 1299–1356. https://doi.org/10.1007/978-94-007-6064-6_14.
- 4) Abdul Rahman, M. S.; Mukhopadhyay, S. C.; Yu, P.-L. Novel Planar Interdigital Sensors. In *Novel Sensors for Food Inspection: Modelling, Fabrication and Experimentation*; Abdul Rahman, M. S., Mukhopadhyay, S. C., Yu, P.-L., Eds.; Springer International Publishing: Cham, 2014; pp 11–35. https://doi.org/10.1007/978-3-319-04274-9_2.
- 5) The Phasance Concept | PDF | Electrical Impedance | Capacitor
<https://www.scribd.com/doc/71923015/The-Phasance-Concept> (accessed 2022 -03 -20).
- 6) Ishai, P. B.; Talary, M. S.; Caduff, A.; Levy, E.; Feldman, Y. Electrode Polarization in Dielectric Measurements: A Review. *Meas. Sci. Technol.* **2013**, *24* (10), 102001. <https://doi.org/10.1088/0957-0233/24/10/102001>.
- 7) Macdonald, J. Impedance Spectroscopy - Old Problems and New Developments. *Electrochim. Acta* **1990**, *35* (10), 1483–1492. [https://doi.org/10.1016/0013-4686\(90\)80002-6](https://doi.org/10.1016/0013-4686(90)80002-6).

- 8) Arya, A.; Sharma, A. L. Effect of Salt Concentration on Dielectric Properties of Li-Ion Conducting Blend Polymer Electrolytes. *J Mater Sci: Mater Electron* **2018**, *29* (20), 17903–17920. <https://doi.org/10.1007/s10854-018-9905-3>.
- 9) Assessment, U. E. N. C. for E. Vibrational, ac impedance and dielectric spectroscopic studies of poly(vinylacetate)-N,N-dimethylformamide-LiClO₄ polymer gel electrolytes https://hero.epa.gov/hero/index.cfm/reference/details/reference_id/7749233 (accessed 2022 -03 -20).
- 10) Sengwa, R. J.; Choudhary, S. Dielectric Properties and Structural Dynamics of Melt Compounded Hot-Pressed Poly (Ethylene Oxide)–Organophilic Montmorillonite Clay Nanocomposite Films. *Bulletin of Materials Science* **2012**, *35* (1), 19–25.
- 11) Ravi, M.; Pavani, Y.; Kumar, K. K.; Bhavani, S.; Sharma, A. K.; Rao, V. V. R. N. Studies on Electrical and Dielectric Properties of PVP:KBrO₄ Complexed Polymer Electrolyte Films. *Materials Chemistry and Physics* **2011**, *1–2* (130), 442–448. <https://doi.org/10.1016/j.matchemphys.2011.07.006>.
- 12) Raju, G. G. *Dielectrics in Electric Fields*, 0 ed.; CRC Press, 2003. <https://doi.org/10.1201/9780203912270>.
- 13) Tsonos, C. Comments on Frequency Dependent Ac Conductivity in Polymeric Materials at Low Frequency Regime. *Current Applied Physics* **2019**, *19* (4), 491–497. <https://doi.org/10.1016/j.cap.2019.02.001>.
- 14) Greenhoe, B. M.; Hassan, M. K.; Wiggins, J. S.; Mauritz, K. A. Universal Power Law Behavior of the AC Conductivity versus Frequency of Agglomerate Morphologies in Conductive Carbon Nanotube-Reinforced Epoxy Networks. *J. Polym. Sci. Pt. B-Polym. Phys.* **2016**, *54* (19), 1918–1923. <https://doi.org/10.1002/polb.24121>.

- 15) Siekierski, M.; Wieczorek, W. Application of the Universal Power-Law to the Studies of Ac Conductivity of Polymeric Electrolytes. *Solid State Ion.* **1993**, *60* (1–3), 67–71.
[https://doi.org/10.1016/0167-2738\(93\)90276-9](https://doi.org/10.1016/0167-2738(93)90276-9).
- 16) Roggero, A.; Caussé, N.; Dantras, E.; Villareal, L.; Santos, A.; Pébère, N. Thermal Activation of Impedance Measurements on an Epoxy Coating for the Corrosion Protection: 1. Dielectric Spectroscopy Response in the Dry State. *Electrochimica Acta* **2019**, *303*, 239–245.
- 17) Khamzin, A.; Popov, I.; Nigmatullin, R. Correction of the Power Law of Ac Conductivity in Ion-Conducting Materials Due to the Electrode Polarization Effect. *Physical review. E, Statistical, nonlinear, and soft matter physics* **2014**, *89*, 032303.
<https://doi.org/10.1103/PhysRevE.89.032303>.
- 18) Jonscher, A. K. A New Understanding of the Dielectric Relaxation of Solids. *J Mater Sci* **1981**, *16* (8), 2037–2060. <https://doi.org/10.1007/BF00542364>.
- 19) Henn, F.; Elliott, S. R.; Giuntini, J. C. Complex Permittivity in Ionically Conducting Solids: A Hopping Model. *Journal of Non-Crystalline Solids* **1991**, *136* (1), 60–66.
[https://doi.org/10.1016/0022-3093\(91\)90119-Q](https://doi.org/10.1016/0022-3093(91)90119-Q).

Appendix A-2

Supporting Information

Increasing ionic conductivity within thermoplastics via commercial additives results in a dramatic decrease in fiber diameter from melt electrospinning

Neelam Sheoran, Brent Boland, Samuel Thornton, Jason R. Bochinski, and Laura I. Clarke**

Experimental results demonstrate that the LLDPE melt viscosity has no predictive effect on jet size but there is a clear trend with conductivity. Figure A-2.1 plots observed jet radius and fiber diameter versus viscosity and conductivity. DNDA ($\eta = 60 - 70$ Pa-s) and ASPUN ($\eta = 250 - 300$ Pa-s) r_{jet} values range from 20 – 60 μm and 20 – 50 μm , respectively (Figure S1a). Figure S1b shows r_{jet} as a function of measured conductivity where the downward trend with conductivity raised to the power -0.25 (as in Equation 7) is evident.

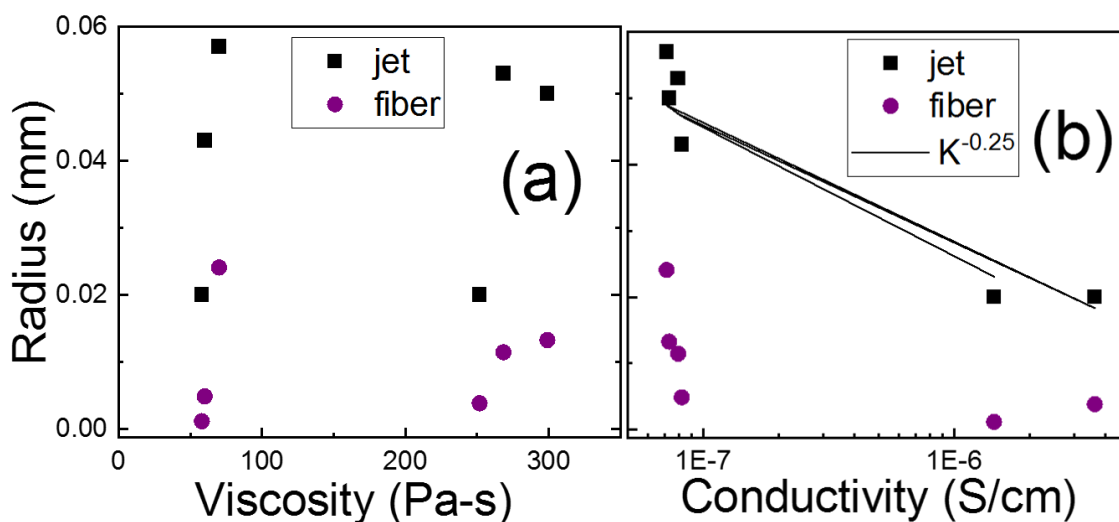


Figure A-2.1. a) Jet and ultimate fiber size show no dependence on melt viscosity for either LLDPE formulation. b) Jet size decreases as melt conductivity increases. The line is conductivity raised to the -0.25 power.

Figure A-2.2 shows an expanded view of the lower histogram panels of Figure 10 for easier viewing of the results for ASPUN (Figure S2a) and DNDA (Figure S2b). Increasing the melt

conductivity results in a significant increase in fraction of fibers produced with sub-micron diameters: for example, for DNDA + 5 wt% FA38 20% of the fibers created were nanoscale ($< 1 \mu\text{m}$), as compared with 0% for the neat DNDA.

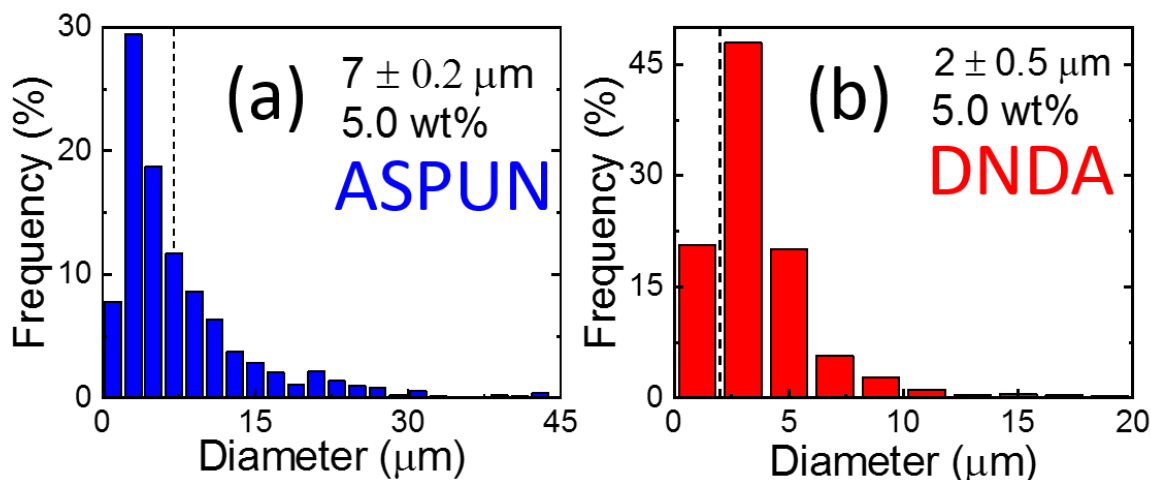


Figure A-2.2. Expanded histogram graphs of fiber diameter distributions for different LLDPE formulations with 5.0 wt% FA38 additive loading for a) ASPUN (blue data) and b) DNDA (red data), respectively.

The melt electrospinning apparatus (Figure A-2.3) consists of a single piece of aluminum machined to create the source plate, onto which a replaceable tungsten carbide-tipped blade attaches (flush to the plate surface) with countersunk screws. The blade provides a consistent, sharp plate edge that is more resistant to scratches and defects when cleaning. The blade's length was adjusted slightly to enable a tight connection.

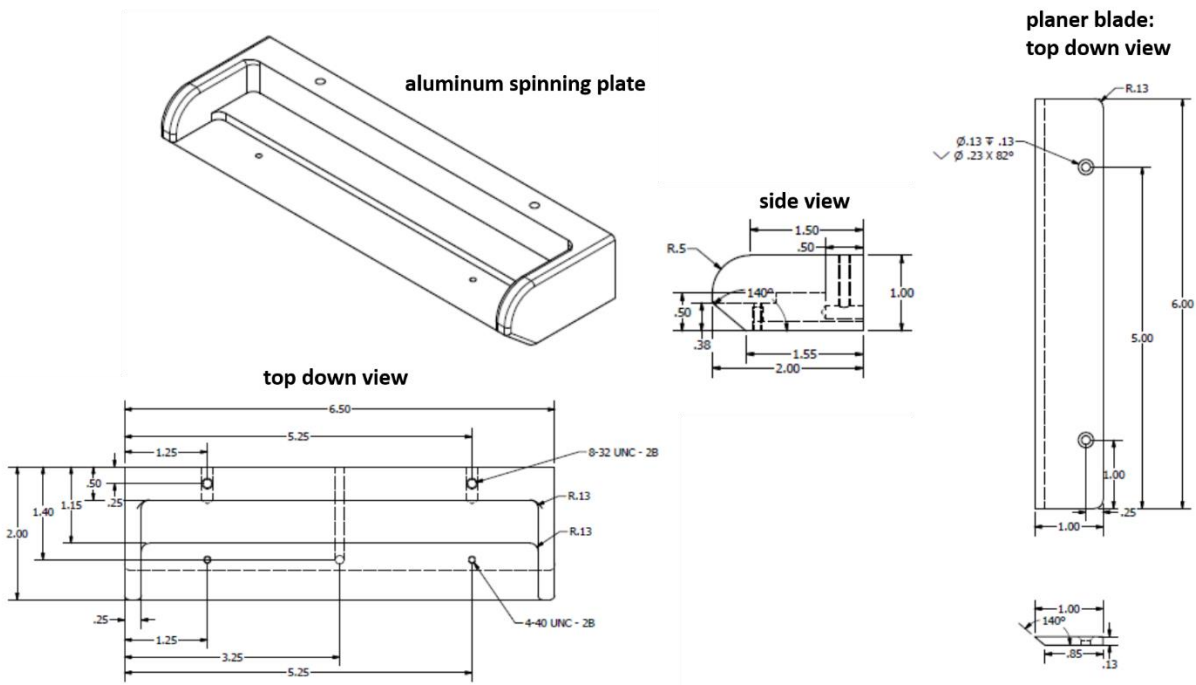


Figure A-3.3. Drawings of the source plate and planer blade. Dimensions are given in inches.